Doctoral Dissertations   Student Scholarship

Spring 2007

Structural and functional pulmonary imaging using hyperpolzarized xenon-129

Iga Muradyan
University of New Hampshire, Durham

Follow this and additional works at: https://scholars.unh.edu/dissertation

STRUCTURAL AND FUNCTIONAL PULMONARY IMAGING USING

HYPERPOLARIZED ^{129}XE

BY

IGA MURADYAN

Master's Degree, Yerevan State University, 1996

DISSERTATION

Submitted to the University of New Hampshire
in Partial Fulfillment of
the Requirements for the Degree of

Doctor of Philosophy

in
Physics

May 2007

UMI Number: 3260603

INFORMATION TO USERS

The quality of this reproduction is dependent upon the quality of the copy
submitted. Broken or indistinct print, colored or poor quality illustrations and
photographs, print bleed-through, substandard margins, and improper
alignment can adversely affect reproduction.

In the unlikely event that the author did not send a complete manuscript
and there are missing pages, these will be noted. Also, if unauthorized
copyright material had to be removed, a note will indicate the deletion.
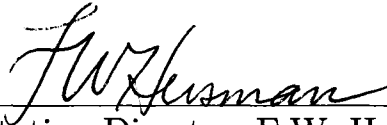
UMI®

_____

UMI Microform 3260603
Copyright 2007 by ProQuest Information and Learning Company.
All rights reserved. This microform edition is protected against
unauthorized copying under Title 17, United States Code.

ProQuest Information and Learning Company
300 North Zeeb Road
P.O. Box 1346
Ann Arbor, MI 48106-1346
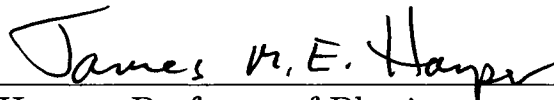
This has been examined and approved.

_____

Dissertation Director, F.W. Hersman,
Professor of Physics.

_____

S. Patz, Professor of Physics,
Brigham and Women's Hospital,
Harvard Medical School

_____

D. Meredith, Professor of Physics

_____

J. Harper, Professor of Physics

_____

I.C. Ruset,
Affiliate Assistant Professor of Physics

April 18, 2007

Date

ACKNOWLEDGMENTS

A dissertation does not just appear out of nowhere, and although it is supposed to be a contribution by one person for a Ph.D. it never is the case. The last lines of this text should be words of gratitude to all those who helped me in the course of my research for writing this thesis, and any merit in it is in large measure due to them. First and foremost, I gladly acknowledge my debt to my supervisor at UNH, Dr. Bill Hersman. Without his knowledge, perceptiveness and push I would never have finished.

I am beholden to my adviser at Brigham and Women's Hospital, Dr. Sam Patz. I could not have imagined having a better mentor for my Ph.D. Without his constant support, encouragement and advice I would not be where I am today. I am grateful to Dr. Mirko Hrovat for numerous discussions and explanations both related and not to this thesis, for the help he gave me with any challenges I faced over the time I worked with him in his lab or at BWH. He is my unlisted adviser, my other mentor.

I am especially thankful to Dr. Jim Butler for teaching so many interesting things about... well, everything! For really being a role-model of a scientist for me. I will be very happy if in my lifetime I reach even a tiny percent of what he represents.

A big "thank you" goes to my colleagues - Christina Johnson, Steve Ketel, and Eric Frederick, Drs. Silviu Covrig and Adrian Sindile and Liz Hersman for all their help in collecting the data necessary for this work. I truly enjoyed working with them.

Dr. Iulian Ruset deserves a separate mention - when I started at UNH five and a half years ago, he was the senior grad student, and he introduced me to everything around the laboratory. Every simple thing seemed very complicated and scary at the time, and he

iii

was very patient and responsive. Even though he never admits, I am sure I annoyed him greatly with all my "rookie" questions. Thank you so much!

Another tribute to my family - for their understanding, endless patience and encouragement when it was most required. Thank you for standing by me in good and bad times.

And finally, the most important "thank you" goes to my dear Mischa for his love and support through these hard years. Thank you for believing in me even when I stopped. I am forever grateful to you for keeping me sane.

And now for something completely different.

I would like to thank Dr. Ernest Illy for inventing the espresso maker.

CONTENTS

vi

LIST OF TABLES

vii

LIST OF FIGURES

x

xi

xiii

ABSTRACT

STRUCTURAL AND FUNCTIONAL IMAGING USING HYPERPOLARIZED ^{129}Xe

by

Iga Muradyan

University of New Hampshire, May, 2007

We describe applications of hyperpolarized ^{129}Xe to pulmonary imaging. Unique characteristics of this gas such as its polarizability and diffusibility in tissue allow probing important properties of the lungs. Three methods that study structure and function of the lungs, Chemical Shift Saturation Recovery ($CSSR$), Xenon polarization Transfer Contrast (XTC) and $Dixon$, and their application to human studies for the first time are the focus of this work.

$CSSR$ measures the global fractional gas transport, $F(t)$ in the lungs. Using this method the dynamics of gas exchange were studied. A model describing this process was derived and used to interpret data obtained with $CSSR$. Studies were conducted on a number of healthy subjects as well as patients with mild to moderate Interstitial Lung Disease. $CSSR$ was able to distinguish the healthy group from the rest by the measured septal thickness.

XTC is an imaging technique, in which the gas-phase signal is attenuated by inverting the spins of ^{129}Xe particles dissolved into the parenchyma. Using this technique 2D maps of the fractional gas transport, $F(t)$ occurring in the lungs were obtained. Studies were

performed at two lung volumes, and showed the at lower volumes, fractional gas transport and therefore the alveolar surface per unit volume is higher for all subjects. Difference in the fractional gas transport from apex to base was detected in the supine position with greater values at the bases. Comparison between health non-smokers and asymptomatic smokers was made. We observed a higher mean value of $F(t)$ and physiological heterogeneity in smokers compared to non-smokers. Preliminary results suggest that XTC is more sensitive to the early changes in the lungs compared to the gold standard tests, such as DL_{CO} and FEV_1.

$Dixon$ is another imaging modality, which can be used to measure local S/V. It provides a direct simultaneous measurement of the dissolved and gaseous phases of inspired Xe. It yields a 2D map of $F(t)$. Higher values of $F(t)$ accompanied by a larger spread was observed at lower lung volumes.

CHAPTER 1

INTRODUCTION

Pulmonary imaging is the least evolved branch of MRI and the reason for this being the low signal in the lungs. The signal in MRI comes from the protons in the body. There are several types of tissue of which a body is comprised and all of them contain some amount of ^1H. The soft tissue is rich with hydrogen ($\sim 90\%$), while bones contain only a tiny amount ($< 10\%$) resulting in a very strong signal from the soft tissue types and almost none from the bones. The lungs pose a different problem - while soft tissue makes up the actual structure of the lungs, volumetrically it accounts for only $\sim 20\%$ of the lung. Air fills up the rest.

Another weakness inherent in lung imaging comes from the numerous tissue-gas interfaces, that alter the magnetic field locally and result in very short signal coherence times for the spins. Recently implemented imaging techniques employed paramagnetic oxygen and gadolinium as contrast agents. They showed some promise for imaging the lung parenchyma and lung perfusion. But the signal-to-noise ratio of these measurements still has room for improvement.

To image lungs one, naturally, would be looking for a contrast agent that would fill the gaseous spaces of the lungs. Such contrast agents were found - the noble gases Xe and He. In thermal equilibrium, the polarization they produce is the Boltzmann polarization, but the signal generated from the gases will be much smaller compared to that from the tissue, since the density of the protons in the tissue is a factor of 10^3 higher than the density of

1

gas in the lungs. Consequently, the gases need to be polarized outside and inhaled later while they are still in the excited state. Fortunately, the technology for the polarized gas production was already in place and being exploited in such areas as nuclear physics.

The use of polarized gases was pioneered in 1994, when ^{129}Xe was used in medical imaging. Later ^3He imaging took over since the nuclear physics community had been dealing with helium for much longer and they were able to create polarizations very close to theoretically allowed limit. Another advantage of helium is that its gyromagnetic ratio is almost 3 times that of xenon, which automatically increases its relative SNR by the same factor. However the ^3He isotope is a by-product of a radioactive decay of tritium. The current supply of ^3He comes from the dismantling of nuclear weapons.

The case of xenon is slightly different. Although ^{129}Xe has a lower SNR, it's supply is unlimited - ^{129}Xe is present in air and can be easily extracted. The natural abundance is only 26.4%, but enrichment is readily available. The main reason for the delay in progress of xenon imaging was low levels of polarization that the researchers were able to obtain. This hurdle was cleared in 2004, when polarization levels comparable to those for helium were attained at UNH.

The main interest in using this gas in medical imaging stems from xenon's solubility in tissue. This allows imaging of not only the gas spaces but the lung tissue as well.

We will present the basics of pulmonary physiology and available diagnostic tools (Chapter 1), basics of MRI and where hyperpolarized gases fit in the framework (Chapter 2), present the experimental set-up for the studies (Chapter 3) and discuss the techniques introduced and used for imaging the pulmonary structure and function (Chapters 4-6). Each chapter describing a technique used will provide an overview of the work done un-

2

til now, details of the experiment and data analysis, presently obtained results and their discussion.

In Chapter 4 we present a technique called Chemical Shift Saturation Recovery ($CSSR$) which is a spectroscopic NMR technique, hence provides information about the lung as a whole. Using this technique, we investigate the dynamics of the gas exchange in the lungs, and provide first measurements of the tissue thickness and the surface area in humans performed *in vivo*. A model of gas diffusion into a tissue slab is introduced and applied to fit the experimental data. These results will be compared to measurements done in 1970s on fixed animal lungs and the differences will be discussed.

In Chapter 5 we will introduce a variation to an existing imaging technique, Xenon polarization Transfer Contrast (XTC). As previously implemented, XTC is a 2-breath method and has been demonstrated in anesthetized animals. To apply the XTC technique in humans, a single breath XTC method was developed, which avoids issues associated with obtaining identical gas volumes on subsequent breath-hold experiments as well as precise image registration in post-processing. We will report measurements of the mean and variance of fractional gas transport for healthy non-smokers as well as asymptomatic smokers. We will compare the results between these two groups of subjects, and correlate the fractional gas transport with the smoking history. We will compare this to the correlation of standard pulmonary function tests, such as DL_{CO} and FEV_1, with smoking history.

Chapter 6 will describe the application of the Dixon technique to pulmonary imaging. The basics of the technique will be presented, the application of the three-point separation to xenon imaging will be introduced together with the data and the discussion of the results.

The general ideas, results and conclusions of all methods introduced and used in this

3

thesis will be discussed, compared and summarized in the Chapter 7.

4

CHAPTER 2

PULMONARY IMAGING

2.1 Some Background on Lung Anatomy and Physiology

The main function of the lungs is to provide continuous gas exchange between inspired air and the blood in the pulmonary circulation. They supply oxygen and remove carbon dioxide from the body, which is then exhaled from the lungs. When healthy, the lungs preform this delicate function reliably and efficiently. However this vital organ can fall victim to a variety of ailments, such as emphysema, interstitial fibrosis etc. Each disease bears a unique mark, which could be identified by the physicians trying to produce a timely diagnosis and ultimately cure the patient. A deeper insight into the pulmonary physiology coupled with an ability to recognize the traits particular to each disease is therefore imperative in the field of diagnostic medicine. The large numbers afflicted by some form of pulmonary disorder urge the expansion of the current arsenal of capabilities in this field.

The gas exchange in a unicellular organism is governed by Fick's law, according to which the rate of gas exchange is directly proportional to the gradient of the concentration, ∇P, of gas near the surface and the area of this surface S_A. It however decreases linearly with the thickness r through which it must diffuse:

$$R \propto S_A \frac{\nabla P}{r} \tag{2.1}$$

5

In more complex organisms, the amount of surface area per tissue mass is much smaller. This necessitates a mechanism which would equip the body with an adequate gas-exchanging capability. For most insects this is accomplished by tracheoles - a network of tubes, that conduct the air to individual body cells. In humans, on the other hand, gas exchange takes place through alveoli - millions of bubble-like endings, where the air pumped by the lung from the atmosphere diffuses into the blood (Figure 2.1).Unlike the case with
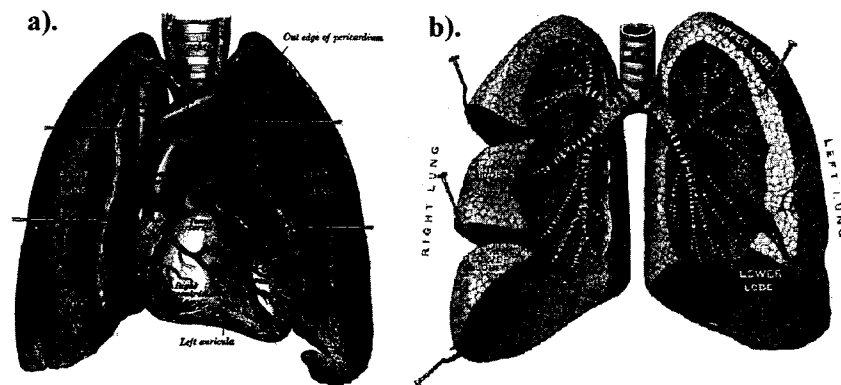
Figure 2.1: Human lungs and heart. (Gray's Anatomy of the Human Body, 20th ed., 1918)

the insects, oxygen is supplied to the body cells in the other organs by the erythrocytes in blood.

The air is inhaled through the nose and/or mouth and guided by the upper respiratory tract consisting of the nose, the pharynx, the larynx and the trachea. Here it is filtered from airborne particles, humidified and warmed. Further down the road, lies the lower respiratory tract which includes the bronchial tree and alveolar space, where all of the gas exchange takes place.

The trachea splits into the left and the right principal bronchi. The former is bent away from the trachea at a slightly sharper angle, making the gas more likely to enter the right

6

Conductive Zone	Trachea		0
			1
	BR		2
			3
	BL		4
			↓
	TBL		
Respiratory Zone	RBL		17
			18
			19
	AD		20
			21
			22
	AS		23
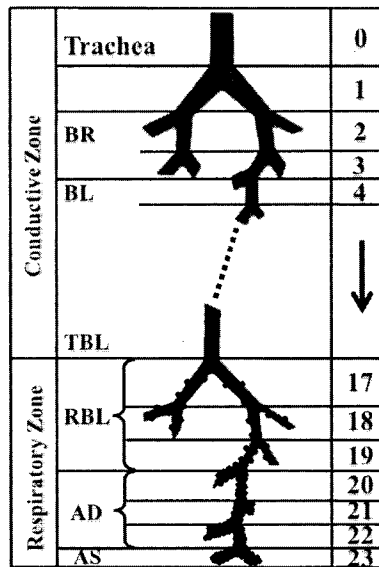
Figure 2.2: Model of airway branching (redrawn from E.R.Weibel, In *Morphometry of the Human Lung*).

lung. Inside the lungs, the primary bronchi subdivide into the secondary, or lobar, bronchi. Each of the secondary bronchi supplies one lung lobe - 3 lobes (upper, middle and lower) in the right lung and 2 lobes (upper and lower) in the left lung. In total there are up to 23 airway divisions between the trachea (0th order) and the alveoli (23rd order). Figure 2.2 shows this structure - the standard model, described by Weibel [19]. Table (2.1) provides some parameters of the lung anatomy.

The last few generations constitute the so-called respiratory zone, where terminal bronchioles feed into the respiratory bronchioles that lead into the alveolar ducts. The zone culminates as the latter feed into alveolar sacs $\left(23^{rd} \text{ order}\right)$. There are about 300 million alveoli in the lungs.

They are approximately $300\mu m$ in diameter (Figure (2.4)) and add up to an area of

Generation	Order	D, mm	L, mm	Number	Area, mm^2
Trachea	0	18	120	1	2.54×10^4
Bronchi	1	12.2	48	2	2.33×10^4
	2	8.3	19	4	2.13×10^4
	3	5.6	8	8	2×10^4
Bronchioles	4	4.5	13	16	2.44×10^4
Terminal	5	3.5	10.7	32	3.11×10^4
Bronchioles	16	0.6	1.7	6×10^4	18×10^5
Respiratory	17	0.5	1	5×10^5	10^7
Bronchioles	19				
Alveolar Ducts	$20 - 22$				
Alveolar Sacs	23	0.4	0.5	3×10^8	10^8

Table 2.1: Standard model by Wiebel. It describes the parameters of the lung anatomy for 23 generations, starting from the trachea and ending at the alveoli.

8
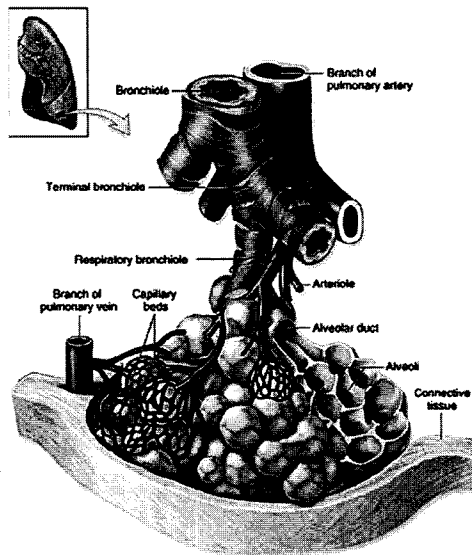
Figure 2.3: Lower respiratory tract (The McGraw-Hill Companies, Inc.). Bronchi subdivide

into bronchioles which lead to alveolar ducts. The latter feed into alveoli, that are embedded

in a capillary mesh. This is the gas exchange site.

9
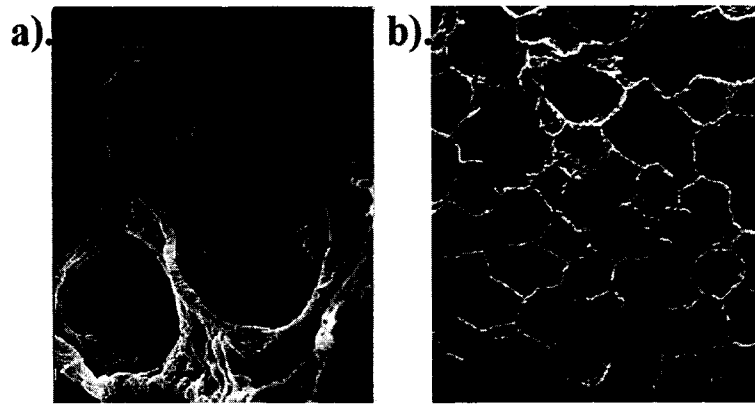
Figure 2.4: Alveoli and alveolar walls in the lungs [27]. Average alveolus has a diameter of ~ 300 μm, while the average barrier thickness between two neighboring alveoli is $\sim$ $5 - 10$ μm

about 100 m^2. The alveoli are wrapped in a fine mesh of capillaries (Figure(2.3)), the alveolar walls are extremely thin making the gas - blood barrier about 2 μm thick which together with the huge alveolar surface area makes gas exchange very efficient.

In the respiratory tract the gas is moved first by tidal flow in the large airways and then by diffusion in the small airways (division 17 and smaller). Pulmonary gas exchange is driven by diffusion due to the concentration gradient present in the lungs.

There are two aspects of blood circulation in the lung: whereas pulmonary circulation is a part of the process of gas exchange with the alveoli, bronchial circulation supplies blood to the parenchyma (tissue of the lung itself).

The efficiency of gas exchange occurring in the lungs greatly depends on the thickness of the alveolar walls and the surface available for gas exchange. Therefore these parameters are the focus of many morphological studies. Most of the measurements were done in the 1960s and 1970 on fixed lungs of excised animals ([24], [19], [23], [20]). Gil *et al.* [39]

10

performed the most careful measurements on air and saline filled animal lungs fixed by vascular perfusion [38]. They noticed a difference in the alveolar surface geometry and the degree of capillary bulging in air and saline-filled lungs. Also, they determined that the alveolar surface area S_A depends on lung volume V_A as $S_A = kV_A^{0.33}$ for air-filled and as $S_A = kV_A^{0.58}$ for saline-filled lungs. Since the available explorative methods are inherently invasive the opportunity to study the lung structure in vivo had not yet presented itself.

Certain types of diseases, including Chronic Obstructive Pulmonary Disease ($COPD$) and Interstitial Lung Disease (ILD), impair lung's ability to exchange gas. $COPD$ is an umbrella term used for describing lung disease associated with airflow obstruction. Most generally, emphysema and chronic bronchitis alone, or in combination, fall into this category. Chronic bronchitis is the inflammation, and eventual scarring, of the bronchi; emphysema is an airspace enlargement secondary to alveolar septal destruction. Thus $COPD$ affects both parameters crucial for efficient gas exchange - tissue thickness and surface area. ILD, on the other hand targets the parenchyma by causing inflammation of the alveolar walls and interstitium, resulting in pulmonary fibrosis. This stiffens the lungs, and compromises the gas exchange and the breathing process.

$COPD$ is the fourth leading cause of death in the United States. The National Heart, Lung, and Blood Institute reports that 12.1 million adults were diagnosed with $COPD$ and about 24 million have evidence of impaired pulmonary function, indicating that the disease is under-diagnosed. This can be attributed to the anatomical definition of the disease and the diagnostic tools available.

Current methods used widely to diagnose lung function are pulmonary function tests (PFT), X-rays, computer tomography etc. We will review them briefly.

11

2.2 Existing Pulmonary Tests and Imaging Modalities

Currently there are a number of diagnostic tests capable of assessing certain aspects of lung function. These are global tests such as PFT and Spirometry on the one hand, and imaging tests providing local information such as X-rays, CT and MRI on the other. Here we will review these diagnostic tools and find the place where Xenon imaging fits in.

2.2.1 Pulmonary Function Tests

Pulmonary function tests (PFT) are a set of tests that yield important *global* information about lung function. Complete PFT usually refers to spirometry before and after the administration of a bronchodilator, measurements of lung volumes, and measurement of diffusion capacity.

Static Lung Volumes and Capacities   Static lung volumes reflect the elastic properties of the lungs and the chest wall. Vital capacity (VC) is the maximum volume of air that can be expired slowly after a full inspiratory effort. Simple to perform, it is one of the most valuable measurements of pulmonary function. Since as a restrictive lung disorder (e.g., pulmonary edema, interstitial fibrosis) progresses it decreases VC, the course of such a disorder and its response to therapy can be monitored by tracking VC and diffusive capacity.

Forced vital capacity (FVC), similar to VC, is the volume of air expired with maximal force. It is usually measured along with expiratory flow rates in simple spirometry (see below, *Dynamic Lung Volumes and Flow Rates*). The VC can be considerably greater than the FVC in patients with airway obstruction. During the FVC maneuver, terminal

12
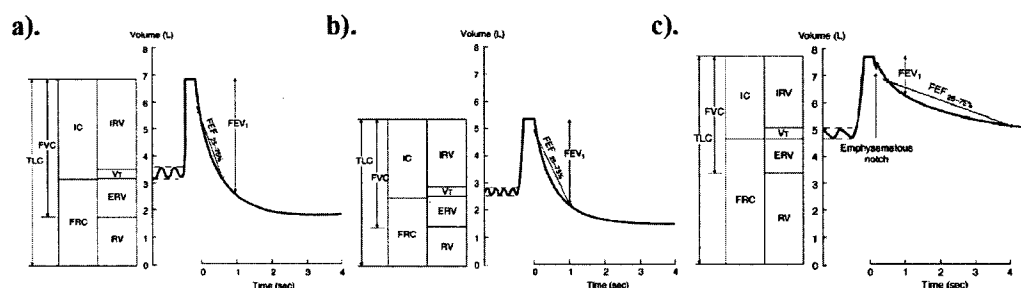
Figure 2.5: Lung volume measurements from a PFT lab in a normal healty human (a), a patient with airway obstruction (b) and a patient with an emphysema (c).

airways affected by the disease close prematurely (i.e., before the true residual volume is reached), trapping gas hence preventing its measurement by the spirometer.

Total lung capacity (TLC) is the total volume of air within the chest after a maximum inspiration. Functional residual capacity (FRC) is the volume of air in the lungs at the end of a normal expiration when all respiratory muscles are relaxed. Physiologically FRC is the most important lung volume because it corresponds to the exhalation volume for normal tidal breathing range. Outward elastic recoil forces of the chest wall tend to increase lung volume but are balanced by the inward elastic recoil of the lungs, which tends to reduce it; these forces are normally equal and opposite at about 40 % of TLC. Loss of lung elastic recoil in emphysema increases FRC. On the other hand, the increased lung stiffness in pulmonary edema, interstitial fibrosis, and other restrictive disorders decreases FRC. The inspiratory capacity (IC) is the difference between TLC and FRC.

The FRC has two components: residual volume (RV), the volume of air remaining in the lungs at the end of a maximal expiration, and expiratory reserve volume (ERV); $ERV = FRC - RV$. The RV normally accounts for about 25 % of TLC (Figure 2.5).

13

Changes in RV are correlated to those in FRC with two exceptions: In restrictive lung and chest wall disorders, RV decreases less than FRC and TLC (Figure 2.5), and in small airways disease, premature closure during expiration leads to air trapping, so that the RV is elevated while the FRC remains close to normal. In $COPD$ and asthma, RV increases more than TLC, resulting in some decrease in VC (Figure 2.5).

Dynamic Lung Volumes and Flow Rates Dynamic lung volumes reflect the caliber and integrity of the airways. Spirometry (Figure 2.5) records lung volume versus time during an FVC maneuver. Forced expiratory volume in 1 sec (FEV_1) is the volume of air forcefully expired during the first second after a full breath and normally accounts for $> 75\%$ of the FVC. This value is recorded both as an absolute value and relative to FVC ($FEV_1\%FVC$). The mean forced expiratory flow during the middle half of the FVC ($FEF25-75\%$) is the slope of the line that intersects the spirographic tracing at 25% and 75% of the FVC. The $FEF25-75\%$ is less effort-dependent than the FEV_1 and is a more sensitive indicator of early airway obstruction.

Diffusing Capacity The diffusing capacity for carbon monoxide(DL_{CO}) can be determined from a single breath (DL_{COSB}). The patient inspires a known small amount of carbon monoxide (CO), holds his breath for 10 $sec.$, then exhales. A sample of alveolar (end-expired) gas is analyzed for CO, and the amount absorbed during that breath is then calculated and recorded in $mL/min/mm\ Hg$.

A low DL_{CO} likely reflects abnormal ventilation/perfusion ratios ($\dot{V}/\dot{Q}$) in diseased lungs rather than physical thickening of the alveolar-capillary membrane. However, this

14

test relies on the availability of Hb for CO and thus is affected by the volume of blood and the quantity of desaturated Hb in the lungs at the time of testing. The DL_{CO} is low in processes that destroy alveolar-capillary membranes (e.g., emphysema and interstitial inflammatory or fibrotic processes) and in severe anemia, in which less Hb is available to bind the inhaled CO. The DL_{CO} is artificially low if the patient's Hb is already occupied by CO (e.g., if he/she smokes within several minutes of the test).

<u>Small Airways Studies</u> In a normal lung, bronchi that are below 2 mm in diameter constitute about 10% of the total airway resistance, but their total surface area is large. Diseases affecting primarily the small (peripheral) airways can be extensive yet not reflect on airway resistance or any tests dependent on it (e.g., FEV_1). This is true of early obstructive lung disease and interstitial granulomatous, fibrotic, or inflammatory disorders. The status of the small airways is reflected by the FEF25 − 75% and by expiratory flow rates in the last 25 to 50% of the FVC.

Despite their obvious value, PFTs only impart information pertaining to the *total* lung function and yield very little, if any, *regional* information about lung function thus making it impossible to diagnose a disease in early stages. Regional information may give increased sensitivity to an early disease which brings us to the available imaging techniques.

2.2.2 Medical Imaging

Imaging became possible about a hundred years ago, when Wilhelm Conrad Röntgen accidentally discovered X-rays. It opened new opportunities in diagnostic medicine making it possible to look within a patient's body without having to slice it open.

Medical Imaging started with the 2-dimensional x-ray image in 1895 (Figure 2.6).

15
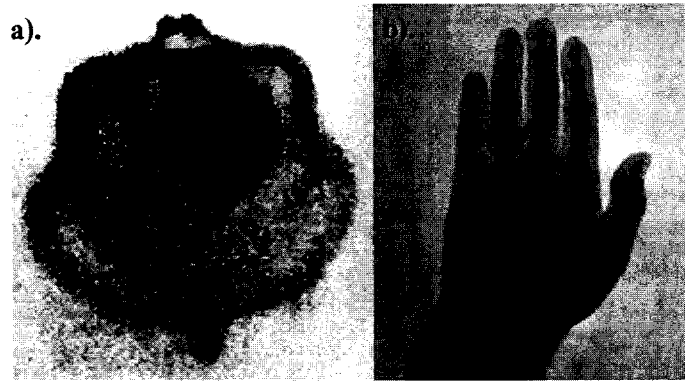
Figure 2.6: The 1st X-rays images ever made.

These images displayed the contents of objects as if you could see through them. A disadvantage of these techniques was that the organ of interest could be partially covered by other structures which made the diagnosis more difficult. In the 1970's Hounsfield developed the first x-ray computer tomograph, which allowed to clearly see regions deep inside the body without the overlapping signal from other organs. By combining slices on top of each other one can reconstruct a 3-dimensional image of the body. Now the organs and structures have a spatial extent that can be measured. Other well known imaging modalities are MRI, SPECT and PET.

X-rays, computed tomography (CT) and magnetic resonance imaging (MRI) can indeed produce very highly detailed images of human organs. However, sometimes it is more important to acquire images which visualize the function of an organ or the blood flow. While X-rays, CT and MRI are used to image morphological structures, SPECT and PET are used to display the biological function of organs in order to visualize physiological processes. This can be achieved by imaging the decay of radio isotopes which are bound to molecules with known biological properties (PET, SPECT). These techniques are very

16

useful when looking for abnormalities like cancer or to understand physiological processes. By taking advantage of both, the morphological and functional images one can have a detailed view of the structure of an organ fused together with the information about its function.

X-Rays   X-rays is the best known and the oldest medical imaging technique. It was discovered by Wilhelm Conrad Röntgen, a professor at the University of Würzburg. Later in the evening of November 8, 1895, working in a darkened room, something unusual caught his eye: when an electric discharge occurred in a vacuum tube with which he was experimenting, a nearby piece of paper coated with a chemical compound of barium, platinum, and cyanide produced a glow. The glass tube was completely surrounded by black cardboard so no light from it could be reach the coated paper. But, something must have penetrated the cardboard, and caused the glow of the paper's coating. The fluorescence of the barium compound was in fact induced by the X-rays. The image above (2.6) is the first radiograph ever made, a clasp purse with a key and a dense box.

Modern x-ray tubes consist of an evacuated glass tube which contains an anode and a cathode. A high potential (50 - 120 KV) is applied between the anode and the cathode. The cathode contains a heated filament which cooks electrons off into the vacuum. These electrons accelerate due to the high voltage and strike the anode. The rapid deceleration of the electrons produces the X-rays. The higher the potential the shorter the wave length and the harder the x-rays. About 98% of the x-rays are absorbed by the patient. Only 1 or 2 percent of them reach the film. The absorption increases with the number of protons, therefore heavier elements absorb more then the light ones. Bones, which consist of calcium,
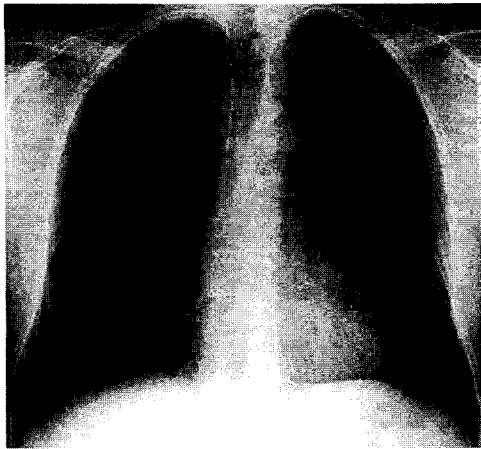
Figure 2.7: Chest radiograph of a normal healthy male.

appear whiter then soft tissues, which are mostly built from hydrogen and carbon.

While propagating through the patient the X-rays are attenuated through processes of scattering and absorption. These phenomena result in the characteristic pattern, used by the diagnostician.The chest radiographs (CXR) are the most popular tools in the radiology department (Figure2.7). They are commonly accepted as a good test to estimate the general state of the patient, whether this is related to cardiac or lung condition. It is then only natural that this method does not provide the most sensitive test.

X-rays is a *transmission* imaging modality (which refers to the type of imaging where the source of radiation is outside of the body. The radiation passes through the body and is detected on the other side) as well as *projection* imaging modality (where each pixel in the image corresponds to the information from all points traversed by the ray propagating through the patient) (Figure 2.8).

X-ray photons have sufficient energy to cause ionization when they interact with matter (it requires $\succeq 30\,\mathrm{eV}$ to cause an ionization event). Hence the x-rays can break molecular

18

Transmission Emission
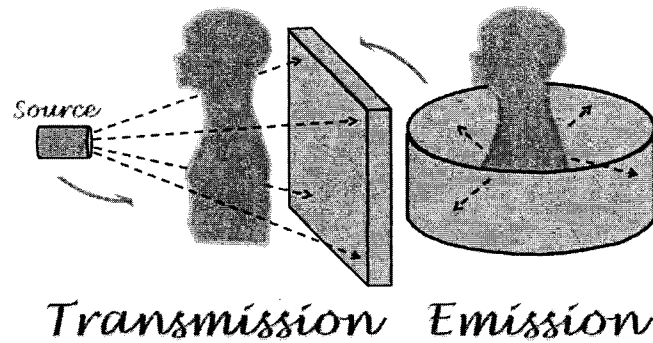
Figure 2.8: Two imaging modalities - transmission imaging refers to the type of imaging where the source of energy is outside the body, while emission is the type with the energy source placed inside the body.

bonds. In DNA molecules this can cause changes in function leading to cancer or genetic defects. At high X-ray doses, so many molecules are damaged that cells can lose their function and die resulting cataracts, skin burns, etc.

Computed Tomography (CT) It is said that CT is "the greatest legacy" of the Beatles [81] - the profit from their record sales allowed EMI labs to fund the research of Godfrey N. Hounsfield on computer tomography. Hounsfield came up with his idea in 1967 and built the prototype in 1971. Independently, Allan MacLeod Cormack, physics professor at Tufts University, developed the theoretical groundwork of CT scanning. He published two papers in the Journal of Applied Physics in 1963 [2] and 1964 [3], but they generated very little interest until Hounsfield's application of this calculations. Hounsfield and Cormack shared the 1979 Nobel Prize in Physiology and Medicine.

Originally CT scanners were developed to study the brain, but other applications soon became apparent and today computed tomography of the chest, the abdomen and pelvis

19

is commonplace. The collected data points are rendered by a computer into a tomographic image of the organ in question. The advantage of tomographic image over projection image is its ability to display the anatomy in a slab of tissue in the absence of over- or under-lying structures. CT substantially reduced the need for exploratory surgery.

Imaging Principles CT imaging is based on the principle that the internal structure of an object can be reconstructed from multiple X-ray projections. The CT image is a 2D representation of a 3D cross-sectional slice, the 3rd dimension being the slice thickness. Helical CT is a major technical advance that allows continuous scanning while the patient is slowly moved trough the CT scanner. In this technique, patient translation and X-ray

Figure 2.9: The trajectory of the X-ray source in spiral CT. In a helical CT the patient is slowly moved through the CT gantry while the x-ray source is rotated, resulting in a spiral-like curve

source rotation occur simultaneously during data acquisition, hence the X-ray source traces a helical curve in relation to the patient, as shown in Figure (2.9). The multiple 2D images collected throughout such a session are combined in the process of image reconstruction to produce a 3D image.

20

Multi-Slice CT   A CT image is composed of multiple picture elements (typically a 512 by 512 matrix) known as pixels. A pixel is a unit area, that is, each square on the image matrix, which reflects the attenuation in a unit volume of tissue, or a "voxel" (the area of the pixel multiplied by the thickness of the slice). This volume averaging results in a loss of spatial resolution: the thicker the slice the lower the ability of CT to resolve small structures. On the other hand as section thickness decreases, noise increases, and images are grainier as a result.
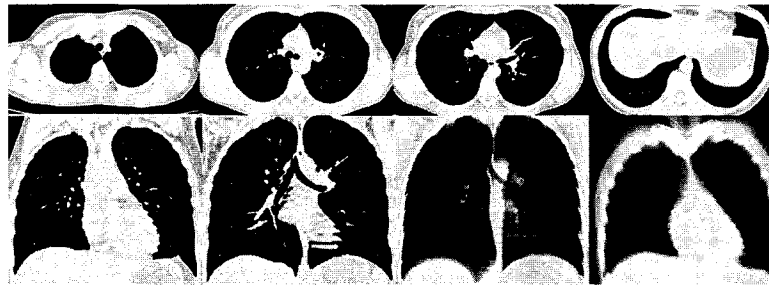
Figure 2.10: Multi-slice CT in both axial and saggital directions. The standard reconstruction in CT smoothes the image and reduces visible image noise for an optimal assessment of the lung parenchyma.

Using multidetector CT, the entire chest scan may be completed during a 8s breath-hold while using a 0.6 or 1.25 *mm* slice thickness. The combination of fast gantry rotation time, the simultaneous acquisition of the patient's electrodiogram, and specialized reconstruction techniques can provide nearly motion-free images during cardiac systole or diastole.

Image Reconstruction   The continuous data acquisition during a CT scan produces multiple overlapping images thus increasing spatial resolution. These overlapping images allow production of high quality multi-slice (2.10) or 3D (2.11) reconstructions while avoiding

21

extra exposure to radiation. This also eliminates motion artifacts that otherwise degrade the image quality.

Figure 2.11: Multi-Slice high resolution CT data can be used to render 3D lungs.

High resolution CT scans are used to evaluate the extents of chronic interstitial processes such as emphysema, fibrosis, and so forth.

Radiation Exposure Although CT is only 4% of all medical X-ray examinations, it represents 40% of the collective radiation dose. The growth of CT is dramatic: from 2.8 million CT exams in 1981 to 20 million exams in 1995.

As mentioned earlier, absorption of energetic photons by a living tissue damages its chemical bonds and leads to cell deterioration. One of the gravest consequences of such damage is the alteration of the DNA. Brenner et al [11] conclude that additional 1 in 1500 will die of radiologically induced cancer each year in the US. Another study of children receiving head CT, conducted by Hall et al [60] showed that high doses of radiation result in decreased school attendance and lower cognitive test scores. There has been no detectable

22

increase in genetic defects related to radiation in a large sample (80,000) of Hiroshima and Nagasaki survivors' descendants, including: congenital abnormalities, mortality (including childhood cancers), chromosome aberrations, or mutations in biochemically identifiable genes [84]. However, exposed individuals who survived the acute effects were later found to suffer increased incidence of cancer of essentially all organs.

All this brings us to a thought that if there were another diagnostic test that could answer if not all then some of the questions addressed by CT, without exposing subjects to any radiation, then the number of radiologically induced cancer cases would decrease dramatically. This is especially important in the case of the younger generation which is more sensitive to radiation exposure.

2.2.3   Nuclear Imaging

Nuclear medicine began in the late 1930's when radioactive iodine was employed to investigate a thyroid disease. The main difference of nuclear medicine from X-rays is that the source of emission is contained inside the body (Figure 2.8). Clinically the patients are injected with a radioactive material whose decay can be measured. These radioactive pharmaceuticals have different properties and concentrate in a defined organ. Over time the activity can be measured to monitor the function of the organ. Nuclear medicine is also referred to as functional imaging rather then morphological imaging like X-rays or CT.

Depending on the method of the radiopharmaceuticals' disintegration nuclear medicine can be split into two main groups:

* Single Photon Emission

* Positron Emission

SPECT The radioactive isotopes used for Single Photon Emission disintegrate by releasing

a single γ quantum. These can be measured with a $\gamma-$camera. Then a computer is used

to apply a tomographic reconstruction algorithm to multiple projections in order to render

a 3D image of the distribution of the radioactive material within the patient.

SPECT is used to generate functional images of organs, to measure local blood flow

and metabolism. As in X-ray CT, SPECT imaging involves a rotation of a photon detector

array around the patient to acquire data from multiple angles. Radionuclides used in
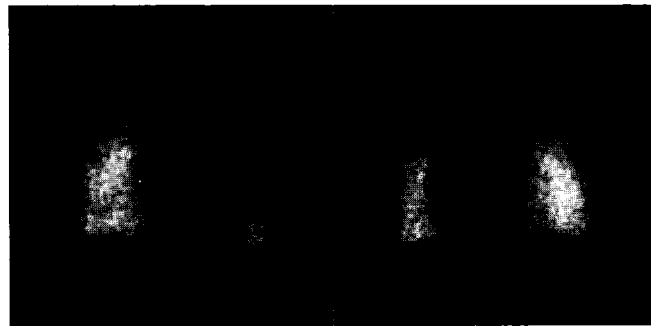
Figure 2.12: Lung imaging with SPECT. It is evident that SPECT does not provide enough

resolution for early diagnosis of lung impairment.

SPECT imaging usually emit a single photon of about $140\,KeV$, as opposed to PET which

uses two high energy photons of about $512\ KeV$. Because only a single photon is emitted,

a collimator has to be used for scatter correction. This decreases the resolution and the

efficiency compared to PET. Although SPECT imaging resolution is lower then that of

PET, the availability of new SPECT radiopharmaceuticals and the practical and economic

aspects of SPECT instrumentation make this method of functional imaging attractive for

a lot of clinical studies.

24

<u>PET Imaging</u> Positron Emission Tomography (PET) is used in clinical medicine and biomedical research to create images that show anatomical structure as well as how certain tissues perform their physiological functions. Radioactive nuclei are introduced to the body, where they decay and emit positrons, that then interact with the electrons present in the tissue and annihilate. This process can produce high energy photons, γ quanta (Figure 2.13). Annihilation might take place directly or via the formation of a positronium, a state in which an electron and a positron form a "light hydrogen atom" bound by Coulomb attraction. In the lowest energy states the total spin of the system is 0 or 1 depending on whether the spins are anti-parallel or parallel. If the annihilation occurs in the spin 0
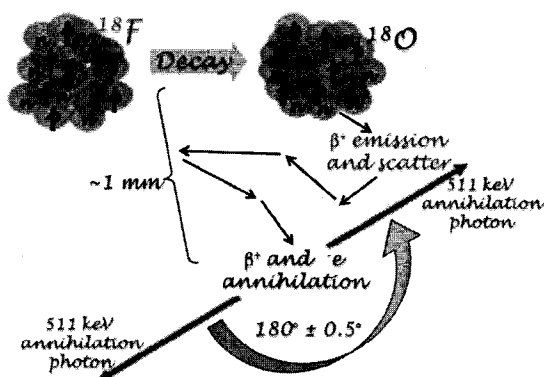
Figure 2.13: A diagram of how PET imaging works.

state, the process is very fast ($<$ 100 ps) and two photons are created and emitted at 180°, each with an energy corresponding to the mass of the electron, 511 keV. The directions of emission are restricted by the conservation of momentum. Before the annihilation both the total linear momentum $\vec{p}$ and angular momentum $\vec{l}$ are zero (in the electron's frame of reference) so both $\vec{p}$ and $\vec{l}$ must both be zero after annihilation. This is accomplished by emitting two spin 1 photons in opposite directions. Spin 1- annihilation creates three

25

photons and the available energy is shared by the three photons. This process is of no interest in PET applications since the three photons cannot easily be used to reconstruct the annihilation point. Fortunately it also is less probable.

Once emitted, positrons travel only a short distance away from the parent atom before combining with an electron and annihilating. When a crystal is struck by a photon of adequate energy, light is emitted. However, only when an opposing pair of detectors register photons in coincidence, is the annihilation event registered and processed. The simultaneous detection of the photons reveals their line of origin. A computer then uses many such lines to construct a three-dimensional image of an organ system [72]. The information obtained from a PET scan, coupled with data from a CT scan, provides a fuller picture of not only the structure but also the function of the organ in question (Figure 2.14).
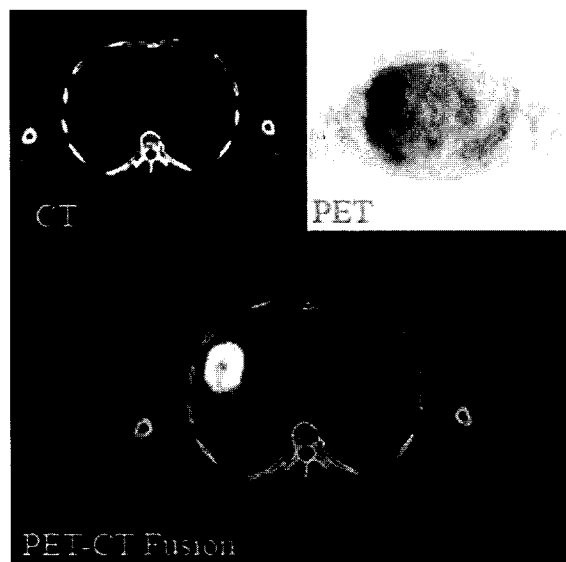
Figure 2.14: CT and PET images fused together. The information obtained from a PET scan, coupled with the from a CT scan, provides a fuller picture of not only the structure but also the function of the organ in question

26

A disadvantage to the short half-lives of PET radiotracers is the need for an on-site cyclotron and staff to produce these radiotracers or a distribution center in close proximity to the PET center. Both add to the overall cost of PET scans. Another disadvantage of PET is the scan time - a single scan can take up to 45 minutes in order to accumulate sufficient statistics.

2.2.4 Magnetic Resonance Imaging (MRI)

Magnetic Resonance Imaging (MRI) is based on a phenomenon known as the Nuclear Magnetic Resonance (NMR) and in the earlier days was referred to as NMR Imaging. Since the word nuclear was associated with ionizing radiation exposure, which is not used in this type of imaging, the word was dropped from the name and it became Magnetic Resonance Imaging. A detailed description of the concept of NMR and image formation in MRI will be given in later chapters. However we will give very short description of the technique and how it fits in with the rest of imaging modalities.

The conventional MRI detects the presence of protons in a body by subjecting them to a large magnetic field to polarize their nuclear spins and then excite them with radio frequency radiation. This is followed by their relaxation from this magnetic interaction. This relaxation gives rise to a signal in MRI.

This signal is proportional to the magnetic field applied to the protons, and can therefore be attributed to a specific location in the tissue in the presence of known field gradients. This provides the information to map the proton density distribution in the tissue. Since the MRI uses proton signal, it is particularly well suited for the imaging of soft tissue, like the brain, the eyes, and other soft tissue structures. Parts of the body, that do not contain

27
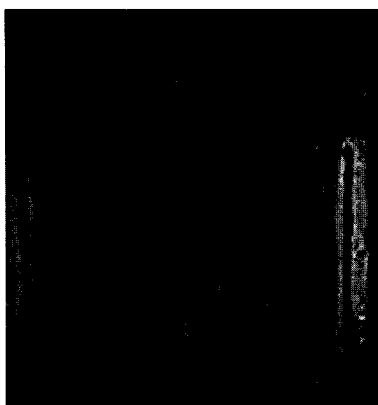
Figure 2.15: MRI of a human chest. Since lungs are mostly filled with air, there is not much MRI signal present there.

a lot of hydrogen will give very little if any signal (Figure 2.15).

In the context of lung diseases and their treatment it is important to understand the multitude of the lung's properties, structure and function. Whereas general knowledge of lung's function and anatomy has been sufficient in order to create methods for treating certain aspects of pulmonary ailments, the deepening of our comprehension of the subject is far from complete.

28

CHAPTER 3

THEORY BEHIND MRI - NUCLEAR MAGNETIC RESONANCE

3.1 The Timeline

It all started in 1946, when two scientists independently from each other observed a phenomenon based on the magnetic properties of certain nuclei, called "Nuclear Magnetic Resonance", or NMR [26], [17]. Both scientists, Felix Bloch and Edward M. Purcell, were awarded the Nobel Prize in Physics in 1952.

The theoretical and experimental groundwork leading to the discovery of NMR, was done in 1920's: the idea of the nuclei possessing an intrinsic spin was suggested by Wolfgang Pauli in 1924 followed in 1925 by an introduction of the spinning electron concept by Uhlenbeck and Goudsmit. The theoretical framework fitting the concept into the year-old quantum mechanics of Edwin Schrödinger and Werner Heisenberg, was developed by Pauli and Darwin in 1927. In 1922, Otto Stern and Walther Gerlach measured the effect of the nuclear spin by deflecting a beam of silver atoms in a magnetic field.

The next decade was marked by an intensive search for a technique to measure this nuclear magnetic moment. One of the major centers was Rabi's laboratory at Columbia University in New York. In 1937, with the help of Cornelis Gorter, they successfully demonstrated such a method. Gorter himself has studied this problem extensively, but failed to find a solution. Together they were able to develop a method which allowed them to succeed [36]. The term "nuclear magnetic resonance" is attributed to Rabi. Another scientist struggling with the measurement of the nuclear magnetic moment was Yevgeni

29

K Zavoisky, Kazan University professor from the Soviet Union. Towards the end of the Second World War he discovered the electron spin resonance [14].

However, it were Bloch and Purcell whose work paved the way for future NMR research [86].

Their success triggered a rapid development of the NMR techniques in the following years. Extensive studies of the relaxation times in solids and even in biological media ensued: the first measurements of the relaxation times in a tissue were reported in 1956 by Odeblad and Lindström [13], then Bratton et al [8] measured T_1 and T_2 relxation times in the skeletal muscle of a frog; Ligon reported the measurement of the NMR relaxation in the arms of living human subjects (1967) [80]. The first results of NMR measurements in a living animal came from Jackson and Langham in 1968 [42]. In 1971 Hansen added brain tissue studies to the realm of NMR measurements [46].

In 1971 Raymond Damadian from Downstate Medical Center in Brooklyn showed that the nuclear magnetic relaxation times of normal and tumorous tissues differed [69]. Damadian's description of relaxation time changes in cancer tissue was one of the main impetuses for the introduction of NMR into medicine.

Needless to say that alongside with the application of already existing techniques new approaches and methods were developed. Erwin L. Hahn in 1950 introduced a method, called "spin echo" whereby he applied field gradients to study molecular diffusion in liquids [15]. In 1951, Roger Gabillard from Lille, France studied T_2 relaxation using one-dimensional gradients [64]. Carr and Purcell studied the effects of the diffusion on the signal in nuclear magnetic resonance using magnetic field gradients in 1954 [33].

The 70's brought a breakthrough in the technical aspects of the NMR method. All

the experiments in the previous decades were one-dimensional, hence carried no spatial information. That is until September of 1971, when Paul Lauterbur of the State University of New York at Stony Brook applied magnetic field gradients in all 3 dimensions and used the back-projection technique to create NMR images. The first NMR images were published in March 1973 (Figure 3.1); these were images of two water tubes [61].
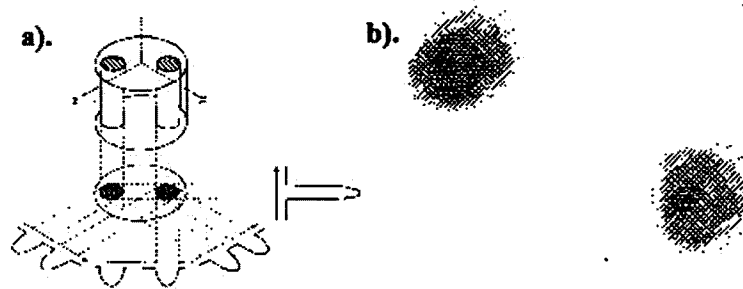
Figure 3.1: The first NMR image obtained by Lauterbur in 1973 [86]. This is an image of two water tubes placed in the imaged volume.

Next year brought more images, including those of living animals [62].

As mentioned above, the field gradients had been used before - they were essential in the diffusion studies. However, it was Lauterbur's idea that introduced the NMR field to imaging. He was awarded the 2003 Nobel Prize in Medicine or Physiology for his contribution to the invention of magnetic resonance imaging.

In 1974 Richard Ernst attended a talk given by Lauterbur at a conference in Raleigh, NC. While at the conference, Ernst realized that Lauterbur's back-projection is not the only way to perform imaging. Instead, one could use controlled magnetic field gradients in the time domain. This led to the development in 1975 of the basic, or Fourier reconstruction method in imaging, that is routinely used today [1]. Ernst received the 1991 Nobel Prize

31

in Chemistry for his work in Fourier Transformed NMR and MRI.

Late 70's brought the first human images: Raymond Damadian demonstrated MRI of the whole body in 1977 [63], while Hinshaw, Bottomley, Neil Holland acquired an image of the wrist [12]. In this same year, Peter Mansfield, leading a group of scientists in Nottingham, England, developed the echo-planar imaging (EPI) technique. In 1978 Mansfield presented his first image of the abdomen. The EPI technique will be developed in later years to produce images at video rates (30 ms / image). Mansfield shared the 2003 Nobel Prize in Medicine or Physiology for the invention of magnetic resonance imaging.

3.2 The Basics of NMR.

Magnetic resonance is a phenomenon in magnetic systems that possess both an orbital magnetic moment and an angular momentum. Certain atomic nuclei, like hydrogen, when placed in a static magnetic field, will assume one of the two states: a state with higher or lower energy. In accord with Zeeman effect, the energy difference between the two states is linearly proportional to the strength of the external magnetic field (Figure 3.2). Under thermal equilibrium conditions there is a small difference in the populations of the two energy states in favor of the lower state. The transition of the nucleus between the lower and higher energy states can occur by means of emitting or absorbing a photon, with energy equal to $\Delta E = E_2 - E_1$. When such photon is absorbed, the system will move to the higher energy state with energy E_2, from which it can return to the thermal equilibrium by emitting a photon with the energy equal to $\Delta E = \hbar\omega$, where ω is the photon's frequency. The emitted energy can be measured using an RF coil. This signal carries information specific to the chemical composition of the sample.
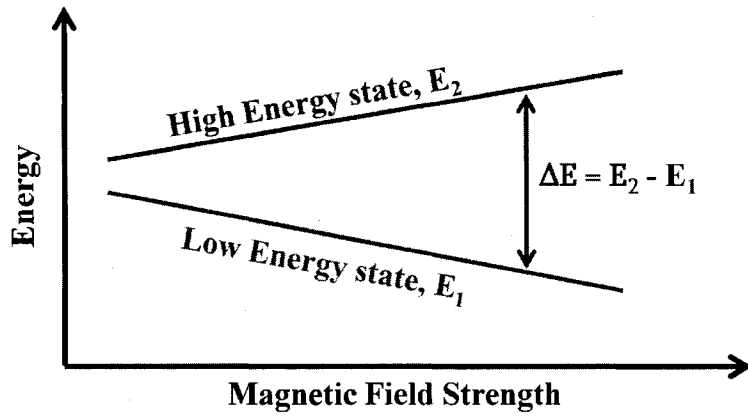
Figure 3.2: The energy level splitting in the nuclei exposed to a static magnetic field. The difference in the energy between the two levels is linearly proportional to the strength of the external field.

3.3 Quantum mechanical picture.

3.3.1 Spin in a magnetic field

A system such as a nucleus can consist of many particles coupled together, hence in any given state the nucleus possesses a total magnetic moment $\vec{\mu}$ and a total angular momentum $\vec{J}$. The two operators are in fact parallel, so that we can write

$$\vec{\mu} = \gamma \vec{J} \tag{3.1}$$

In order to interpret the parallel and antiparallel relative orientations of the two operators let's consider the matrix elements. If we define a dimensionless angular momentum operator $\vec{I}$

$$\vec{I} = \frac{h}{2\pi} \vec{J} = \hbar \vec{J} \tag{3.2}$$

33

then I^2 has eigenvalues $I(I+1)$ with I being either integer or half-integer. The eigenstates of each component $\vec{I}$ (e.g. I_z) are also eigenstates of I^2, therefore a simultaneous measurement of I^2 and I_z is possible. We will denote by m the eigenvalues of I_z. m can assume $2I+1$ values: $I, I-1, ..., -I$. The Eqn. (3.1) is then

$$\langle I \ m | \mu_{x'} | I \ m' \rangle = \gamma \frac{h}{2\pi} \langle I \ m | I_{x'} | I \ m' \rangle \tag{3.3}$$

where $\mu_{x'}$ and $I_{x'}$ are the components of $\vec{\mu}$ and $\vec{I}$ along some arbitrary direction x'.

When a magnetic field $\vec{B}$ is imposed on a nucleus, it produces an interaction energy of the nucleus of $-\vec{\mu} \cdot \vec{B}$. Therefore the spin Hamiltonian will be

$$H = -\vec{\mu} \cdot \vec{B} \tag{3.4}$$

If we take the field to be B_o along the $\hat{k}$ direction, we will have

$$H = -\gamma \hbar B_o I_z \tag{3.5}$$

Evidently, the eigenvalues of this Hamiltonian are multiples of $(\gamma \hbar B_o)$. Hence the allowed energies are

$$E_m = -\gamma \hbar B_o m, \quad m = I, \ I-1, .., \ -I \tag{3.6}$$

and the general time-dependent solution will be

$$\Psi(t) = \sum_{m=-I}^{+I} c_m \psi_{I,m} \exp\left(-\frac{i}{\hbar} E_m t\right) \tag{3.7}$$

where $\psi_{I,m}$ are the corresponding eigenfuctions of the time-independent Schrödinger equation.

To detect the presence of such a set of energy levels, it is necessary to have an interaction that can cause a transition between the levels. To satisfy the conservation of energy, the

34

interaction must be time dependent and of such an angular frequency that

$$\hbar\omega = \Delta E \qquad (3.8)$$

where ΔE is the energy difference between the initial and final Zeeman energies. Also, the interaction must have a non-vanishing matrix element joining the initial and final states. An alternating magnetic field applied perpendicular to the static field provides such a coupling. The operator I_x has matrix elements between states m and m', $\langle m' | I_x | m \rangle$, which vanish unless $m' = m \pm 1$. Consequently, the allowed transitions are between adjacent energy levels:

$$\hbar\omega = \Delta E = \gamma\hbar B_o$$

or

$$\omega = \gamma B_o \qquad (3.9)$$

An important thing to note here is that Planck's constant $\hbar$ disappears from the resonant equation, which suggests that the result is closely related to a classical picture.

3.3.2 Expectation Value and its Equation of Motion

We can compute the expectation value of any observable, for example μ_x , by means of the time-dependent wave function $\Psi(t)$:

$$\langle \mu_x(t) \rangle = \langle \Psi(t) | \mu_x | \Psi(t) \rangle \qquad (3.10)$$

or if we take into account that $\mu_x = \gamma\hbar I_x$,

$$\langle \mu_x(t) \rangle = \sum_{m,m'} \gamma\hbar c_m^* c_m \langle m' | I_x | m \rangle \exp\left[-\frac{i}{\hbar}(E_{m'} - E_m)t\right], \qquad (3.11)$$

35

where $\langle m' | I_x | m \rangle \equiv \langle \psi_{I,m'} | I_x | \psi_{I,m} \rangle$ is a time-independent matrix element. Since these matrix elements vanish unless $m' = m \pm 1$, all the terms of Eqn. (3.11) have an angular frequency of either $+\gamma B_o$ or $-\gamma B_o$, so their sum must also contain γB_o.

We are interested in spin 1/2 systems only. For that case, taking into account the fact that diagonal elements of I_x vanish, the expectation value of μ_x will be

$$\langle \mu_x (t) \rangle = \gamma \hbar \left[c^*_{1/2} c_{-1/2} \left\langle \frac{1}{2} \left| I_x \right| -\frac{1}{2} \right\rangle \exp\left(-i\gamma B_o t\right) + c^*_{-1/2} c_{1/2} \left\langle -\frac{1}{2} \left| I_x \right| \frac{1}{2} \right\rangle \exp\left(i\gamma B_o t\right) \right]$$

(3.12)

Since $\left\langle \frac{1}{2} \left| I_x \right| -\frac{1}{2} \right\rangle = \left\langle -\frac{1}{2} \left| I_x \right| \frac{1}{2} \right\rangle^*$ we have

$$\langle \mu_x (t) \rangle = 2\gamma \hbar \operatorname{Re} \left\{ \left[c^*_{1/2} c_{-1/2} \left\langle \frac{1}{2} \left| I_x \right| -\frac{1}{2} \right\rangle \exp\left(-i\omega_o t\right) \right] \right\}$$

(3.13)

where $\omega_o = \gamma B_o$ is the angular frequency we must apply to produce resonance. Using raising and lowering operators we can show that $\left\langle \frac{1}{2} \left| I_x \right| -\frac{1}{2} \right\rangle = \frac{1}{2}$. Also, if we express c's in terms of two real positive quantities a and b, and two real but not necessary positive quantities α and β, i.e. $c_{1/2} = a \exp(i\alpha)$ and $c_{-1/2} = b \exp(i\beta)$, the normalization of the wave function will give $a^2 + b^2 = 1$. Then we have

$$\langle \mu_x (t) \rangle = \gamma \hbar a b \cos\left(\alpha - \beta + \omega_o t\right)$$

(3.14)

Similarly, for $\langle \mu_y (t) \rangle$ and $\langle \mu_z (t) \rangle$ we get

$$\langle \mu_y (t) \rangle = -\gamma \hbar a b \sin\left(\alpha - \beta + \omega_o t\right)$$

(3.15)

$$\langle \mu_z (t) \rangle = \gamma \hbar \frac{a^2 - b^2}{2}$$

(3.16)

Note that both, $\langle \mu_x \rangle$ and $\langle \mu_y \rangle$, oscillate in time at the Larmor frequency γB_o, but $\langle \mu_z \rangle$ is time-independent. Moreover, the maximum amplitudes of $\langle \mu_x \rangle$ and $\langle \mu_y \rangle$ are the same.

36

We can rewrite $\langle \vec{\mu} \rangle$ in a vector form

$$\langle \vec{\mu} \rangle = \begin{pmatrix} \langle \mu_x \rangle \\ \langle \mu_y \rangle \\ \langle \mu_z \rangle \end{pmatrix} \tag{3.17}$$

and take into account that $\langle \mu_x \rangle^2 + \langle \mu_y \rangle^2 = const.$ Then we see that $\langle \vec{\mu} \rangle$ behaves like a vector oriented at a fixed angle with respect to z-axis, and precessing in the transverse plane. We will see later, that exactly the same behavior is predicted for the vector of the nuclear magnetic moment when treated classically.

On the other hand let us define x-, y-, z-axes as fixed, with the z-axis coinciding with the direction of magnetic field, which could vary with time as well. Then, as mentioned before, the Hamiltonian is $H = -\gamma \hbar B I_z$. Then we can use the commutation relation of the components of the angular momentum

$$[I_i, \ I_j] = i\varepsilon_{ijk}I_k$$

to find

$$\frac{dI_x}{dt} = \frac{i}{\hbar}\,[H, \ I_x] = -\gamma B_o i\,[I_z, \ I_x] = \gamma B_o I_y \tag{3.18}$$

In the same manner,

$$\frac{dI_y}{dt} = -\gamma B_o I_x \tag{3.19}$$

and

$$\frac{dI_z}{dt} = 0 \tag{3.20}$$

37

If we write $\frac{d\vec{I}}{dt}$ as a column vector

$$\frac{d\vec{I}}{dt} = \begin{pmatrix} \frac{dI_x}{dt} \\ \frac{dI_y}{dt} \\ \frac{dI_z}{dt} \end{pmatrix} \tag{3.21}$$

then the three equations above, (3.18), (3.19) and (3.20), are the components of the vector operator equation:

$$\frac{d\vec{I}}{dt} = \vec{I} \times \gamma\vec{B} \tag{3.22}$$

Recalling that $\vec{\mu} = \gamma\hbar\vec{I}$, we have an equation for the expectation value of $\vec{\mu}$:

$$\frac{d\langle\vec{\mu}\rangle}{dt} = \langle\vec{\mu}\rangle \times \gamma\vec{B} \tag{3.23}$$

Eqn. (3.23) has a classical form, meaning that the expectation value of the magnetic moment of a spin obeys the classical equation of motion.

The equation above is for a single spin. In case of a group of spins with magnetic moments μ_i for the ith spin, the expectation value for the total magnetization will be

$$\left\langle \vec{M} \right\rangle = \sum_i \langle\vec{\mu}_i\rangle \tag{3.24}$$

If the spins do not interact with one another, Eqn. (3.23) holds for the total magnetization as well. It is very important to remember that Eqn. (3.23) was derived without limitations on the magnetic field, i.e. it holds not only for the static, but also the time-dependent field. Therefore, we can study the effects of the alternating magnetic field using a classical description of the system.

38

3.4 Classical Picture

3.4.1 Nuclei in an External Magnetic Field

The protons and neutrons that make-up the nuclei possess an intrinsic angular momentum, spin. This phenomenon can be thought of as arising from the magnetic field created by the rotating internal charged structure of the nucleon. The direction of the spin, and the magnetic moment associated with it, will be normal to the plane of rotation (Figure3.3).The
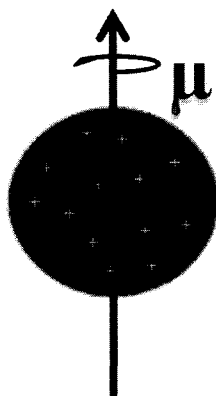
Figure 3.3: Classical description of a spin. A proton with distributed charge creates a magnetic moment while spinning about its axis.

neutron is electrically neutral. However, since the charges within it are not uniformly distributed, the neutron also generates a net magnetic moment. As we know, the relationship between the angular momentum J and the magnetic moment $\vec{\mu}$ of a nucleus is given by

$$\vec{\mu} = \gamma \vec{J} \tag{3.25}$$

where γ is a proportionality constant characteristic of a given nucleus known as the *gyromagnetic ratio*.

39

A nucleus containing an even number of nucleons, in which the individual angular momenta of the constituents cancel out, will have a zero net angular momentum. An odd number of protons and neutrons on the other hand will create a configuration, in which the net angular momentum of the nucleus, and hence its magnetic moment is non-zero. Such nuclei are used in NMR experiments.
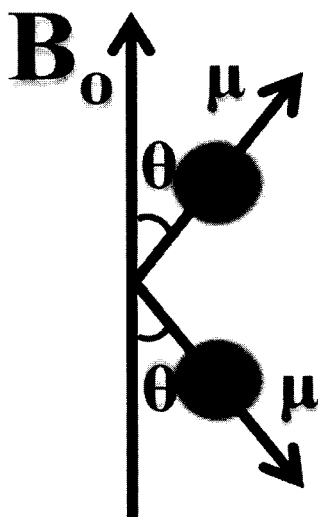
Figure 3.4: Interaction of a nucleus with an applied magnetic field. It aligns itself either parallel or anti-parallel to the field.

In a static uniform external field, $\vec{B}_0 = \hat{k}B_0$, the proton will be oriented parallel or antiparallel to $\hat{k}$ (Figure 3.4). The difference in the energy between two states is

$$\Delta E = \mu_z B_0 - (-\mu_z B_0) = 2\mu_z B_o. \qquad (3.26)$$

Therefore, if the proton flips, it will either emit or absorb a photon of frequency ω, which is found from the Bohr relation

$$\Delta E = \hbar\omega. \qquad (3.27)$$

40

From Eqns.3.26 and 3.27, it follows that

$$\omega = \left[\frac{2\mu_z}{\hbar}\right] B_o = \gamma B_o \qquad (3.28)$$

In order to see the evolution of the magnetic moment under the influence of the magnetic field, $\vec{B_o}$, let's assume that at $t = 0$

$$\vec{\mu}(0) = \hat{i}\mu_{x0} + \hat{j}\mu_{y0} + \hat{k}\mu_{z0} \qquad (3.29)$$

The magnetic moment will be subjected to a torque given by

$$\vec{N} = \vec{\mu} \times \vec{B_o} = \frac{d\vec{J}}{dt} \qquad (3.30)$$

From Eqns. (3.25) and (3.30) we get

$$\frac{d\vec{\mu}}{dt} = \gamma(\vec{\mu} \times \vec{B_o}) \qquad (3.31)$$

or for each component separately

$$\begin{aligned}
\frac{d\mu_x}{dt} &= \gamma\mu_y B_o \\
\frac{d\mu_y}{dt} &= -\gamma\mu_z B_o \\
\frac{d\mu_z}{dt} &= 0
\end{aligned} \qquad (3.32)$$

Combining the 1st two equations of (3.32) gives, for the transverse components,

$$\frac{d^2}{dt^2}\begin{pmatrix} \mu_x \\ \mu_y \end{pmatrix} + (\gamma B_o)^2 \begin{pmatrix} \mu_x \\ \mu_y \end{pmatrix} = 0. \qquad (3.33)$$

Solving these equations with the initial conditions (3.29) in mind, gives

$$\vec{\mu}(t) = \hat{i}\left(\mu_{x0}\cos\omega t + \mu_{y0}\sin\omega t\right) + \hat{j}\left(\mu_{y0}\cos\omega t - \mu_{x0}\sin\omega t\right) + \hat{k}\mu_{z0} \qquad (3.34)$$

41

where $\omega = \gamma B_0$. In matrix form this can be written as

$$\vec{\mu}(t) = R_z\left(\omega t\right) \vec{\mu}_0, \tag{3.35}$$

where vectors are represented as column matrices

$$\vec{\mu}(t) = \begin{pmatrix} \mu_x(t) \\ \mu_y(t) \\ \mu_z(t) \end{pmatrix}, \tag{3.36}$$

and $R_z\left(\omega t\right)$ is a matrix representation of a rotation about $z-$axis:

$$R_z\left(\alpha\right) = \begin{pmatrix} \cos\alpha & \sin\alpha & 0 \\ -\sin\alpha & \cos\alpha & 0 \\ 0 & 0 & 1 \end{pmatrix} \tag{3.37}$$

This solution represents the precession of the magnetic moment about the axis of the
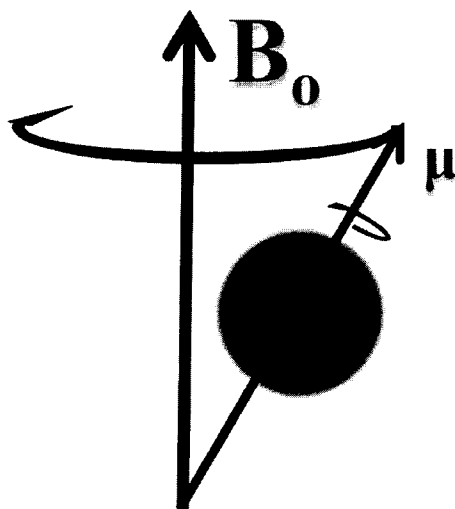
Figure 3.5: Precession of a spin with magnetic moment $\vec{\mu}$ in the presence of a magnetic field.

42

applied field , $\hat{k}$ (Figure 3.5) with frequency

$$\omega = \gamma B_0 \qquad (3.38)$$

called Larmor frequency.

3.4.2 Thermal Magnetization

When a magnetic field, B_0 is applied across a macroscopic sample, containing a large number of nuclei, each possessing a magnetic moment (Figure 3.6), the spins orient themselves in such a way, that the $\hat{k}$ components of the nuclear spins add up to create a net magnetic moment, $\vec{M}$. The transverse components of the spins however are incoherent, therefore unable to amount to a non-zero total.In terms of the energy states discussed above, a slight
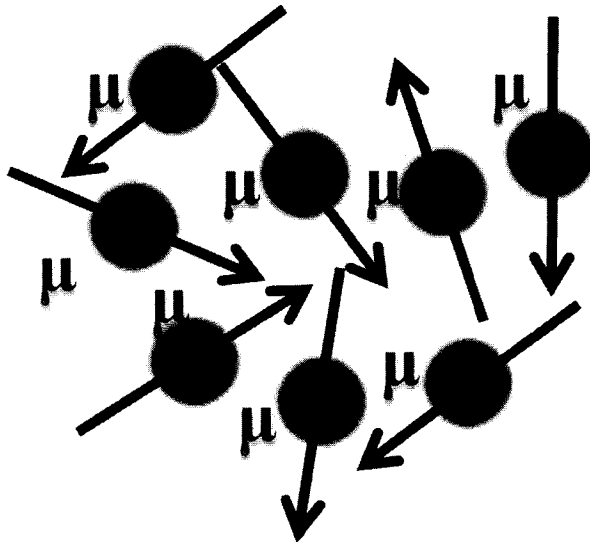
Figure 3.6: Thermal equilibrium in a non-magnetic material. In the absence of an external magnetic field non-magnetic materials have zero net magnetic moment.

majority of the spins will end up in the antiparallel direction, while the rest are parallel.

43

Let N_α be the probability that a given nucleus will be found in α-state at the lower energy, while N_β be the probability that it will be in β-state, at the higher energy. If the system is in thermal equilibrium, then the probabilities are governed by Boltzmann's Law [10]

$$\frac{N_\alpha}{N_\beta} = \exp\left(\frac{\Delta E}{k_B T}\right) \approx 1 + \frac{\Delta E}{k_B T} \tag{3.39}$$

where k_B is Boltzmann's constant ($k_B = 1.3806 \times 10^{-23} J \cdot K^{-1}$), T is the absolute temperature of the sample, and ΔE is the energy difference between the two states. For protons at $20^\circ C$, ΔE is on the order of $10^{-26} J$ and $k_B T$ is on the order of $10^{-21} J$. Since the populations of the two levels are close, one can write

$$N_\alpha - N_\beta \approx \frac{\Delta E}{2 k_B T} \tag{3.40}$$

By definition the polarization is

$$P = \frac{N_\alpha - N_\beta}{N_\alpha + N_\beta} = \frac{\Delta E}{2 k_B T} \tag{3.41}$$

since $N_\alpha + N_\beta = 1$. Therefore

$$\vec{M} = (N_\alpha - N_\beta) n\mu_z \hat{k} \approx \frac{\Delta E}{2 k_B T} n\mu_z \hat{k} \tag{3.42}$$

where n is the number of nuclei per unit volume. As evident from this equation, the net magnetization will decrease with the temperature.

3.4.3 RF Pulses and Rotating Reference Frame

Assuming the individual nuclear spins do not interact, we can extend the formalism developed for the corresponding magnetic moments, to the bulk magnetization $\vec{M}$. At $t = 0$,

$$\vec{M}(0) = \hat{\imath} M_{x0} + \hat{k} M_{z0}. \tag{3.43}$$

44

And the three components change as

$$\frac{dM_x}{dt} = \gamma M_y B_o \tag{3.44}$$

$$\frac{dM_y}{dt} = -\gamma M_z B_o \tag{3.45}$$

$$\frac{dM_z}{dt} = 0 \tag{3.46}$$

with (3.43) as the initial conditions. The solution to this equations is

$$\vec{M}(t) = \begin{pmatrix} \cos\omega t & \sin\omega t & 0 \\ -\sin\omega t & \cos\omega t & 0 \\ 0 & 0 & 1 \end{pmatrix} \begin{pmatrix} M_x \\ M_y \\ M_z \end{pmatrix} = \begin{pmatrix} M_{xo}\cos\omega t \\ -M_{xo}\sin\omega t \\ M_{zo} \end{pmatrix} \tag{3.47}$$

Again the equations describe a precession about the applied field (Figure 3.7, a). Consider now a frame of reference, which rotates about $\hat{k}$ with the same frequency as $\vec{M}$, ω. In this frame the magnetization is stationary. To show that M_x and M_y are also stationary, we can to use

$$\begin{pmatrix} \hat{i}' \\ \hat{j}' \\ \hat{k}' \end{pmatrix} = - \begin{pmatrix} \cos\omega_r t & \sin\omega_r t & 0 \\ -\sin\omega_r t & \cos\omega_r t & 0 \\ 0 & 0 & 1 \end{pmatrix} \begin{pmatrix} \hat{i} \\ \hat{j} \\ \hat{k} \end{pmatrix} \tag{3.48}$$

If we let $\omega_r = \gamma B_o$, the magnetization in the rotating frame will be (fig 3.7)

$$\vec{M} = \hat{i}' M_{xo} + \hat{k}' M_{xo} = const \tag{3.49}$$

In order to produce transverse magnetization that generates the NMR signal, a component of the RF magnetic field must be in the transverse plane. Suppose that the RF

45
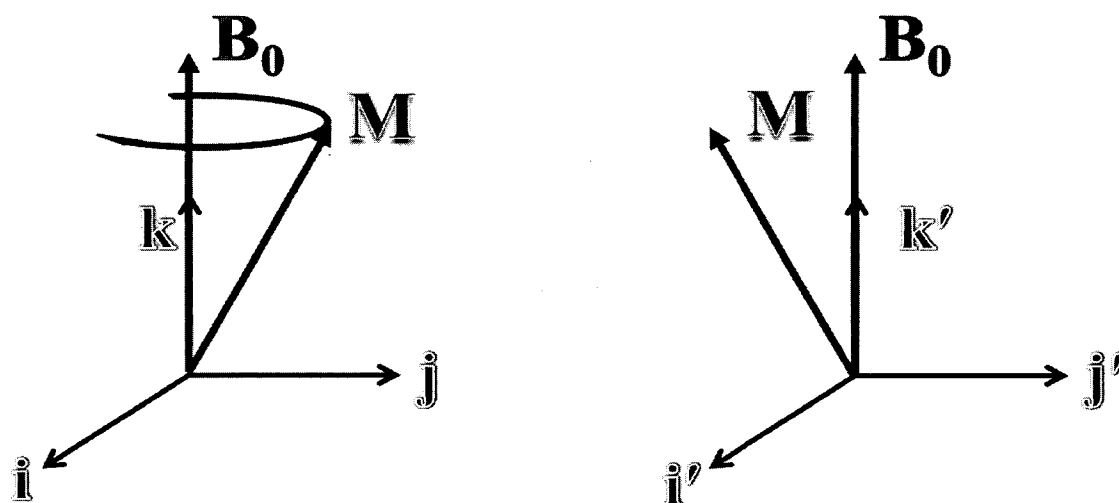
Figure 3.7: Laboratory and rotating reference frames. In the stationary reference frame, the net magnetization precesses about $\vec{B}_o$, while in the rotating reference frame net magnetization vector $\vec{M}$ is stationary.

magnetic field $\vec{B}_1(t)$ is initially applied along the x-axis and has a frequency of ω_{rf}. In the laboratory frame, a circularly polarized, or quadrature, B_1 field can be written as

$$\vec{B}_1^{lab}(t) = \hat{\imath}\, B_1(t)\cos(\omega_{rf}t) - \hat{\jmath}\, B_1(t)\sin(\omega_{rf}t) \tag{3.50}$$

We can write it in the rotating (with angular frequency equal to ω_{rf}) reference frame as

$$\vec{B}_1^{rot}(t) = -\begin{pmatrix} \cos\omega t & \sin\omega t & 0 \\ -\sin\omega t & \cos\omega t & 0 \\ 0 & 0 & 1 \end{pmatrix}\begin{pmatrix} B_{1,x}^{lab} \\ B_{1,y}^{lab} \\ B_{1,z}^{lab} \end{pmatrix} = \begin{pmatrix} B_1(t) \\ 0 \\ 0 \end{pmatrix} \tag{3.51}$$

Now, let's rewrite the equations of motion in the rotating coordinate system for the case when not only the main magnetic field is present, but the RF field is applied as well. In general for a magnetization vector in an external magnetic field $\vec{B}$ we have

$$\frac{d\vec{M}}{dt} = \gamma \vec{M} \times \vec{B} \tag{3.52}$$

46

Since

$$\frac{d\vec{M}}{dt} = \frac{d}{dt}\sum_{ijk} \hat{i}'M_{i'} + \hat{j}'M_{j'} + \hat{k}'M_{k'} = M_{i'}\frac{\partial\hat{i}'}{\partial t} + M_{j'}\frac{\partial\hat{j}'}{\partial t} + M_{k'}\frac{\partial\hat{k}'}{\partial t} + \hat{i}'\frac{\partial M_{i'}}{\partial t} + \hat{j}'\frac{\partial M_{j'}}{\partial t} + \hat{k}'\frac{\partial M_{k'}}{\partial t}$$

and

$$\frac{d}{dt}\begin{pmatrix} \hat{i}' \\ \hat{j}' \end{pmatrix} = \vec{\Omega} \times \begin{pmatrix} \hat{i}' \\ \hat{j}' \end{pmatrix} \tag{3.53}$$

where $\Omega = -\omega_r \hat{k}$ with ω_r being frequency of the rotating frame, we can write for the magnetization vector:

$$\frac{d\vec{M}}{dt} = \vec{\Omega} \times \vec{M} + \frac{\delta\vec{M}}{\delta t} \tag{3.54}$$

where $\delta\vec{M}/\delta t$ is the derivative of the magnetization vector in the rotating frame. Then in this frame by combining eqns. (3.52) and (3.54), we get

$$\frac{\delta\vec{M}}{\delta t} = \frac{d\vec{M}}{dt} - \vec{\Omega} \times \vec{M} = \gamma\vec{M} \times \vec{B}_{eff} \tag{3.55}$$

where the effective field

$$\frac{d\vec{M}}{dt} = \gamma\vec{M} \times \left\{ \hat{k}\left(B_o - \frac{\omega_r}{\gamma}\right) + B_1(t)\left[\hat{i}\cos\left(\omega_{rf} - \omega_r\right)t - \hat{j}\sin\left(\omega_{rf} - \omega_r\right)t\right] \right\} \tag{3.56}$$

If we set the rotating frame frequency to be equal to RF frequency, i.e. $\omega_{rf} = \omega_r$, than we 'll have

$$\vec{B}_{eff} = \hat{k}\left(B_o - \frac{\omega_r}{\gamma}\right) + \hat{i}'B_1 \tag{3.57}$$

Then if $\omega_r = \gamma B_o$,

$$B_{eff} = \hat{i}'B_1. \tag{3.58}$$

The $\vec{B}_1$ field applied on-resonance for a finite time is called an Radio-Frequency (RF) pulse. RF pulses are characterized by their flip (or tip) angle α, which is the angle between

47
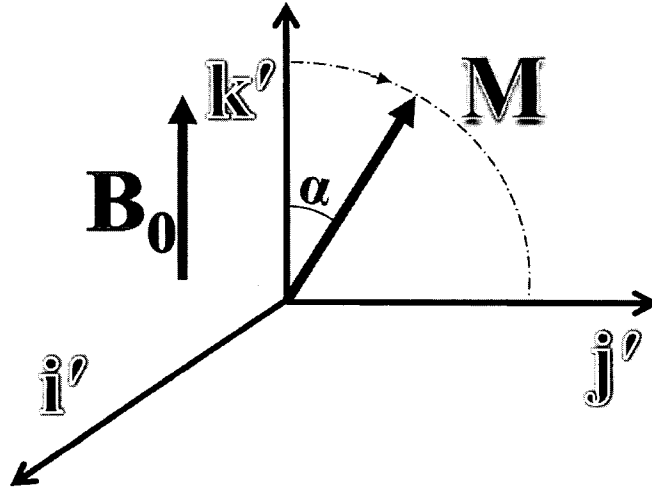
Figure 3.8: RF pulse application in the rotating reference frame.

the direction of the main magnetic field and the magnetization vector immediately after

the RF pulse is terminated (Figure 3.8).

To quantify the flip angle let us consider the equation describing the dynamics of the

magnetization vector as seen from the rotating reference frame rotating at $\omega_r = \omega_{rf}$:

$$\frac{d\vec{M}}{dt} = \gamma\vec{M} \times \vec{B}_{eff} = \gamma\vec{M} \times \left[\hat{k}\left(B_o - \frac{\omega_{rf}}{\gamma}\right) + \hat{i}'B_1\right] \tag{3.59}$$

This equation can be written in vector matrix form as

$$\frac{d\vec{M}}{dt} = \begin{bmatrix} 0 & \Delta\omega & 0 \\ -\Delta\omega & 0 & \gamma B_1 \\ 0 & -\gamma B_1 & 0 \end{bmatrix} \vec{M}(t) = \Re\vec{M}(t) \tag{3.60}$$

where $\Delta\omega = \gamma B_0 - \omega_{rf}$. The solution to this equation is

$$\vec{M}(t) = \exp(\Re t)\,\vec{M}_0 \tag{3.61}$$

with $\vec{M}_0 = \vec{M}(t = 0)$ and

$$\exp(\Re t) = I + \Re t + \frac{1}{2}(\Re t)^2 + \frac{1}{3!}(\Re t)^3 + \dots \tag{3.62}$$

48

with I being a unity matrix. If we choose ω_r such that $\Delta\omega = 0$, set initial conditions such that at time $t = 0$ the magnetization vector is along the magnetic field ($M_{x,0} = 0$, $M_{y,0} = 0$, and $M_{z,0} = M_0$) then the Eqn.3.60 will have a solution of a form:

$$\vec{M}(t) = \begin{bmatrix} 0 \\ M_0 \sin\left(\gamma \int_0^t B_1(t')\,dt'\right) \\ M_0 \cos\left(\gamma \int_0^t B_1(t')\,dt'\right) \end{bmatrix}, \tag{3.63}$$

i.e. in the rotating frame magnetization precesses in $yz - plane$ with an angle

$$\alpha(t) = \gamma \int_0^t B_{eff}(t')\,dt' \tag{3.64}$$

called flip angle. It should be stressed again that this was obtained for a case of on-resonance excitation $\omega_{rf} = \gamma B_0 : \quad \Delta\omega = \gamma B_0 - \omega_{rf} = 0$. However, strictly speaking, this assumption is valid only at the center of the RF pulse. For more general case, when $\Delta\omega \neq 0$ let consider a complex vector of transverse magnetization defined as

$$M_\perp = M_x + iM_y \tag{3.65}$$

Then the first two equations of 3.60 can be written as

$$\frac{dM_\perp}{dt} = -i\Delta\omega M_\perp + i\gamma B_1(t)M_z(t) \tag{3.66}$$

Now, if we choose the same initial conditions as above ($M_{\perp,0} = 0$) the solution to this equation will be

$$M_\perp(t) = i\gamma \exp(-i\Delta\omega t) \int_0^t B_1(t')M_z(t')\exp(i\Delta\omega t')\,dt'. \tag{3.67}$$

49

For small flip angles $M_z(t) \approx M_0$ and the above equation can be written as

$$M_\perp(t) \approx i\gamma M_0 \exp(-i\Delta\omega t) \int_0^t B_1(t') \exp(i\Delta\omega t') \, dt' \qquad (3.68)$$

Then the flip angle will be

$$\sin(\alpha) = \frac{|M_\perp(t)|}{M_0} = \gamma \left| \int_0^t B_1(t') \exp(i\Delta\omega t') \, dt' \right| \qquad (3.69)$$

Since for small angles $M_z(t) \approx M_0$ then α must be small and

$$\sin(\alpha) \approx \alpha \approx \gamma \left| \int_0^t B_1(t') \exp(i\Delta\omega t') \, dt' \right| \qquad (3.70)$$

According to equations 3.64 and 3.70, the flip angle is linearly proportional to the RF field under one of the following two conditions: (a) for on-resonance excitations, or (b) for small flip angles ($\alpha \ll 1 \, rad$).

3.5   Bloch Equations and Relaxation

3.5.1   Bloch Equations in Rotating Frame

The motion equations derived for the magnetization vector in the previous subsection state that a 90° RF pulse tips the the magnetization vector, resulting in a non-zero transverse component, which will then proceed to rotate perpetually. Experimental observations however show, that the signal, and therefore M_{xy}, picked up by a coil normal to the transverse plain, starts decaying exponentially with time, immediately after the RF pulse is turned off. This behavior was explained by Bloch [25] who included the main relaxation mechanisms into the phenomenology, and quantified them with characteristic constants T_1 and T_2, called respectively the "longitudinal" and the "transverse" relaxation times.

50

For a sample of nuclei placed in an external uniform field and tipped by a 90° flip angle the Bloch equations can be written as

$$\frac{dM_{x,y}}{dt} = \gamma \left(\vec{M} \times \vec{B} \right)_{x,y} - \frac{M_{x,y}}{T_2} \tag{3.71}$$

$$\frac{dM_z}{dt} = \gamma \left(\vec{M} \times \vec{B} \right)_z + \frac{M_o - M_z}{T_1} \tag{3.72}$$

where M_o is the equilibrium value of the magnetization vector. Let $\pi/2$ RF pulse be applied in the transverse plane, so that initially there is no magnetization along $\hat{k}$ or $\hat{j}$.

$$\vec{M}(0) = \hat{i} M_o \tag{3.73}$$

The the solutions to these equations are

$$\begin{aligned}
M_x(t) &= M_o \exp\left(\frac{-t}{T_2}\right) \cos\left(\gamma B_o t\right) \\
M_y(t) &= -M_o \exp\left(\frac{-t}{T_2}\right) \sin\left(\gamma B_o t\right) \\
M_z(t) &= M_o \left[1 - \exp\left(\frac{-t}{T_1}\right) \right]
\end{aligned} \tag{3.74}$$

The physical causes of relaxation are related to the mutual influence of magnetic moments and their interaction with the environment. The effect of the relaxation process is the return of the magnetization vector to its equilibrium state.

3.5.2 The Relaxation

To understand the relaxation let us consider a sample under no magnetic field influence. In such a case the magnetic moments of the nuclei are randomly oriented, resulting in zero net magnetization. When B_o is applied all nuclei start precessing about its axis at Larmor frequency with a precessional angle θ_o. However some orient themselves parallel, while others - anti-parallel to the field axis. It is important to note that the phases of the nuclei

51

is random, resulting in no transverse component of the magnetization even though each nucleus has a non-zero transverse component itself.

Upon application of an RF pulse, a phase coherence is established in both states. Since the RF pulse is on resonance it allows energy to be imparted onto the system. As a result, nuclei, in a net sense, migrate to the anti-parallel state. Once the population of the nuclei in each cone is the same, there is no net axial magnetization and a 90° flip is reached.

After a 90° pulse, as the magnetization precesses in the transverse plane, two types of relaxation occur. Longitudinal, or spin-lattice relaxation brings the axial component of the magnetization back to its equilibrium value and is quantified by T_1. The other type of relaxation is transverse or spin-spin relaxation, which reduces the transverse magnetization to zero and is quantified by T_2.

Longitudinal Relaxation As mentioned above, in longitudinal relaxation nuclei, under the applied magnetic field, gradually migrate back to the parallel state to re-establish their equilibrium population distribution. When a nucleus flips back to the parallel state, it experiences a change in energy. This energy difference is characterized by the Larmor frequency. Radiation at Larmor frequency will stimulate this emission and bring the nuclei back to equilibrium quicker. However there is an important distinction between the kind of transitions caused by RF pulses and those leading to relaxation. In the case of the RF pulses, all spins experience the same oscillating field, whereas in the other case the transverse fields are local, thereby affecting only a few spins and not the whole sample. Moreover, these fields are random in amplitude and direction, and it is exactly this randomness which drives the sample to equilibrium.

The return to equilibrium is called the spin-lattice relaxation since the lattice is responsible for stimulating and absorbing this release of energy.

The lattice may provide radiation at the resonance frequency through random thermal motions of nuclei. In liquids the molecules have more freedom to rotate, translate and collide with one another than in solids. Therefore the chance that stimulated emissions will occur is, in general, greater and consequently, T_1 is shorter for liquids than for solids; and it is even shorter for gases.

Transverse Relaxation As mentioned, M_{xy} is formed when a large number of nuclear spins precess in phase, so that their transverse components are parallel. The rate of precession of each of these moments is dictated by the strength of the magnetic field in the vicinity of the given nucleus. If initially all such magnetic moments are in phase, inhomogeneities will cause them to rotate at slightly different frequencies, so that after some time phases will no longer be equal. This will result in a diminished M_{xy}, eventually bringing its value to 0, once the nuclear phases are completely uncorrelated.

There are two ways to destroy the coherence in the transverse magnetization. The first is to make the vectors jump to new positions at random. which can be brought about by local oscillating fields, just like in the case of the longitudinal relaxation, where the oscillating fields force the spins to flip. In general, anything that causes spin-lattice relaxation will cause spin-spin relaxation as well. The second way to dephase the magnetization is to get the vectors to precess at slightly different frequencies. Again, a local field plays a part in it, but this time it does not need to be oscillating, it just needs to be different at different points.

53

Relaxation Mechanisms *Paramagnetic Impurities* The large magnetic moment of the electron means that paramagnetic impurities are particularly effective in promoting relaxation. Such species include paramagnetic oxygen and certain transition metal compounds.

Dipol-Dipol Interaction Two spins can interact with their magnetic moments, while one of them creates a magnetic field and the other one experiences it. Their roles are interchangeable. The size of this interaction depends on the distance between two nuclei and the angle between the line connecting them and the direction of the field. When the nuclei move around, the distance between them, as well as the direction of the vector, change forcing changes in the magnetic field. However these molecular vibrations do not have a component at Larmor frequency. They generally cause changes in the orientation, that promote relaxation.

Chemical Shift Anisotropy Due to the effect of the electrons present in a molecule, the magnetic field experienced by a nucleus is slightly different (in both, direction and strength) from the field applied externally, thereby causing a chemical shift. In fact, the magnetic field experienced by the nucleus depends on the orientation of the molecule relative to the applied field. This is called chemical shift anisotropy. The changes in the field at the nucleus are small, but sufficient to be detected in the spectrum and cause relaxation.

3.6   The NMR signal - FID

The goal in MRI is to image the spatial distribution of the transverse magnetization in a given object, once the magnetization vector has been tipped by an RF pulse. In the earlier discussion we showed how to create this magnetization, here we will talk about how to interpret the signal we collect.

Consider a $\pi/2$ pulse applied uniformly over a sample of spins. The pulse rotates the longitudinal magnetization into the transverse plane. Once the magnetization vector has a transverse component, measurement of the precession is possible. According to Faraday's law, an *emf* is created in any coil through which the spin's magnetic flux sweeps. This can be expressed as

$$emf = -\frac{d\Phi(t)}{dt} = \frac{d}{dt}\int_{sample} dV \left[\vec{B}_{receive}(\vec{r}) \cdot \vec{M}(\vec{r}, t)\right] \qquad (3.75)$$

where $\vec{B}_{recieve}$ is the field of the current created by the precessing vector. If there were
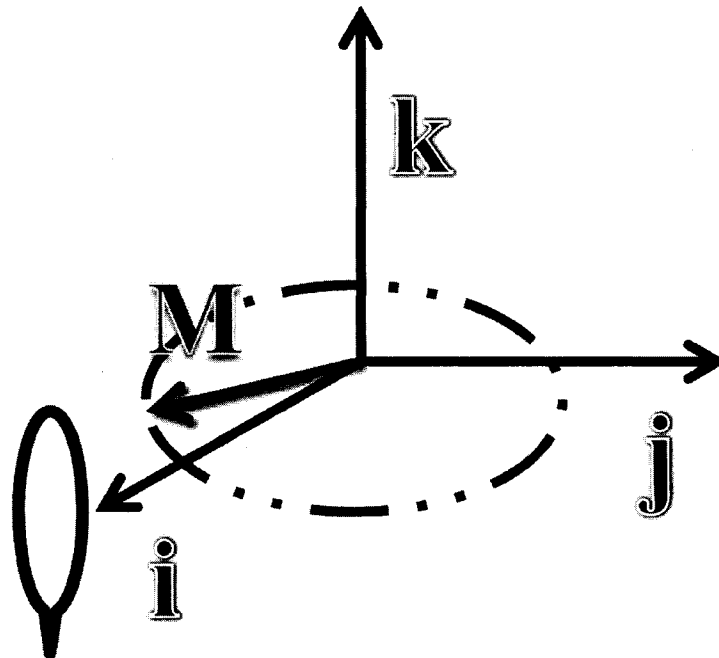
Figure 3.9: Derecting the signal in NMR

no relaxation mechanisms, the collected signal would have a sinusoidal form (Figure 3.10, a), but with the relaxation the sinusoidal is modulated by an "exponential" envelope (see Figure 3.10, b)Mathematically the signal can be written as

55

$M_{xy}=M_{xy,o}*exp(-t/T_2)$
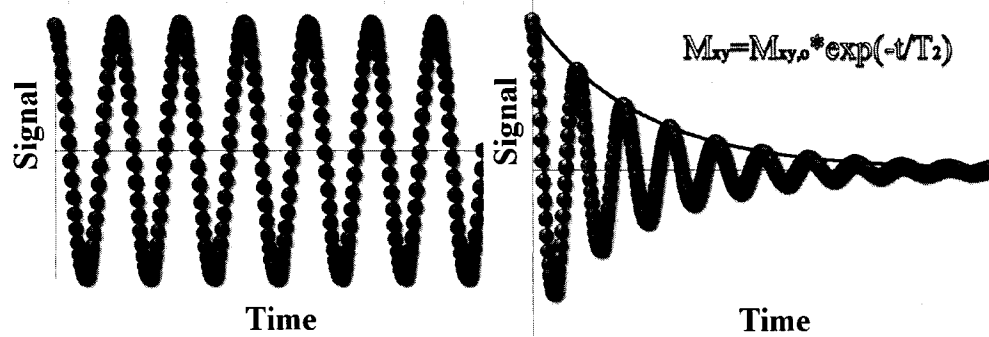
Figure 3.10: The signal with and without relaxation effects. In the absence of relaxation the transverse magnetization would perpetually rotate in the XY-plane. However, in the reality various relaxation mechanisms cause a nearly exponential decay of the sinusoidal signal.

$$s(t) = M_\perp \exp(-t/T_2) \exp(i\omega_o t + \phi) \tag{3.76}$$

This kind of an experiment is called Free Induction Decay, FID. It is used routinely to measure flip angles, or relaxation times T_1 and T_2. We will discuss these experiments in more detail in later chapters. Fourier Transformation of this signal will transfer it from the time domain to the frequency domain giving a peak at the frequency at which the nuclei in the sample were precessing.

3.7 k-space and Fourier Analysis.

3.7.1 Field Gradients

Consider a sample that consists of 2 cylinders filled with water (Figure 3.11, a).Although they are separated in space, if the protons experience the same general field, then the FT of the signal (Figure 3.11, b) will have only one peak in the frequency spectrum (Figure

56
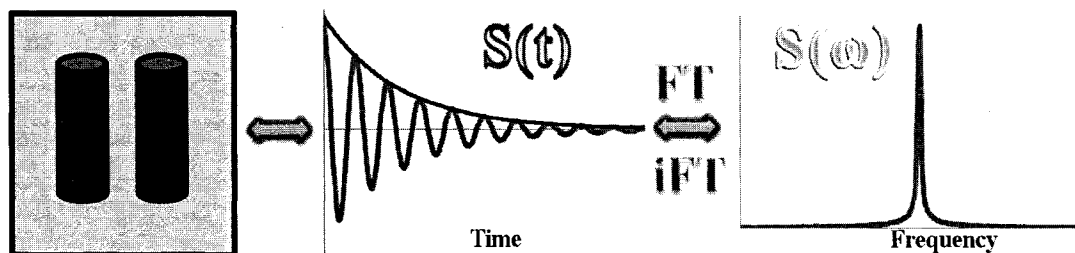
Figure 3.11: FID signal of a phantom

3.11, c). If each of the cylinders were to see a unique magnetic field, we would be able to differentiate their positions based on the collected signal, hence gain information about the distribution of the matter in the sample. This can be achieved by imposing a spatially linearly varying field gradient on the main magnetic field. It is important to keep in mind that gradient fields vary along some spatial direction, but that field lines are aligned with the main magnetic field, as shown in Figure 3.12. Now, let's see what effect this gradients will have on the signal. Consider a spatially and temporally varying fields introduced by time-varying gradient fields:

$$B\left(\vec{r}, t\right) = B\left(x, y, t\right) + G_x\left(t\right) \cdot x + G_y\left(t\right) \cdot y + G_z\left(t\right) \cdot z \tag{3.77}$$

The instantaneous frequency at each point in space is then given by

$$\gamma B\left(\vec{r}, t\right) = \gamma \left[B_o + G_x\left(t\right) \cdot x + G_y\left(t\right) \cdot y + G_z\left(t\right) \cdot z\right] \tag{3.78}$$

which in the frame rotating at $\omega_o = \gamma B_o$ is seen as

$$\omega\left(\vec{r}, t\right) = \gamma \left[G_x\left(t\right) \cdot x + G_y\left(t\right) \cdot y + G_z\left(t\right) \cdot z\right] \tag{3.79}$$

and the spatially variant phase is

$$\phi\left(\vec{r}, t\right) = \int_0^t \gamma \left[G_x\left(t'\right) \cdot x + G_y\left(t'\right) \cdot y + G_z\left(t'\right) \cdot z\right] dt' \tag{3.80}$$

57
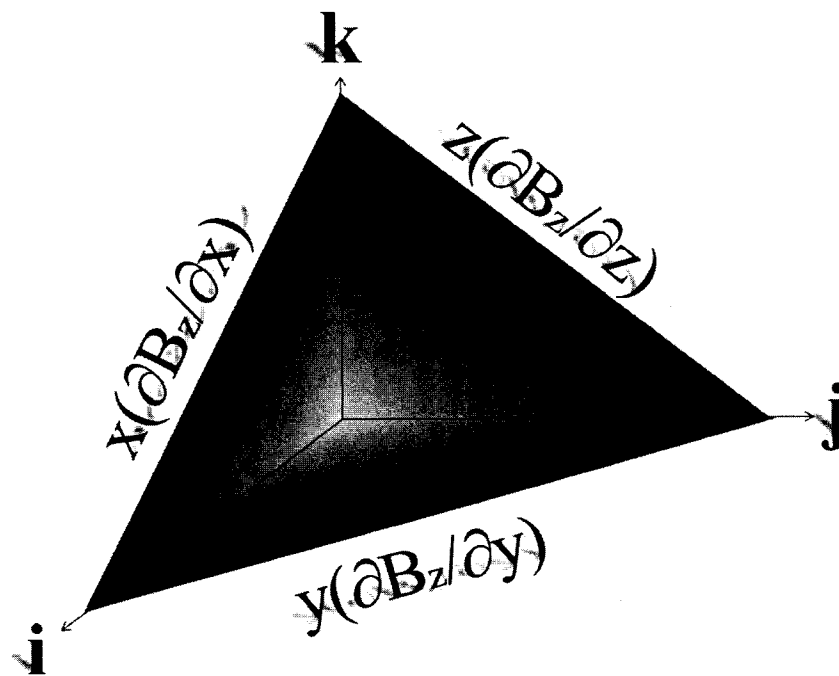
Figure 3.12: Gradient fileds superimposed on the main magnetic field. The color gradient in each plane represents the field gradient in the corresponding direction

58

where time t begins with each RF pulse when it brings the magnetization from the longitudinal axis into the transverse plane, where it is observable. Then the collected signal can be written in the form

$$
\begin{aligned}
s\left(t\right) &= \int \varrho\left(\vec{r},t\right) d\vec{r} \\
&= \int d\vec{r}\left[\rho\left(\vec{r}\right)\exp\left(-t/T_2\right)\exp\left(-i\phi\left(\vec{r},t\right)\right)\right] \\
&= \int d\vec{r}\left\{\varrho\left(\vec{r}\right)\exp\left(-t/T_2\right)\exp\left[-i\gamma\int_0^t\left[G_x\left(t'\right)\cdot x+G_y\left(t'\right)\cdot y+G_z\left(t'\right)\cdot z\right]dt'\right]\right\}
\end{aligned}
\tag{3.81}
$$

3.7.2 k-space definition

Suppose that a physical quantity $w\left(\vec{r}\right)$ is defined in a region V of space, with V finite and $w\left(\vec{r}\right)$ integrable over V. Then we can define a "complementary" distribution $W(\vec{k})$ by applying an FT such that

$$
W(\vec{k}) = \int_V w\left(\vec{r}\right)\exp\left[2\pi i(\vec{k}\cdot\vec{r})\right]d\vec{r}
\tag{3.82}
$$

where $\vec{k}$ is a three-dimensional complex vector and $d\vec{r}$ is a volume element. Then $W(\vec{k})$ is defined in the linear vector space of three-dimensional complex vectors $\vec{k}$, called the $k-space$, which is covariant to the Euclidean $R-space$. Since the two distributions are closely correlated, knowing $W(\vec{k})$ the function $w\left(\vec{r}\right)$ can be computed

$$
w\left(\vec{r}\right) = \int W(\vec{k})\exp\left[-2\pi i(\vec{k}\cdot\vec{r})\right]d\vec{k}
\tag{3.83}
$$

and the solution is guaranteed to be unique.

In the above formulae (3.82 and 3.83) the 3-dimensional $k-space$ corresponding to a 3-dimensional $R-space$ is defined. However, it is evident that, starting with any Euclidean space of n dimensions ($n = 1, 2, 3, ...$), one can extend the definition to the corresponding n-dimensional $k-space$. The physical dimension of the k-vectors of any $k-space$ is always

59

$[m^{-1}]$ (or strictly speaking, $\left[\frac{cycles}{m}\right]$ originating from the fact that $k - space$ is the space of wave numbers corresponding to the plane waves described by Fourier series) rather than $[m]$ of the $R - space$ position vectors $\vec{r}$. This is why $k - spaces$ are also called reciprocal spaces.

3.7.3   k-space and MRI

Let us go back to the collected signal (Eqn. ??). If we define k-vector's components as

$$\begin{pmatrix} k_x(t) \\ k_y(t) \\ k_z(t) \end{pmatrix} = \frac{\gamma}{2\pi} \int_0^t \begin{pmatrix} G_x(t') \\ G_y(t') \\ G_z(t') \end{pmatrix} dt' \tag{3.84}$$

and substitute them in the signal equation (??), we will have

$$s(t) = \int d\vec{r} \{ \varrho(\vec{r}) \exp(-t/T_2) \exp[-2\pi i (x k_x(t) + y k_y(t) + z k_z(t))] \} \tag{3.85}$$

Comparing eqns. (3.85) and (3.82) one discerns a certain similarity broken only by the presence of the factor describing the magnetization decay in the transverse plane and the fact that the k-vector is time dependent. If we temporarily neglect the decay term and assume that during the experiment it remains approximately equal to its initial value of 1, then

$$s(t) = \int d\vec{r} \left\{ \varrho(\vec{r}) \exp\left[-2\pi i (\vec{k}(t) \cdot \vec{r})\right] \right\} = Q(\vec{k}(t)) \tag{3.86}$$

where, according to (3.82), $Q(\vec{k})$ denotes the $k - space$ transform of $Q(\vec{k})$ along the $k - space$ path $\vec{k}(t)$. Note that following from the definition of the k-vector (Eqn.3.84), the path $\vec{k}(t)$ always starts from 0. From (3.84) one can write

$$u(t) = \frac{d \vec{k}(t)}{dt} = \frac{\gamma}{2\pi} \vec{G}(t) = \frac{\gamma}{2\pi} \left| \vec{G}(t) \right| \hat{g}(t) \tag{3.87}$$

60

where $\hat{g}(t)$ is direction vector of the imposed field gradient. This equation indicates that the evolution rate of $\vec{k}(t)$ (both, its absolute value and its direction) is always proportional to the gradient vector $\vec{G}$, which brings to the following: after the excitation one departs from the origin of the $k - space$ and using the gradients, moves along any desired $k - space$ path; along the way, one builds up a record of the $Q(\vec{k})$ values for the subset of the visited $k - space$ points.

Unlike $\varrho(\vec{r})$, the function $Q(\vec{k})$ is complex. This fits with the actual NMR signals which are detected using two phase detectors with orthogonal RF reference signals. The two channels, often denoted as u and v, provide two time-dependent output signals $u(t)$ and $v(t)$ which behave as Cartesian components of a complex signal $s(t) = u(t) + iv(t)$.

According to Eqn. (3.82), $W(-\vec{k}) = W^*(\vec{k})$, with the star denoting a complex conjugate. This means that there is a built-in symmetry in the $k - space$, regardless of the nature of the quantity $W(\vec{k})$ or, in our case, $Q(\vec{k})$. One therefore needs to chart $Q(\vec{k})$ only in a suitably selected half of the $k - space$.

The function $Q(\vec{k})$ normally looks quite messy and is full of oscillatory patterns. Since we always image spatially bounded objects, however, the area of the $k - space$ where $Q(\vec{k})$ reaches large values is limited to a central region. At large distances from the origin, $Q(\vec{k})$ becomes smaller than the ubiquitous experimental noise and it is therefore no longer charted. The area we use for data collection is called Field of View (FOV).

3.7.4 Echo formation

As mentioned earlier, the final goal in MRI is to chart the function $Q(\vec{k})$ at a set of points dense enough to make it possible to carry out, with a reasonable precision, the back-

61

transformation into $R-space$. To achieve this, hundreds of strategies have been developed, each one corresponding to a distinct MRI data acquisition technique. We will concentrate on the Cartesian $k-space$ grid.

Now, let's see how the signal, called an echo, is formed in MRI. Suppose we have a cylinder of water placed in the main magnetic field and suppose that upon RF excitation pulse ($t = 0$) we applied a constant field gradient $+\vec{G}_x$ for a period of time τ. The positions of the spins in the phantom are frequency encoded by this gradient. Figure 3.13 shows
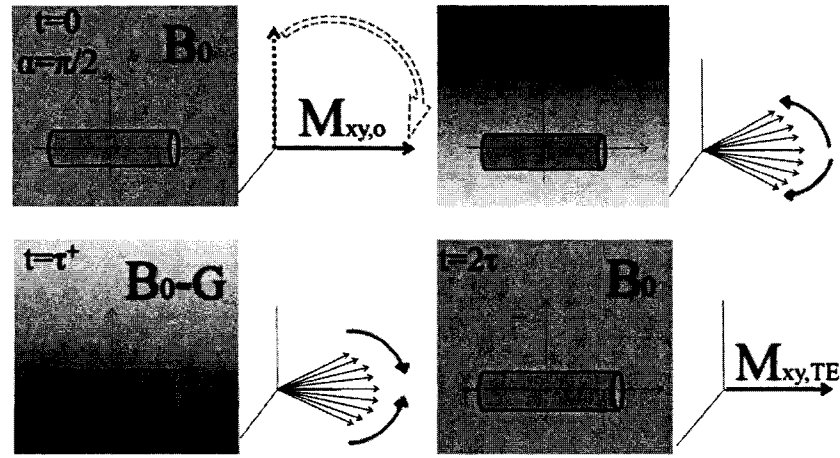
Figure 3.13: Gradient echo formation.

the behavior of the magnetization vector from the excitation time to the echo formation time. According to Eqn. (3.80), spins at position x during time $t = \tau$ will accumulate a phase of $\phi_{+G_x}(x,t) = \gamma G_x x \tau$. If at this time we flip the sign of the gradients, i.e. $-\vec{G}_x$, for some time interval τ', and collect data at the same time, we will observe the echo. During the time when negative gradient is applied, the spins will accumulate additional phase, $\phi_{-G_x}(x, t = \tau') = -\gamma G_x x \tau'$, resulting in total phase of $\varphi(x,t) = \phi_{+G_x}(x,\tau) + \phi_{-G_x}(x,\tau')$. The echo will be achieved when total accumulated phase is zero, i.e. at time $t = 2\tau$. Thus

62

the gradient echo condition is

$$\int G\left(t\right)dt=0$$

i.e. the zeroth moment of the gradient has to vanish. The time when this is achieved is

called echo time, TE.

Inverting the gradients is not the only means of inducing an echo. Consider a case

just like in the previous discussion, where the same cylinder with protons is placed in

the main magnetic field, and 90° RF pulse is applied along x-axis. As before, upon the

magnetization flip into the transverse plane, field gradient is applied for some time $t = \tau$.

Only now, instead of inverting the direction of the gradient before staring data collection,

we will apply a 180° RF pulse along the y-axis (see Figure 3.14). This will flip the position
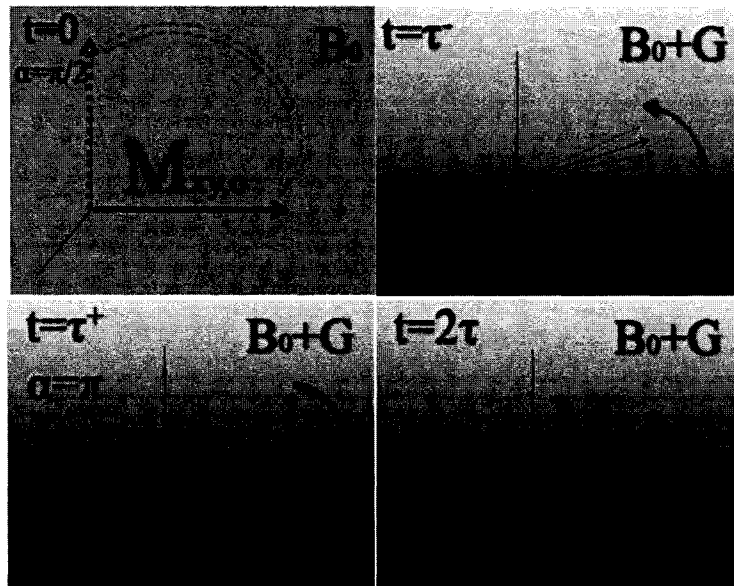
Figure 3.14: Spin Echo formation.

of the spins so that the spins that were previously in higher field region will be in lower

field region, thus forcing the faster spins to precess at a lower frequency and vice versa.

63

All this while keeping the gradient in the same direction. Then an echo will be induced at time $t = 2\tau$. This type of an echo is called "spin echo".

In general TEs in spin echo sequences are longer than those in gradient echo sequences, but the spin echoes have an advantage over gradient echoes in correcting for T_2^* effects. In fact, any T_2 measurement is based on a spin echo sequence, while T_2^* measurement - on gradient echo sequence.

The spatial direction, in which direction the gradient is used while collecting data is called "Read Out", or "Frequency Encoding" direction. Of course, in order to have information about a 3-dimensional body we need probe in all 3 directions. It is possible to apply gradients in all three dimensions, hence dividing the FOV into many voxels (volume elements) and acquiring a true 3D image of the sample. True 3D imaging is rarely used due to its lengthy acquisition times, and most of the time it is replaced by slice selective 2D imaging, where a thin slab of a sample is chosen to image. Then the sequence can be repeated for multiple slices to cover the whole sample.

3.7.5   Multislice Gradient Echo Imaging

The vast majority of the experiments described in this thesis used a spin-warp technique based on gradient echo formation. I will provide some details describing the basics of constructing such a sequence. The time diagram of this pulse sequence is presented in Figure (3.15). This is a repeated pulse sequence with a different phase encoding gradient value for each RF excitation (repetition time TR interval). Let us first look at the frequency encoding direction (x-gradient) - as in the above case, the gradient encodes the x spatial position into frequency, and creates one to one correspondence between Euclidian $R - space$
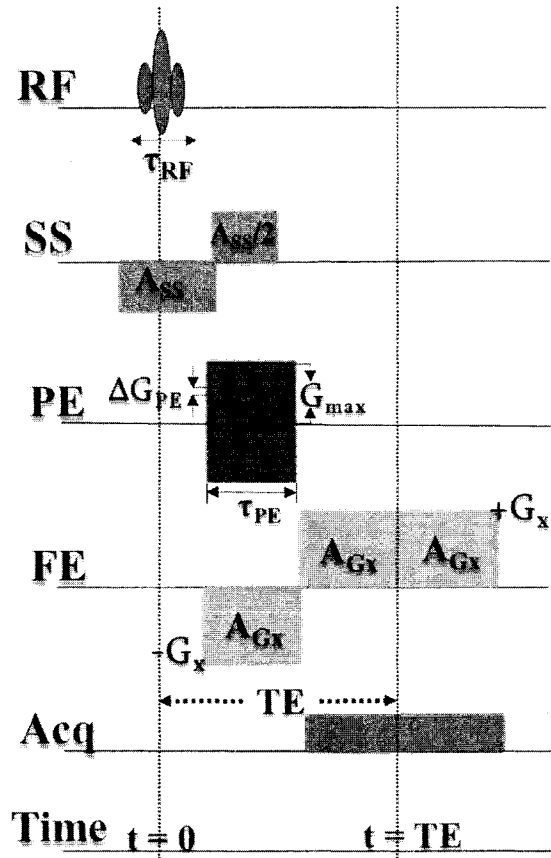
Figure 3.15: Time diagram for the gradient echo sequence.

65

and complex $k - space$.

The phase encoding, y-gradient, is on briefly before each acquisition, but is off during the data collection. Thus, the encoding by y-gradient is done. In this case the y-gradient sets up a spatially dependent phase distribution that remains fixed during the frequency encoding process. In other words, the y-gradient encodes spatial position into the phase of the magnetization (i.e. direction of $\vec{M}$), hence the name phase encoding gradient.

Finally, a constant z-gradient is applied during the RF pulse for time τ_{RF} and then reversed immediately after the RF pulse (see Figure3.15). This gradient forces the frequency of precession to be a linear function of position along the corresponding slice select direction. The goal is to excite a slice such that all spins in the slab from $-\Delta z$ to Δz have an identical phase and flip angle after the slice selection. To achieve this, the frequency profile of the RF pulse has to be unity over the range Δf of frequencies from $(-\gamma G_z \Delta z)$ to $(+\gamma G_z \Delta z)$ and zero elsewhere. This region is called the RF bandwidth, BW_{RF}. From this it follows, that the slice thickness is calculated as

$$\Delta z = \frac{BW_{RF}}{\gamma G_z} \tag{3.88}$$

for each RF pulse shape.

The slice select gradient induces dephasing across the slice. To correct for this accumulated phase, the gradient is reversed after the RF pulse is turned off. The duration of the reversed gradient is adjusted so that the spins realign in the transverse plane by the end of the application of the rephasing lobe, e.g. if accumulated by the end of the RF pulse phase is $\phi(z, \tau_{RF}) = \gamma G_{ss} z \tau_{RF}$, then a refocused gradient should be applied for

$$\tau_{rephase} = \frac{1}{2} \frac{G_{ss}}{G_{rephase}} \tau_{RF} \tag{3.89}$$

66

where 1/2 is used, because under the assumption that spins are tipped instantaneously, the dephasing takes place only during half of τ_{RF}.

For the pulse sequence described and presented in Figure (3.15), the signal can be written as

$$s\left(t'\right) = \int dx \left\{ \exp\left(-i\gamma G_x t' x\right) \int dy \left[\exp\left(-i\gamma G_y \tau_{PE} y\right) \int_{z_o - \Delta z}^{z_o + \Delta z} dz \varrho\left(x, y, z\right) \right] \right\} \qquad (3.90)$$

where $t' = t - TE$, and z_o refers to the center of the excited slice. If we transfer now into the $k - space$, and integrate over the slice thickness, the signal will become

$$s\left(k_x, k_y\right) = \iint \varrho\left(x, y, z_o\right) \exp\left(-2\pi i \left(k_x x + k_y y\right)\right) dx dy \qquad (3.91)$$

with the actual image being the 2D FT of the $k - space$ signal.

As a last note here, let's take a look at how the $k - space$ looks and what trajectory this pulse sequence describes. As shown in Figure (3.16) and discussed earlier, $k - space$
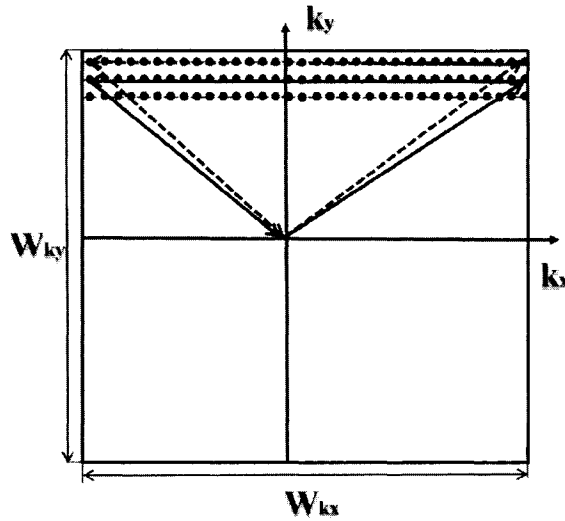
Figure 3.16: $k - space$ for the spin-warp pulse sequence.

trajectories always start at the origin. Then $\vec{k}$ moves to the position defined by the applied

67

gradients G_x and G_y, after which follows the data acquisition along k_x. Then it all starts over, but with a new G_y, hence k_y value until the FOV is fully covered.

3.8 Hyperpolarized Noble Gas MRI

3.8.1 Pulmonary imaging

Until now we were discussing thermal polarization and conventional proton imaging. This technique assesses the distribution of protons in any given area of the body. In the lungs, the airspaces are virtually devoid of protons, but the soft tissues of the organ do contain them. Furthermore, pathological conditions may change the number of (free moving) protons. For instance, edema, inflammation, tumors, and hemorrhage increase this number (and hence the signal in MRI), whereas fibrosis or calcification will decrease this number (and will lead to signal loss at MRI).

Due to low tissue density in the lungs signal is much lower than that acquired from other organs. Moreover, protons in the lung tissue have an inconveniently short coherence time (T_2^*) dictated by numerous gas-tissue interfaces present in the lungs. An alternative to endogenous contrast is the administration of external contrast agents. Recent techniques employing paramagnetic O_2, as well as Gd-enhanced imaging techniques are able to image the lung parenchyma or perfusion of the lung, and indirectly give information about lung ventilation ([89], [68], [30]).

The initial interest and development of the nuclear hyperpolarization techniques was motivated by topics in nuclear and particle physics. For example, polarized ^3He cells are used as spin filters in low-energy nuclear physics experiments to produce low-energy polarized neutron beams (LANL $npd\gamma$ experiment). ^3He possesses a huge spin-dependent

68

absorption cross-section as a result of which only neutrons with spins parallel to those of the ^3He nuclei are transmitted, resulting in a polarized neutron bean.

Introduction of hyperpolarized gases in the nuclear physics community [57] and their implementation in medical imaging [58] as contrast agents provided a signal five orders of magnitude higher than that achieved at thermal equilibrium in commonly used magnetic fields. In hyperpolarized gases nuclear spins are artificially aligned with the magnetic field in the course of optical pumping/spin exchange [4], creating a magnetization that, unlike its thermal counterpart, is non-renewable and independent of the magnetic field.

^3He and ^{129}Xe are the only two noble gas isotopes with spin $-\frac{1}{2}$ nuclei that are appropriate for MR applications. The high degree of polarization, attainable for ^3He, as well as a gyromagnetic ratio 2.74 times greater than that of ^{129}Xe and comparable to that of the proton makes ^3He gas phase imaging quite easy. ^3He is the gas of choice for gas space imaging of the lungs. ^{129}Xe on the other hand is lipophilic, and unlike ^3He it dissolves into tissue and blood. Besides, it is very sensitive to its environment and undergoes a wide range of frequency shifts which facilitates studying the pulmonary air-sacs, septum and blood separately. Low polarization levels available for xenon, slowed if not hindered its application in human MRI. With the breakthrough in the xenon polarization technique human studies became feasible.

3.8.2 ^{129}Xe in NMR

Xenon was first used in NMR by Ito and Fraissard in 1980 for the study of porous solids [77]. They were looking for an inert molecule sensitive to its environment, and interactions with other chemical compounds. Among the noble gases, xenon has the largest electron

69

shell that is easily deformed. As a result of this, xenon displays the largest range of chemical shifts [65].

The non-equilibrium magnetization with four to five orders of magnitude increase of the signal allowed for very fast sampling with small flip angles. The need to signal average is eliminated, as well as the necessity to allow for T_1 relaxation before the next pulse is applied. The low density of the polarized xenon gas phase compared to water, is balanced by its high polarization, so that the magnetization density of ^{129}Xe of the same order as the thermal magnetization of protons at few tesla. But most importantly, most systems under study are devoid of xenon and therefore incapable of producing background signals at the xenon frequency.

General Properties In the atmosphere xenon can be found in minute amounts (concentration of 87ppb). Sir William Ramsay and Morris Travers discovered Xenon in 1898 by evaporating liquid air components. It is gaseous at standard temperature and pressure, easily liquefied or frozen with a boiling point at $165.1K$ at $1atm$ and a melting point at $161K$ at $1atm$. Xenon has an atomic number of $Z = 54$ and nine naturally occurring isotopes with atomic masses ranging from 124 to 136. ^{133}Xe is used in nuclear medicine, while ^{129}Xe and ^{131}Xe, with natural abundance of 26.4% and 21.29% respectively, are both stable. These isotopes possess a non-zero nuclear spin: 1/2 for ^{129}Xe and 3/2 for ^{131}Xe, which makes them a target of NMR studies. Of the two isotopes, the former's gyromagnetic ratio is 4 times as large as that of the latter, resulting in much higher sensitivity. The relaxation times are shorter for ^{131}Xe due to its quadrupole moment making the least favorite of the two when it comes to NMR applications.

T (K)	Substance	Preparation	L	$Mol_{Xe}/Mol_{solv.}$
310.15	*Water*		0.0834 (2)	
	Plasma	*Air*	0.091 (2)	
		N_2	0.090 (2)	
		O_2	0.093 (2)	
	Eritrocytes	*Air*	0.190 (8)	
		N_2	0.200 (8)	
		O_2	0.170 (10)	
298.15	*Albumin*		0.2382	
303.15			0.1954	
310.15			0.1493	
298.15	*Fat*		2.0606	
303.15			1.9630	
310.15			1.845	
294.15	*Albumin*			1.1
	Haemoglobin			1.9
	Methaemoglobin			1.9
Other				
310.15	0.9% *NaCl*		0.078 (7)	
	Olive oil		1.79 (4)	

Table 3.1: Ostwald coefficient of xenon, L, in different substances of biological relevance (Clever, 1979)

71

Xenon is highly soluble in lipids. Its Ostwald coefficient in oil or fat tissue is ~ 10 times higher than that in water [32]. Table (3.1) illustrates the solubility of xenon in different substances. The values are taken from [32]. Most measurements were done using ^{133}Xe isotope. The data shows solubility dependence not only on the temperature but oxygenation level of the blood. Since xenon molecules are electrically neutral and non-polar, they avoid mixing with water (and are hydrophobic as any other noble gas). On the other hand, xenon dissolves in lipids and other neutral environments.

Anesthesia The first application that Xe ever found in medicine was in the role of an anesthetic. Such properties of Xe were discovered by Behnke who observed the "drunkenness" effect in deep-sea divers [78]. Xenon was first used as an anesthetic agent in experiments on mice in 1946 [43]. In humans xenon produces an anesthetic effect at minimal alveolar concentrations of 71% atm [76]. Xenon has shown many advantages over other anesthetics: it is non-teratogen, i.e. it does not interfere with the development of the fetus, has analgesic effects at $\sim 20\%$ concentrations; offers better regional perfusion of organs, does not influence the body temperature, nor does it contribute to the destruction of the ozone layer, and has a rapid washout. Thus xenon is mostly harmless to the organism [78].

Chemical Shift As mentioned, Xenon nucleus is cloaked by a large electron cloud. The constituents of the cloud can be thought of as a current, that induces a magnetic field opposite to the field imposed on the sample. Therefore the effective field experienced by the nucleus at the core of the atom is screened by the electron could. This effect however varies depending on the chemical environment immediate to the atom in question. Indeed,

the very electrons that make up the atomic cloud, can interact with their peers that occupy the electron clouds of the neighboring elements (air, tissue etc.). This interaction will affect the overall effective field seen by the nucleus [9]. This phenomenon is called a chemical shift, and is typically quatified by a parameter σ. Xenon possesses a "chemical shift" range of about 350ppm in solution and ~7500ppm in compounds [6] (Figure 3.17).
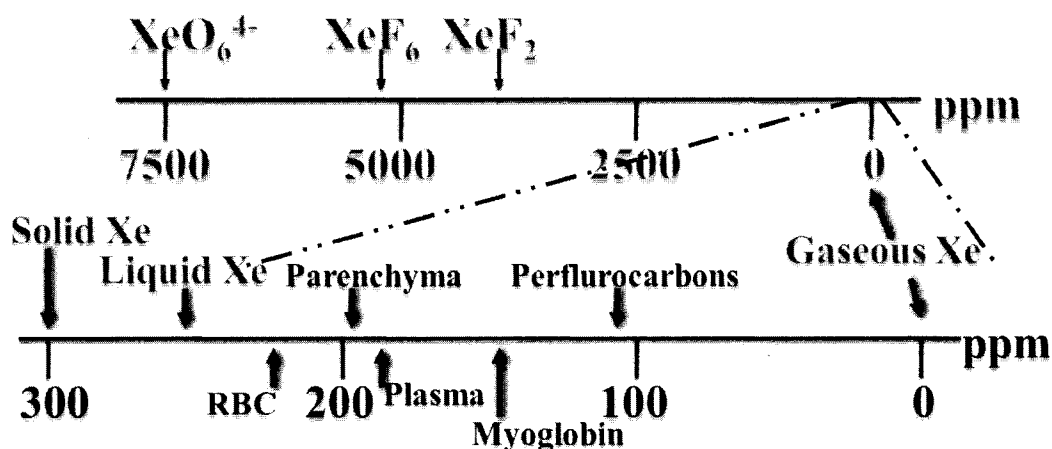
Figure 3.17: Chemical shift range of xenon.

The longitudinal relaxation rates and the range of the chemical shifts in gaseous and liquid xenon was extensively studied by Streever and Carr [67] and later by Hunt and Carr [18]. Xenon NMR was used extensively in microporous material studies [54], as well as studies of dissolved-phase dynamics and time-dependent diffusion, which can be used to obtain information about surface-to-volume ratio and torturosity [70], [71], [45]. As shown by Spence et al. [56], xenon can be used as a biosensor due to its high sensitivity to very small changes in the surrounding environment.

3.8.3   In vivo MRI with Hyperpolarized Xenon

In 1994 Albert et al.[58] introduced hyperpolarized xenon to the realm of medical imaging.

73

They demonstrated xenon gas images and images of the human oral cavity, as well as measured chemical shifts of xenon in lipids, proteins and water all within 20 *ppm*. In 1997 Mugler *et al.* *[37]* presented the first xenon images in a human chest, along with xenon spectra from the chest and the head. The spectrum from the chest had several peaks - one large peak at 0 *ppm* from the gas state and three more about 200 *ppm* away (185 *ppm* - blood plasma, 196 *ppm* - lung parenchyma, 216 *ppm* - RBC). The head spectrum showed two peaks - at 0 *ppm* (gas) and 196 *ppm* (brain tissue). They also estimated the time it takes the xenon signal to reach its maximum in the brain to be 5 *s*, which is consistent with previously reported blood transit times of order of 5 *s*.

In 2004 Kilian *et al.* [82] looked at the human brain perfusion using hyperpolarized xenon. They analyzed the data using a modified version of previously reported xenon uptake model by Peled *et al.* [75], where they account for the depletion of polarization by RF pulses during a breath-hold. The results suggest that the peaks at 196.5 ± 1 *ppm* and 193 ± 1 *ppm* corresponded to the xenon dissolved in grey and white matters, respectively. According to their results longitudinal relaxation in the gray matter exceeded that in the white matter.

Later that year Kilian *et al.* [83] reported temporally- and spatially-resolved *in vivo* spectroscopy of the human brain. The main source of improvements in this work was the use of a commercial xenon head coil. These measurements supported the earlier reported chemical shift values (196 and 193 *ppm*).

Another major avenue of hyperpolarized Xenon NMR research is its application to lungs. Mansson *et al.* [73] in 2003 studied average alveolar wall thickness in healthy rats and rats with acute pulmonary inflammation lung injury using hyperpolarized ^{129}Xe.

74

They measured pulmonary perfusion, capillary diffusion length and mean transit times. Diffusion length obtained in the healthy rats was 8.5 ± 0.5 μm, while in the diseased rats it was 9.9 ± 0.6 μm. They reported differences in the measured values of the capillary diffusion length, but found no differences in average alveolar wall thickness and mean transit time.

Some more animal lung imaging was done by Ruppert *et al.* [49]. They investigated lung function using polarization transfer techniques. They examined the dependence of the fractional xenon diffusibility rate on the lung inflation, as well as diffusion time, using animal models. The reported gas exchange times were of the order of tens of milliseconds, and dissolved state diffusion constant of 3.3×10^{-6} cm/s. These measurements will be discussed in more detail in later chapters.

75

4.1 UNH Xenon Polarizer

4.1.1 Polarizing ^{129}Xe

In the case of conventional MRI the magnetization in the sample being studied originates in the protons. The "thermal" magnetization of the ^1H nuclei is induced by placing the patient, whose body is naturally rich with hydrogenous tissues, in a strong magnetic field. The quantization axis is then defined and the protons, spin-$\frac{1}{2}$ particles, align their magnetic moments along the magnetic field. However, as mentioned in earlier chapters this magnetization is limited in that it requires great magnetic fields (few Tesla). In addition, since only areas containing protons can yield an image, such volumes as the lung gas spaces filled with air, cannot be imaged using conventional MRI methods.

In our experiments, in order to gain information about gaseous compartments within the lungs, as well as the gas exchange and other properties of the organ, we utilized polarized ^{129}Xe. The nuclei of this noble gas can be polarized in the two-fold process of Spin Exchange Optical Pumping.

Optical Pumping The first part of the process involves a dense Rb vapor placed in a weak ($\sim$ 30 G) magnetic field $\vec{B}_0$. The low melting point of Rb (39^oC) allows achieving its vaporized state by heating the metal to relatively moderate temperatures (160^oC). Once in the magnetic field, the otherwise degenerate states $5S_{1/2}$ and $5P_{1/2}$ of the Rb atom split

into sublevels (Zeeman Splitting) (see Figure4.1).
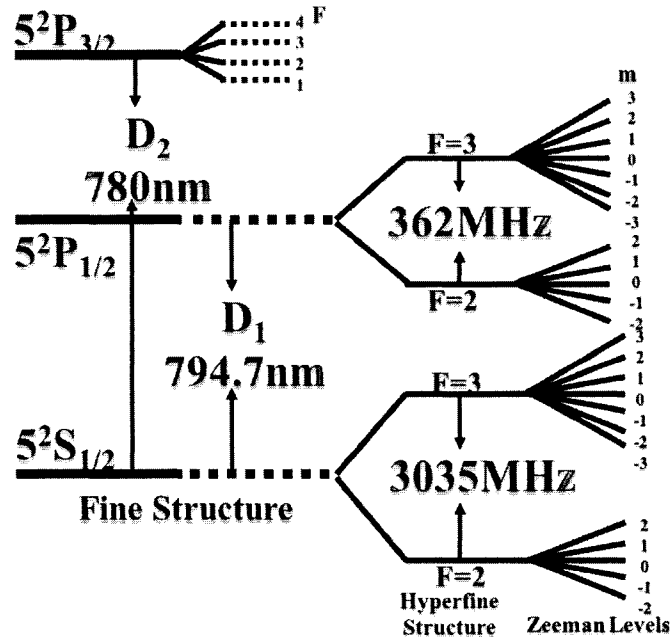
Figure 4.1: ^{85}Rb Level Diagram.

At this point the single valence electron of the Rb atom is irradiated by circularly

polarized laser light of positive helicity σ_+. The frequency of the laser light (794.7 nm) is

tuned to the D_1 absorption line of the Rb atom, which is the transition between the $S_{1/2}$

and $P_{1/2}$ states. From the conservation of angular momentum, transitions from $S_{1/2,-1/2}$

to $P_{1/2,+1/2}$ are allowed. A mixing occurs between $P_{1/2,+1/2}$ and $P_{1/2,-1/2}$ states. From the

two sublevels of the excited state, the atom decays back to $S_{1/2,-1/2}$ and $S_{1/2,+1/2}$. While

the latter state is the desired destination, the former is continuously pumped by the laser.

As a result the $S_{1/2,+1/2}$ population gradually builds up in the Rb vapor. The decay to the

ground state happens through one of the two channels - spontaneous emission or quenching

collisions. Photons emitted in such transitions are unpolarized on average and therefore are

77

capable of depolarizing other atoms. In order to mitigate this effect, the cells containing Rb are supplied with some amount of N_2 molecules, which can quench the excited atoms through collisions and absorb the extra energy of the excited state into vibrational degrees of freedom. In order to achieve the desired effect with N_2, densities of ≥ 0.1 amagat are used.

For such densities the hyperfine structure of the alkali D_1 lines are unresolved. Therefore the interaction between the alkali atom and a photon can result only in flipping the electron spin, leaving the nuclear spin unchanged. Under these conditions it is valid to assume that the density matrix of the alkali atoms follows the "spin-temperature" distribution [53] described by a single parameter β, spin temperature parameter:

$$\rho = \frac{\exp\left(\beta I_z\right)\exp\left(\beta S_z\right)}{Z} \tag{4.1}$$

where Z is the partition function. Then the electron polarization is

$$P_{Rb} = \frac{N_\uparrow - N_\downarrow}{N_\uparrow + N_\downarrow} = \frac{\exp\left(\beta/2\right) - \exp\left(-\beta/2\right)}{\exp\left(\beta/2\right) + \exp\left(-\beta/2\right)} = \tanh\beta/2 \tag{4.2}$$

However the Rb nuclear spin interacts with its electron spin through the hyperfine interaction, which means that the electron spin slowly transfers into the nuclear spin thereby reducing the polarization rate by a polarization dependent factor defined as

$$1 + \varepsilon\left(P\right) = \sum_{isotopes} \frac{\langle F_z \rangle}{\langle S_z \rangle} = \sum_{isotopes} \left[1 + 2\left(\vec{I}\cdot\vec{I} - I_z^2\right)\right] \tag{4.3}$$

where $\varepsilon\left(P\right)$ is the slowing down factor. Then the electron spin evolution due to optical pumping will be

$$\frac{d\langle S_z \rangle}{dt} = \frac{R}{1 + \varepsilon\left(P\right)}\left(\frac{1}{2} - \langle S_z \rangle\right) \tag{4.4}$$

78

where $R = \int_0^\infty \Phi\left(\nu\right)\sigma_{opt}\left(\nu\right)d\nu$ is the mean photon absorption rate for unpolarized atoms, while $\Phi\left(\nu\right)$ is the photon flux and $\sigma_{opt}\left(\nu\right)$ is the spectral distribution of the absorption cross section of the alkali atom. Taking into account the slowing down factor the spin build-up rate of alkali electron is usually on the order of $10^5 - 10^6\ s^{-1}$.

Spin-Exchange This is the process by which the spin of the alkali metal (Rb) electron is transferred to the nucleus of the noble gas (^{129}Xe). In fact there are two channels by which the exchange can transpire - through binary collisions and by forming van der Waals molecules. The conservation of energy and momentum during the formation of van der Waals molecules requires the presence of a 3rd body. The binary collision channel dominates at higher pressures, while van der Waals formation takes over at low pressures.
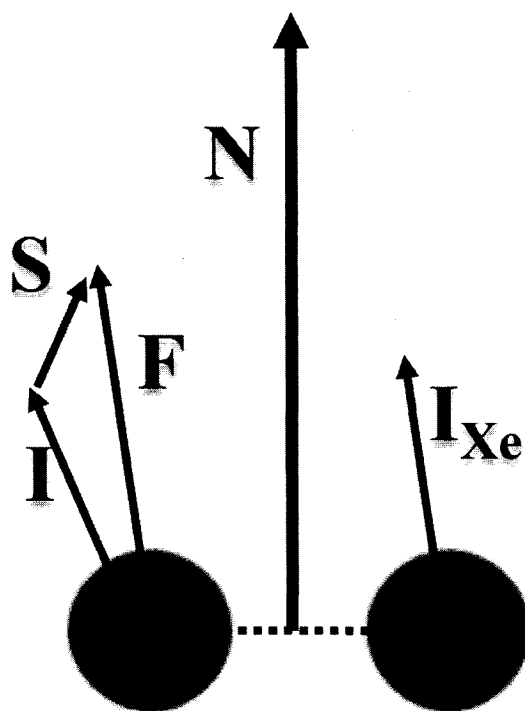
Figure 4.2: Schematic of the angular momenta of $Xe - Rb$.

79

If $\vec{S}$ and $\vec{I}$ are the electron and nuclear spins of the Rb, and $\vec{I}_{Xe}$ is the nuclear spin of ^{129}Xe, then the Hamiltonian describing the spin-exchange interaction can be written as

$$H_{se} = \alpha \vec{S} \cdot \vec{I}_{Xe} + \gamma \vec{S} \cdot \vec{N} + A \vec{I} \cdot \vec{S} + (O) \tag{4.5}$$

where $\vec{N}$ is the net orbital angular momentum of the $Rb - Xe$ pair (Figure(4.2)). The first term in Eqn. (4.5) describes the coupling of the electron's spin and the spin of the ^{129}Xe's nucleus. This term is responsible for the spin-exchange. The 2nd term describes the process of spin rotation which results in the transfer of the spin to the net angular momentum. This term does not contribute to the nuclear polarization of ^{129}Xe but reduces the Rb polarization. The ratio of the amount of angular momentum transferred to $\vec{N}$ and $\vec{I}_{Xe}$ can be calculated from the amplitudes of the corresponding couplings and has been estimated by Zeng [88] to be on the order of 1/3. The 3rd term is the interaction between the nuclear and electron spins of the Rb atom itself.

In order to gain a net xenon nuclear magnetization, spin exchange rates γ_{SE}, coupled with optical pumping rates must prevail over the various relaxation mechanisms. Thus, the ^{129}Xe nuclear polarization can be written as

$$P_{Xe} = P_{Rb} \frac{\gamma_{SE}}{\gamma_{SE} + \Gamma},$$

where Γ describes the relaxation effects and should be small compared to γ_{SE} to achieve high polarizations.

4.1.2   Polarizer at BWH

Running the polarizer The xenon for the experiments was polarized using a polarizer developed and built at University of New Hampshire, which is described in detail in [34] as well as doctoral dissertation of Iulian Ruset [35]. Here we will provide a short description of the polarizer and its operation at the new location at the Brigham and Women's Hospital, in Boston, Massachusetts.
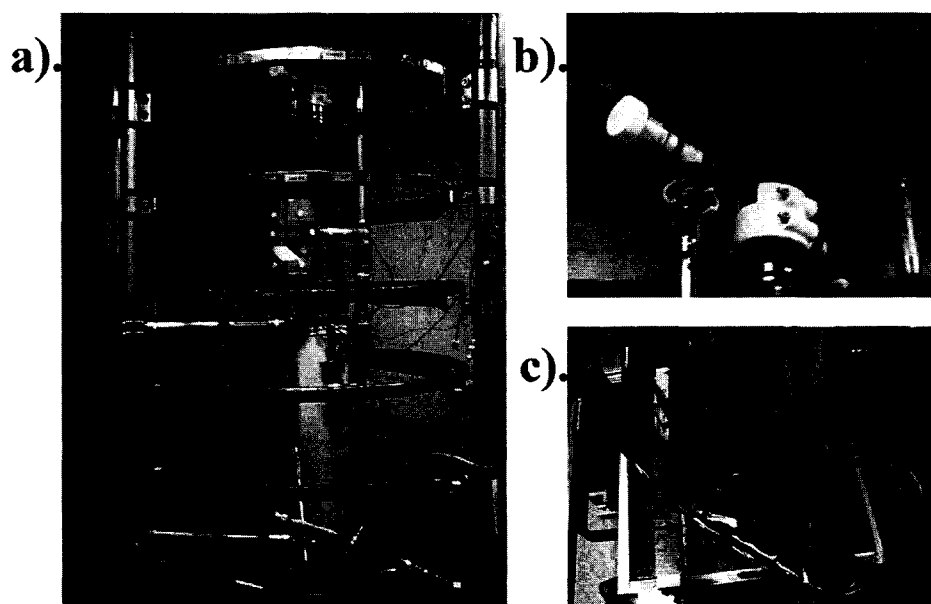
Figure 4.3: UNH polarizer installed and operating at the Brigham and Women's Hospital.

Figure (4.3) shows the polarizer installed at BWH. The seven coils, connected in series, that sit on the metal rack provide a low magnetic field ($30\ G$) necessary for optical pumping of the Rb. The coils position is adjusted while observing the NMR signal from the xenon. The position of the coils is optimal when the NMR peak is the narrowest and the signal is at its maximum.

The optical set-up of the polarizer is placed in a black box and mounted on top of the polarizer. It is adjusted so that the laser light coming out of the box travels down

the polarizer cell without hitting the walls minimizing the reflections from the wall. This is the most important adjustment of the polarizer, since it has the largest effect on the polarization numbers observed. Currently we are using 5 Coherent Fiber Array Package (FAP) lasers connected in parallel to a single power supply. Each of the lasers provides a maximum power output of 30 W when running at 35 A. The FAPs are mounted on a cooling base connected to a chiller, that circulates the chilling fluid through the mount.

The light from the separate lasers is combined using a 5 *meter* long fiber optic. Figure (4.4) shows the dependence of the combined laser power on the current at the top of the polarizer cell, just before entering, and at the bottom, right after the exit. The combined
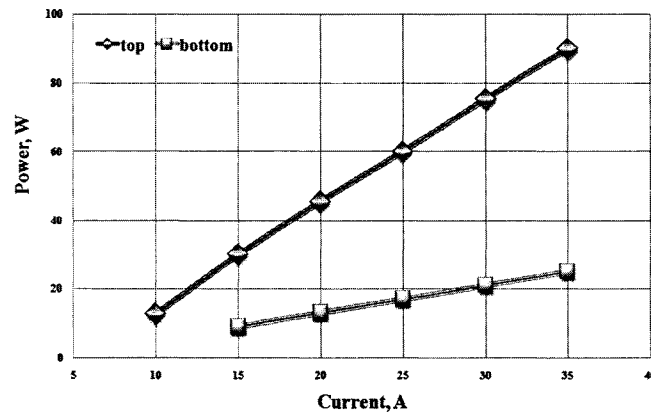
Figure 4.4: The laser power from all 5 FAPs, measured just before entering the polarizing column, and right after the exit.

beam has a spectrum with $FWHM$ of $\sim 1.5\ nm$ and is centered at $794.7\ nm$ when operating current is 35 A and cooling fluid is at 15^oC.

The polarizer cell is a 182 cm long Pyrex glass cell consisting of two parts welded together. The bottom part of the cell has a spiral form with little pools for Rb, and it is

82

connected at the bottom to the top half of the cell by a tube running through the center of the spiraling part. The cell hangs on a support, bottom half immersed inside a PYREX glass oven, inside which heated oil is being circulated. The oil is heated by a Neslab heating bath, the temperatures used are between 140 and 180^oC, with 160^oC being the optimal observed temperature. The glass oven is insulated using two layers of a fiber glass.

Having the lower part of the polarizer cell immersed in the hot oil ensures the high density of the Rb vapor. As gas enters, it first flows through the spiral part towards the bottom of the cell, filled heavily with Rb vapor. Then the saturated gas mixture moves up the central tube of the cell against the laser light, which shines from the top of the column. This counterflowing feature of the polarizer is the main difference compared to other polarizing systems. With this counter-flowing design, the laser light has the least energy when the polarization process just starts at the bottom of the cell, and as gas moves up, laser energy increases. The polarization is expected to be the highest at the very top of the column. Another unique feature of the system is that the second half of the cell is at room temperature forcing the Rb to condense on the walls while still illuminated by the light, hence ensuring the maximum preservation of xenon polarization.

When the polarized gas mixture reaches the top of the polarizer, it travels down a side tube, which is out of the laser light, into a spiral cell, that is immersed into a U-tube filled with liquid nitrogen, where polarized xenon is frozen and separated from the buffer gases. This U-tube with the freezing spiral cell is seated inside a permanent magnet with a field of 0.3T. The system operates at sub-atmospheric pressures (500 Torr), and pressure is controlled by a pressure controller that is attached after the freeze-out spiral cell and right before a vacuum pump.

After a desired amount of polarized xenon is frozen, the gas flow is shut down, together with the laser, and the polarizer cell is isolated, while the freeze-out cell is evacuated to ensure that buffer gases are eliminated from the cell. Then the spiral cell is isolated while still immersed into LN2 and sitting inside the permanent magnet block. Then it is connected to another vacuum pump through a tee, which is connected to either a Tedlar bag or a glass cell. After the thawing system is evacuated, the spiral cell, still immersed in the liquid nitrogen, is opened to the system and LN2 U-tube is removed and replaced with a hot water container to start the thawing process. It is necessary to ensure fast thawing, since the longitudinal relaxation time for xenon in liquid phase is on the order of seconds. After the thawing is completed the cell or a Tedlar bag is placed inside a transfer suitcase and transferred to the magnet room, where the experiments are performed. The pressure in the thawing system is monitored and recorded during the thawing process, and later used in the polarization calculations.

Polarization measurements The polarization of the gas depends on the xenon flow rates used during the process. With lower flow rates the partial pressure of xenon is lower in the gas mixture and polarization values are higher. However it takes longer to polarize and accumulate the polarized xenon. On the other hand to reduce the time it takes to polarize and freeze the xenon, higher xenon flow rates can be used which will result in lower polarization. Thus, in order to optimize the final polarization of the gas prepared for an experiment, one needs to consider the amount of gas necessary, take into account the relaxation time of frozen xenon and polarization dependence on the flow rate. Hence, mapping the latter is of great importance.

84

The polarization calculations are based on the fact that the measured signal is proportional to the number of polarized ^{129}Xe spins, which is in turn proportional to the number of spins in the given volume (PV), natural abundance of the xenon gas used (α), number of averages taken (N), the amplifier gain used for the measurements (G) and of course the flip angle used $(\sin(\theta))$. The polarization of the hyperpolarized xenon is calculated from the comparison of the signals from the thermal and polarized xenon samples using the ratio

$$\frac{S_{HP}}{S_{TH}} = \frac{\vartheta_{HP}}{\vartheta_{TH}} \cdot \frac{P_{HP}}{P_{TH}} \cdot \frac{V_{HP}}{V_{TH}} \cdot \frac{\alpha_{HP}}{\alpha_{TH}} \cdot \frac{G_{HP}}{G_{TH}} \cdot \frac{N_{HP}}{N_{TH}} \cdot \frac{\sin(\theta_{HP})}{\sin(\theta_{TH})} \cdot \frac{\exp(-t/T_{1,HP})}{\exp(-t/T_{1,TH})} \tag{4.6}$$

where ϑ is the polarization of the sample, P is the partial pressure of the xenon gas in the cell, acronym HP stands for HyperPolarized, while TH is for THermal.

The thermal polarization itself is given by Boltzmann's equilibrium distribution (using Eqn. 3.41)

$$\vartheta_{TH} \approx \frac{\mu B_o}{k_B T} \tag{4.7}$$

where T is the absolute temperature. For xenon sample at 0.2T magnetic field and room temperature the thermal polarization is 3.75×10^{-7}. For polarization measurements we collect 128 averages with the thermal cell ($V = 3L$, $P_{Xe} = 4atm$, $\alpha_{129} = 86\%$). Since $T_1 = 0.9s$ for this cell, using $TR = 6s$ allows us to neglect the longitudinal relaxation effects.

Upon thawing, the polarized xenon is transferred to the magnet room, placed in the magnet and a single FID is taken to measure the polarization in the cell. Then the data are Fourier transformed, properly phased and integral of the real part of the signal is measured. The same is done to the signal collected on the thermal sample. Then the polarization of the hyperpolarized sample is calculated using Eqn. (4.6). Figure (4.5) presents the dependence

85

of the xenon polarization on the xenon flow rate. All other parameters (such as oven temperature, laser current etc.) were kept constant during these runs.
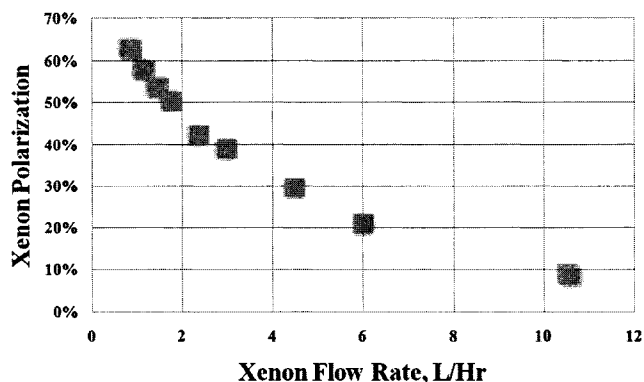
Figure 4.5: Xenon polarization mapping. Depending on the time available and amount of gas required for an experiment, the xenon flow rate in the polarizer can be adjusted resulting in the optimal xenon polarization.

Polarization levels were measured for most of the experiments performed with human subjects. In these cases, since the Tedlar bag filled with polarized xenon was used for the experiment, the polarization was measured using the spiral cell with the xenon left in it after thawing. Since these polarization measurements were performed after the human experiments, sometimes 20-30 minutes after thawing, we had to take into account the $T_1 = 40$ min relaxation time of the xenon in the spiral cell. Polarization levels of 40-50% were routinely measured after human experiments.

4.2 MRI setup

4.2.1 The scanner and the software

The studies described here were performed at the Brigham and Women's Hospital using a

86

General Electric Signa Profile IV MRI magnet. It is a 0.2 *Tesla* permanent magnet and the field changes depending on the temperature. Drifts of order of 2 ppm a second are commonplace for the magnet. The GE system was interfaced with a broadband Tecmag Apollo research spectrometer that took over the control of the gradient coils and gradient power amplifiers of the GE system. However, a completely separate RF system was constructed for 2.361 MHz, which is the xenon Larmor frequency at this field strength.

Since the 0.2 T magnet was clinically used in the past, the Faraday room, where it is located, is quite "clean" around proton frequency (8.535 MHz), while the xenon resonance frequency neighborhood was not as noise-free. To reduce the noise, a copper mesh box was built on the magnet bed around the RF coil. A sliding patient bed was built to ease the process of climbing inside the RF coil.

4.2.2 Human size RF coil

All human experiments are performed using an RF coil by Mirtech, Inc. The coil consists of two rounded square loops in near Helmholz configuration. The distance between the sides of the coil is 46 cm, providing enough space for a subject to slide in.

Flip Angle Calibration   In experiments with hyperpolarized gases it is essential to minimize losses of the non-equilibrium gas magnetization. Thus it is crucial to use the available gaseous phase xenon pool with utmost care, which requires a careful flip angle determination.

The flip angle calibration for hyperpolarized gases is based on the following observation. Suppose at time $t = 0$ the initial polarization M_o is along the main magnetic field, i.e. $\vec{M}_{\parallel}(t = 0) = M_o\hat{k}$, and $\vec{M}_{\perp}(t = 0) = 0$. Then an RF pulse with a flip of α^o is applied,

87

which will create transverse magnetization and redistribute the magnetization as

$$M_{\parallel} = M_o \cos{(\alpha)} \qquad (4.8)$$

$$M_{\perp} = M_o \sin{(\alpha)}$$

Now, if we apply another RF pulse of the same energy we will have

$$M_{\parallel}^{n=2} = [M_o \cos{(\alpha)}] \cos{(\alpha)} \qquad (4.9)$$

$$M_{\perp}^{n=2} = [M_o \cos{(\alpha)}] \sin{(\alpha)}$$

where n is the number of the RF pulse applied. If we continue in the same manner, after the nth pulse we will see

$$M_{\parallel}^{n} = M_o \cos^{n}{(\alpha)} \qquad (4.10)$$

$$M_{\perp}^{n} = M_o \cos^{n-1}{(\alpha)} \sin{(\alpha)} \qquad (4.11)$$

Then, if a number of consecutive simple FIDs are acquired, each followed by a set of spoiler gradients to dephase any residual transverse magnetization preceding the next RF pulse, the signal can be fit to the Eqn. (4.11) to deduce the value for the used flip angle α. In this discussion we neglected the relaxation of the magnetization due to inherent T_1 spin-lattice relaxation. In practice the time between consequent RF applications is kept much shorter than the longitudinal relaxation in a phantom used.

The flip angle calibrations were done on a number of gaseous phantoms, including 1 Liter spherical glass cell and a 2 liter Tedlar bag filled with hyperpolarized xenon. Then the phantom is placed in the middle of the magnet, and the FIDs are acquired. The time between consequent RF applications, or repetition time TR, was kept short (on the order of 250 ms) to mitigate longitudinal relaxation effects ($T_1 = 120$ min in a glass cell and 40 min

88
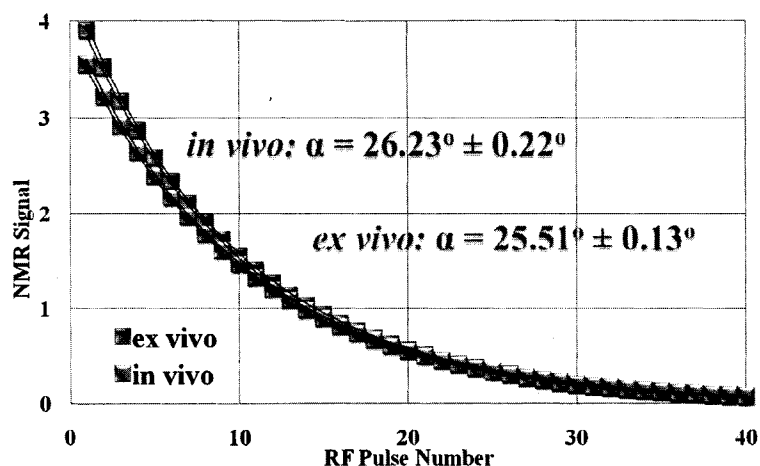
Figure 4.6: Flip angle calibration done on a Tedlar bag and repeated with a human subject. For the *ex vivo* run we obtained $25.5^o \pm 0.1^o$, while *in vivo* experiments provided $26.2^o \pm 0.2^o$ for the flip angle values. The lines in the plot show 95% confidence region.

in a Tedlar bag). Then the time data is Fourier Transformed and properly phased, which is followed by integrating the real part of the signal. Then the sequence of the integral values is fit to Eqn. (4.11). Figure (4.6) shows a sample result from such a flip angle calibration experiment. In this particular case the experiment was done on a Tedlar bag filled with 1Liter of natural abundance xenon. The flip angle is calculated to be $25.51^o \pm 0.13^o$. In the same plot we present similar experiment done *in vivo*, where all parameters of the pulse sequence were kept the same to allow comparison of the flip angles. For a human subject we obtained flip angle of $26.23^o \pm 0.22^o$. From the small difference between the flip angles ($\sim 3\%$) it follows that the subject only slightly loads the coil.

We placed a broadband pick-up coil on the side of the human coil to monitor the field created by the RF coil. We used the information gained from the broadband coil to confirm the flip angle calibrations done on a gas phantom, as well as check the load introduced by

89

the subject. Of course , the information provided by the pick-up coil is relative and in order to quantify the flip angle values, we still need to determine at least one value for the flip angle. This can be done using a thermal xenon sample.

The thermal sample we use is a 3-Liter spherical glass cell, filled with 4 atmospheres of xenon and 2 atmospheres of oxygen. Oxygen is added to reduce the longitudinal relaxation time of xenon, hence shorten the NMR signal acquisition times. In the given configuration, $T_1 = 0.9$ s for the thermal sample. To collect a signal with $SNR = 150$ (after a Gaussian appodization), we collect 128 averages and allow 6 s between the consequent FIDs for the transverse polarization to relax back to the longitudinal plane.

Using the thermal sample, we can determine the 90° flip as the one with the highest signal, and relate that to the measurement done with the broadband pick-up coil. After this, the relative measurements done with the pick-up coil can be quantified. Another application of the pick-up coil is monitoring the RF pulse shapes, as well as time constants of the electronics.

$\underline{B_1\text{- field mapping}}$ Since the subjects occupy most of the space inside the coil, one expects the RF field, B_1, to have a strong spatial dependence in the chest region. We studied the field created by the drive coil and mapped the flip angle over the region of interest, i.e. over the field of view that will be used in the imaging experiments. For our experiments it is a square region with 300 mm long side.

For these studies we used a 1 liter glass cell filled with hyperpolarized natural abundance xenon. The flip angle was probed at 25 different positions within the FOV. For a coil in Helmholtz configuration one expects to see a saddle-like behavior of the magnetic

90

field. Figure (4.7) presents an interpolated fit to the acquired map normalized to the value
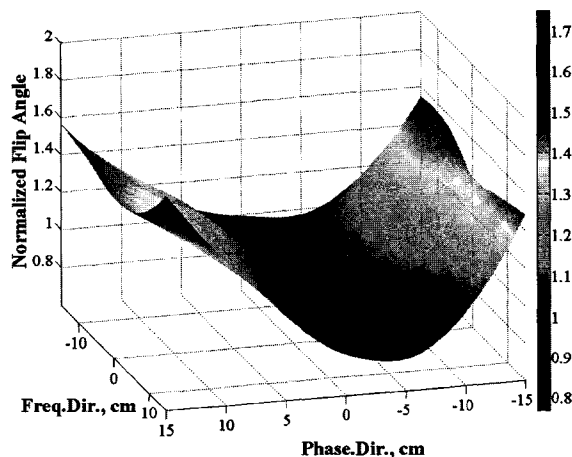
Figure 4.7: B_1 field, or flip angle, map. Since the human body occupies about 90% of the space inside the coil, with the sides almost touching the coil, one expects to see very strong dependence of the flip angle on the position within the coil. The acquired map has the expected distribution. However, it shows a slight assymetry between the sides.

measured at the center of the FOV. The acquired map has the expected distribution. However, it shows slight asymmetry between the sides. These maps were subsequently used to correct the images for the flip angle differences in the different regions in the lungs. The flip angle corrections were done on pixel-by-pixel basis.

4.2.3 RF Pulse

The xenon spectrum in the lungs consists of a gas peak (at 0 ppm) located $\sim$ 200 ppm from several dissolved state peaks, which rise from the xenon dissolved into lung septum, blood plasma and erythrocytes. The frequency spread of the dissolved state peaks is $\sim$ 10 ppm and at 0.2T they are indistinguishable. But the separation in resonance frequencies of the two phases, gaseous and dissolved, is 485Hz.

91

If one is interested in imaging the signal coming from the dissolved phase, one wants to keep the gaseous state intact to have a pool of polarized xenon available to dissolve into the parenchyma. Hence, one wants to have an RF pulse shape such that when it is centered at dissolved state frequency, the spins in gas state "see" very small effect. It is a common practice to use RF pulses that have a shape of a sinc function in the time domain. Then in the frequency domain the pulse has a square shaped profile, and should excite only the frequency range covered by the square. Another pulse shape widely used is the Gaussian shape, which in the frequency domain has the same shape as in the time domain.

Since at 0.2 T field strength the separation is not very wide between the two phases, we needed a pulse shape which in frequency domain has a flat top for a range of over 200Hz, and the frequency range at the bottom is narrower than $2 \times 500 \ Hz$. None of the available RF wave forms qualified, hence we constructed one by taking an inverse Fourier transform of a trapezoidal shape which had 300 Hz wide flat top and 500 Hz bottom. After the implementation the pulse shape was checked with the broadband pick-up coil discussed earlier. The time and frequency domain data of the constructed pulse form are shown in Figure (4.8).

Figure (4.9) shows a comparison of the "trapezoidal" pulse form with a 5 lobe sinc pulse. These data are collected with the broadband pick-up coil. As evident from the picture, "trapezoidal" pulse has a much flatter top, resulting in a more homogeneous flip angle. Also it deposits less energy at the frequencies $\sim \pm 500 \ Hz$ off-resonance.

92
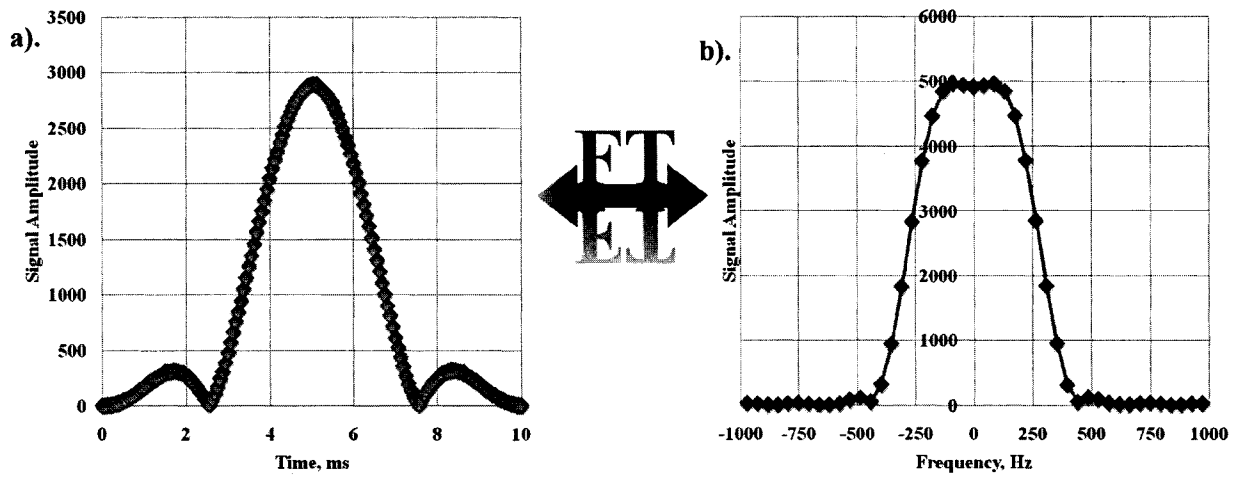
Figure 4.8: RF wave form (time domain) and its Fourier transform (frequency domain). The RF pulse form was designed such that its spectrum in frequency domain has a trapezoidal form with the base spanning over less than 1kHz.
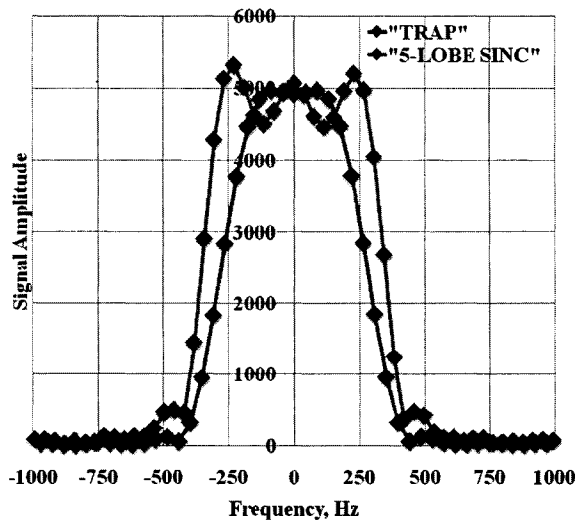
Figure 4.9: Comparison between the pulse form with a trapezoidal spectrum and a commonly used sinc RF form. The spectrum of the "trap" pulse has much flatter top resulting in more homogeneous flip angle over the chosen frequency range compared to that of the 5-lobe sinc pulse presented here.

93

4.3 MRI Compatible Spirometer

In order to study the dependence of the alveolar surface area on the lung gas volume, we needed a lung volume measurement in parallel with the NMR signal acquisition. For this an MRI compatible spirometer was constructed by Mirtech, Inc. An older model rolling-seal spirometer was used where all magnetic pieces of hardware were replaced. The spirometer is interfaced with a LabView program. The NMR pulse sequence is set-up such that it forces a scope trigger at the same time as excites the dissolved state xenon. This scope trigger is recorded by the spirometer, thereby synchronizing spirometer and spectrometer measurements.
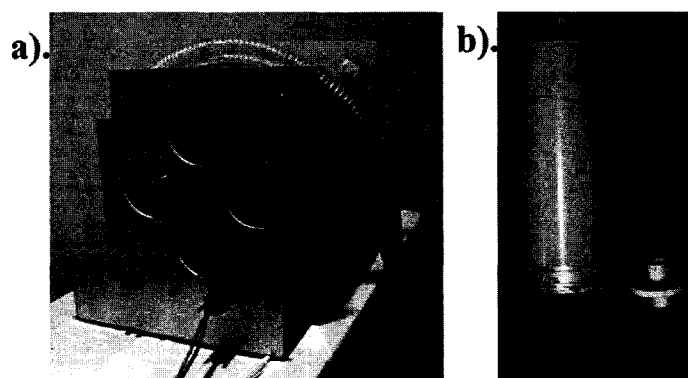
Figure 4.10: MRI compatible spirometer with the calibration syringe. All magnetic components of an old spirometer (a) were replaced to enable its use in the MRI suite. Calibration and linearity check of the spirometer were done using a calibration syringe (b).

Figure (4.10) shows the spirometer (a), the calibration syringe and a mouth piece (b). The small filter with the mouth piece on one side, is connected to the spirometer tube on the other side. The spirometer was measured to have a volume capacity of 10 L. It was calibrated using a 3 Liter calibration syringe provided with the spirometer, and then the

94

calibration was verified using a calibration syringe from the local PFT lab. The numbers from both measurements agreed. Also, using the linearity of the roll was confirmed.

4.4   Human Protocol

Human experiments followed an FDA IND and local IRB approved protocols. According to the initial protocols in 2005, only healthy people from 18 to 65 years old could participate in the studies. In 2006 the new protocols approved the studies with patients with mild to moderate lung diseases.

4.4.1   First Screening

The potential subjects are given a consent form for a review. If interested, they undergo a preliminary screening by a physician. This screening eliminates those candidates, who have a history of allergies, high blood pressure etc. The remaining candidates take a 6-minute walking test with a SpO_2-meter attached to one of their fingers. If the oxygen saturation level drops by more than 5 points from the initial reading, the candidate is automatically eliminated from the studies.

At the next stage the candidate's EKG, blood pressure, heart rate, SpO_2 level and respiration rate are recorded, followed by several practice breaths to simulate the actual experiment. One practice breath includes breathing of air from a set of tedlar bags, containing the maximum amount of xenon, oxygen and air mixture that this subject would ever breathe. The first Xe breath is always supervised by a physician. The breathing protocol consists of two (inhale to TLC)-(exhale to RV) cycles, followed by inhalation of the bags' contents. The subjects are asked to hold their breath for 20 seconds, while the

95

physician monitors their vitals. The candidate's vitals are recorded again after the breath-hold. If heart rate changes by more than 50 points, blood pressure changes by 20 points and SpO_2 drops by more than 5 points, the candidate will be eliminated. Otherwise he/she will proceed to the initial test with polarized xenon.

The Tedlar bags used for the gases are connected through a Y-tube to a plastic line. There are two small plastic valves attached: one is placed right after the xenon bag to prevent the contact of the polarized gas with oxygen, and another one is placed after the Y-tube to keep the gas from escaping from the bag.

The first breath-hold with hyperpolarized xenon is also performed under a physician's supervision. The breathing protocol is exactly the same as with air only, the breath-holds limited to 20 seconds. The subjects are warned to start breathing at any time if they fill uncomfortable, even if the 20 seconds have not passed. The heart rate and oxygen saturation levels are monitored again during this breath-hold. If the heart rate did not increase significantly and the oxygen saturation level did not drop, then the subject qualified to participate in the studies.

4.4.2 The experiments

For all experiments with human subjects a physician had to be present to monitor the vitals of the subject while breathing xenon gas inside the magnet. In 2006, however, a new protocol was approved, according to which for healthy subjects a physician must be present for the initial screening only, then experiments not exceeding 20 second breath-holds could be monitored by a person trained in Advanced Cardiovascular Life Support program. Also, with a presence of a physician during the experiments longer, up to 40 seconds, breath-holds

96

were approved for healthy subjects. The new protocol allowed participation of patients with mild to moderate lung diseases, but only for short breath-holds (under 20 seconds).

The set of the vitals is recorded again 10 minutes after each xenon breath.

4.4.3 Subject information

The xenon gas mixture approved by FDA and IRB must contain no more than 70% of xenon and no less than 21% of oxygen. The xenon concentration in the lungs after inhalation should not exceed 35%.

The maximum amount of xenon that can be given to a subject was determined based on either the actual or predicted values for the lung volumes. The predictions are based on the subjects' age, sex and height and calculated using the formulae presented in Table (4.1). All subjects were sent to the PFT lab for spirometry measurements as well as DL_{CO}

Sex	RV	TLC
$Male$	$1.31\,(0.0254 \cdot H) + 0.0022 \cdot A - 1.23$	$7.99\,(0.0254 \cdot H) - 7.08$
$Female$	$1.81\,(0.0254 \cdot H) + 0.0016 \cdot A - 2$	$6.6\,(0.0254 \cdot H) - 5.79$

Table 4.1: Formulae for lung volume calculations based on sex, age and height.

and FEV_1 measurements. If they were able to get the test results before the studies, their measured lung volumes were used in calculations instead of the predicted values. Table (4.2) provides information about subjects' sex, age and smoking history, Table (4.3) - information about their lung volumes measured at the PFT lab, whereas Table (4.4) has the information about their DL_{CO} and FEV_1 measurements.

Almost 250 xenon breath-holds were done up to date, not including the initial screening. None of the subjects reported any negative reaction to the gas. Xenon showed no effect on

ID	Age	Sex	H	TLC	RV	Notes	Sm.History
HS4	55	male	177.8	7.33	2.34	NS	0
HS6	32	male	177.8	6.2	1.33	NS	1.2
HS13	32	male	188	7.94	1.94	NS	0
HS14	32	male	175.3	7.13	1.78	S	12
HS15	30	female	152.4	4.27	1.24	S	18
HS16	23	female	158.8	4.60	1.25	S	9
HS17	28	female	170.2	5.44	1.53	S	24
HS18	35	female	160	4.77	1.46	S	0
HS19	30	female	158.8	4.94	1.42	S	8
HS20	28	female	154.9	4.44	1.25	NS	0
HS22	25	male	185.4	7.74	1.75	SH	1.5
HS23	23	male	175.9	7.33	1.64	SH	5.5
HS26	50	male	163.2	5.96	2.01	S	33
HS27		female	167.6	5.27	1.91	ILD	−
HS28		female	162.6	4.94	1.85	ILD	−

Table 4.2: Subject information. "SM" - a smoker, "NS" - a non-smoker, "SH" - a person exposed to a second-hand smoke everyday, "ILD" - a subject, who has been disgnosed with ILD. A subject is considered to be a non-smoker if he/she does not have a smoking history of more than 1.5 pack years and is not an active smoker at the time of the participation in the studies.

98

ID	TLC	TLC % pred	FRC	FRC % pred	RV	RV % pred
HS4	7.02	100	3.76	95	1.85	81
HS6	6.2	86	3.45	88	1.33	71
HS13	7.54	93	4.38	98	1.94	89
HS14	6.64	95	3.15	82	1.79	99
HS16	4.11	80	2.03	78	0.82	58
HS17	6.52	109	3.52	112	1.85	103
HS18	4.96	97	2.55	96	1.11	73
HS19	4.54	90	1.97	76	1.01	70
HS20	3.68	77	1.81	75	0.91	69
HS22	7.57	95	4.23	98	1.42	72
HS23	6.05	85	2.25	58	0.74	44
HS26	7.27	125	3.67	115	2.3	127
HS27	4.83	89	1.75	64	1.16	63
HS28	4.8	93	2.4	84	1.83	107

Table 4.3: Lung volumes of the participating subjects measured in the PFT lab.

ID	DL_{CO}	DL_{CO} % pred	FEV_1	FEV_1 % pred
HS4	38.38	139	3.93	115
HS6	26.79	106	4.41	100
HS13	34.72	106	4.86	108
HS16	16.64	74	3.06	103
HS17	29.57	125	4.1	125
HS18	21.24	99	3.09	111
HS19	19.87	90	3.04	106
HS20	20.74	95	2.65	95
HS22	39.65	117	4.96	107
HS23	36.35	110	4.58	105
HS26	24.35	90	3.09	105
HS27	25.19	85	2.86	98
HS28	11.41	45	2.1	74

Table 4.4: DLCO and FEV1 of the participating subjects measured in the PFT lab.

either of the vital signs that were monitored before, during or after the administration of the gas.

4.4.4 Breathing Protocols

We performed experiments at several lung volumes, which were close to either RV, FRC or TLC. They all had very similar breathing protocols, however we will describe each of them separately.

FRC experiments "FRC experiments" refers to experiments performed at lung volumes close to FRC. For this the subjects while already lying on the bed inside the magnet, were asked to inhale to TLC, exhale to RV, repeat this cycle and then inhale the gas mixture from the Tedlar bags. For FRC experiments the bags contain enough xenon, oxygen and air mixture to bring the lung volume of the subject from RV to $RV + V_{mix} \approx 0.45 TLC \approx FRC$. Then they held their breaths at this, near FRC lung volume, while data are collected.

TLC experiments For TLC experiments, the subjects were again asked to go through the TLC-RV cycle while breathing on air, and follow with the gas from the bags. The amount of gas in the bags is calculated based on the subjects lung volumes to bring him/her to TLC. If the amount of gas is miscalculated, the subject is asked to inhale a gulp of air in order to reach TLC, where the experiments are performed. This is the most repeatable lung volume, and our tests with a spirometer showed that it is much easier for the subjects to repeat reaching TLC than RV.

RV experiments For RV experiments the subjects still go through TLC-RV cycle on air, then inhale the gas mixture from the bags, hold just for a couple of seconds and exhale all

101

the way to RV, where they hold their breath. This is the hardest lung volume to reach, and some subjects showed varying RV readings when breathing on the MRI-compatible spirometer. The ability to reach RV depended on the number of full breathing cycles the subject has performed already in the short period of time, i.e. when they tire it is much harder to reach RV. Also, in supine position, which is the position we used for our experiments, it is harder to reach RV. None of the subjects we asked to perform on the MRI compatible spirometer reached their true RV. The closest they went is $RV + 100mL$, while the more common value is at $RV + (250 - 400)mL$.

Mixed experiments There were experiments performed while the lung volume was changing. Initially, before the spirometer was built, to probe the signal dependence on the lung volume we had to design an experiment where the lung volumes changed throughout the experiment, but were constant during some period of time to collect data at that fixed lung volume and proceed to the next. The solution to this was preparing 2 sets of bags, with xenon and oxygen mixtures such that when the subject, after exhaling to RV, inhales from the 1st set of bags, he/she reaches a lung volume near FRC, where he/she holds their breath for a short 6 second breath-hold, then without exhaling the subject is asked to inhale the gas mixture from the 2nd set of bags to reach TLC. If the subject feels that there was not enough gas to reach the highest lung volume, they gulp some air from the room to reach the TLC and hold their breath for another 6 seconds. This is then followed by full expiration to reach RV and another 6 second breath-hold.

This breathing maneuver allowed us to measure the gas exchange in the lungs at three different lung volumes during the same experiment, enabling comparison of the data at

102

these lung volumes. Otherwise a straight comparison of the data from 2 different runs is complicated by any possible changes in the subjects lung function, heart rate, blood flow etc. that could affect the gas exchange in the lungs, but would be extremely hard, if not impossible, to account for.

Experiments with the spirometer And finally, we have performed experiments, during which the lung volume was constantly changing, and not only the NMR signal was recorded, but the lung volume as well. For this type of experiments the subjects were given enough gas mixture to reach the TLC. After going through TLC-RV cycle twice, they inhale the mixture from the bags and if necessary, follow with some more air from the room, drop the bags and start exhaling through the spirometer tube. After they have reached their RV, they are asked to hold their breath at this lung volume for just a second to allow several point to be collected by the spirometer at RV for better registration of the lung volume, and then inhale all the way to TLC, still on the spirometer, and hold at TLC for another second.

Since the TLC is the most repeatable lung volume, we match the TLC reading of the spirometer to the real TLC of the subject and obtain information about the lung volume behavior with time. Using this information together with the NMR signal collected simultaneously with the spirometer data, we deduce the NMR signal versus lung volume information.

103

CHAPTER 5

THE CHEMICAL SHIFT SATURATION RECOVERY TECHNIQUE

The main function of the lungs, the gas exchange, is accomplished through a diffusion process driven by a concentration gradient: after filling the lungs with oxygen-rich air (21% of O_2, 0.04% CO_2), oxygen is diffused into the lung parenchyma, while carbon dioxide from the blood (17% of O_2, 4% CO_2) is driven out into the gas state and exhaled. The *Gas* exchange is a very efficient process since the surface area available for gas exchange is quite large and the gas - blood barrier very thin (see Chapter 1).

Lung diseases decrease the efficiency of this process and may prevent the body from getting enough oxygen. More than 35 million Americans have a chronic lung disease like asthma or *COPD*. If all types of lung disease are lumped together, they are the number 3 killer in the United States, causing 1 in 7 deaths in this country.

In order to determine early impairment of the lung function and prevent its further degradation, it is necessary to understand the structure and function of the lungs. This can be achieved through close study of its morphometric parameters.

5.1   What has already been done?

Historically, a physiological parameter estimating lung function is the pulmonary "diffusing capacity". It was introduced by Bohr [7], and meant a "constant" relating the flow of O_2 from air to blood, $\dot{V}_{O_2}$, to the difference between the oxygen partial pressure in alveoli, P_{O_2}, and the mean oxygen tension in alveolar capillary blood, $\bar{P}_{O_2}$([21], [66])

$$\dot{V}_{O_2} = DL_{O_2} \left(P_{O_2} - \bar{P}_{O_2} \right) \tag{5.1}$$

104

The DL_{O_2} parameter can be regarded as a conductance of the lungs for oxygen and can be estimated from the geometry and the dimensions of the lungs (being the conductor in this analogy). If DL_{O_2} is estimated it would lay a theoretical groundwork for a quantitative structure-function correlation of pulmonary gas exchange. The diffusion capacity can be written as

$$D = K \cdot S \cdot \frac{1}{\tau_h} \tag{5.2}$$

where K is the permeability of the material for O_2, S is the total available surface area, and τ_h is the harmonic mean barrier thickness which is given by

$$\frac{1}{\tau_h} = \frac{1}{n} \sum_{i=1}^{n} \frac{1}{\tau_i} \tag{5.3}$$

It was shown by Weibel and Knight [22] that for a simple case of a flat barrier the relevant mean of the variable barrier thickness with respect to the diffusion is not the arithmetic, but the harmonic mean (Eq.5.3).

Most of the studies performed in this area were carried out on fixed lungs of excised animals. The lungs were fixed either by instillation of fixative into the airways, which reveals the relationship between the tissue and the blood in capillaries but cannot demonstrate the extracellular lining layer on the alveolar surface (5.1, a), or by vascular perfusion, in which case the extracellular lining is preserved but the relationship of capillary blood to tissue barrier cannot be revealed (5.1, b). Hence both fixation techniques were used and data analyzed in order to form a full picture of the structure-function relationship.

For the studies stratified sampling was used: from each lobe of the fixed lungs a slice of about 1 to 2 mm thickness was resected using very sharp razor blade, then sliced into small cubes of 2 to 3 mm^3. From this pool of blocks a small number (4 to 8) of randomly selected

105
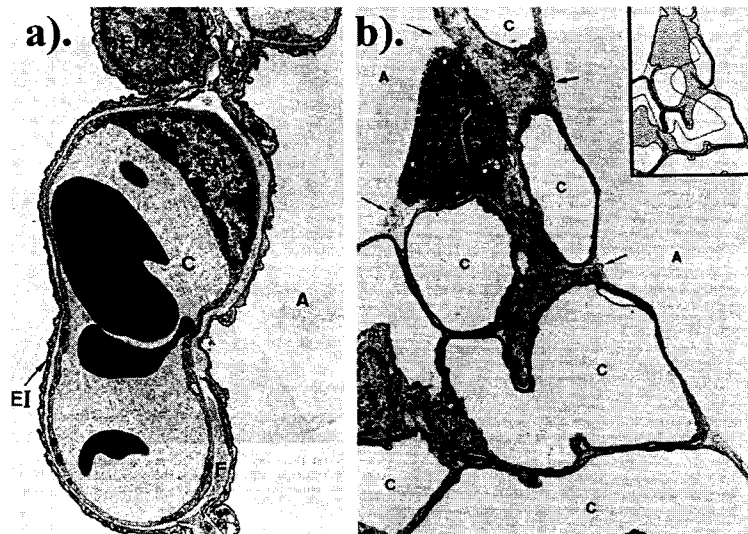
Figure 5.1: Pulmonary tissue and capillaries. [40] "(a). Alveolar capillary, C, lined by endothelial cell, EN. Alveoli, A, are lined by Type I squamous epithelial cell, EI. Left side of the barrier has minimal interstitium with fused basement membranes; in the right half interstitium contains some collagen fibrils, F, and fibroblast processes (7400X). (b). Rat lung fixed by vascular perfusion. Capillaries, C, are empty. A=alveolar space. Arrows point at lining layer pools. Inset shows scheme of reversible folding of connective tissue midplane. Extensive parts of the tissular alveolar surface have been "derecruited" and are not available for gas exchange. The gaps inside the folds are usually filled with lining layer. Note final smoothness of alveolar surface (6700X)."

106

pieces were analyzed. Studies of the gas exchange region in the terrestrial mammals (shrews, bats, mice, rats, guinea pigs, rabbits, monkeys, dogs and man) detected no fundamental qualitative differences in the structure of the gas exchange apparatus. The volume and surface areas were estimated by simple stereological counting methods by comparing the micrograph with an appropriate test size ([19], [20], [23]).

The minimal tissue barrier was measured to be from 0.1 μm to 0.3 μm. The gas-blood barrier thickness can be anywhere from 5 μm or more in the regions where cell organelles, nuclei or interstitial elements are contained [21]. The plasma layer separating the endothelial cell from the Red Blood Cell (RBC) membrane can be a few microns deep.

The studies performed on fixed lungs showed that the alveolar surface area varies depending on the level of lung inflation. This dependence was studied by many groups on different animals using several different techniques to fix the lungs and analyze the data, which made the comparison of the results virtually impossible. The alveolar surface area, S_A, dependence on lung volume, V_A, in humans was studied by Thurlbeck [85] and Weibel [19].Thurlbeck performed his experiments on 25 non-emphysematous lungs of normal subjects ranging in age from 25 to 79 years old. He concluded that alveolar surface area varies between 43 and 102 m^2, depending on the subject's body size. He derived a formula estimating the S_A based on the subject's height, H :

$$S_A = 1.18 \cdot H - 127 \tag{5.4}$$

where H is measured in cm and S_A- in m^2. Thurlbeck found that S_A falls with age.

The same trend was observed by Weibel in 2 human lungs he studied [19]. Figure 5.2 shows the S_A dependence on V_A from these two studies.
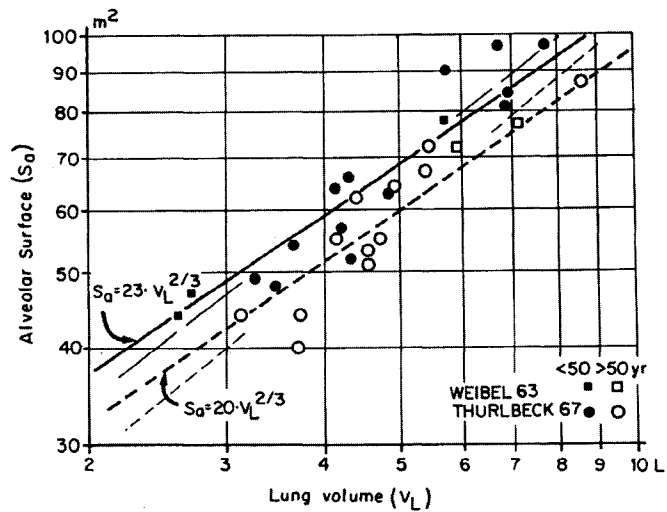
Figure 5.2: Alveolar surface area dependence on the lung volume. [40] "Alveolar surface area S_A plotted against lung volume V_A for two age groups (< 50 and > 50 yr.)".

Another extensive study of the S_A dependence on V_A was done by Gil *et al.* in 1979. These experiments were performed on fixed lungs of 24 excised rabbits filled with either air or saline to lung volumes between 40 and 100%. The major finding of this work was the functional form of S_A dependence on V_A for these two cases of fixed lungs. In particular, they showed that $S_A = k \cdot V_A^{0.33}$ for air filled fixed lungs and $S_A = k \cdot V_A^{0.58}$ for saline filled fixed lungs (see Figure 5.3).Figure (5.4) shows electron micrographs of air and saline filled lungs from this study, where different degrees of capillary bulging are seen in air- and saline-filled lungs. The authors attribute this to profound influence of the interfacial tensions on the structure of alveolar septa and surfaces.

The authors summarize the possible modes by which the air spaces reduce their volume on deflation in the following points: sequential de-recruitment of alveolar surface by collapse of whole units of the lungs, which will affect S_A and V_A the same way, i.e. functional

108
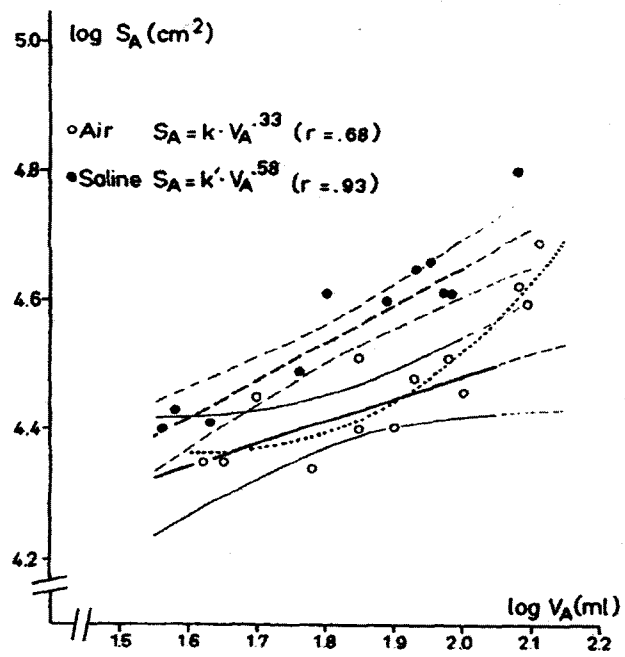
Figure 5.3: Alveolar surface area dependence on the lung volume in fixed rabbit lungs filled with air and saline. [39] "Log-log plot of the alveolar surface area S_A versus volume V_A in air- and saline-filled fixed lungs".

109
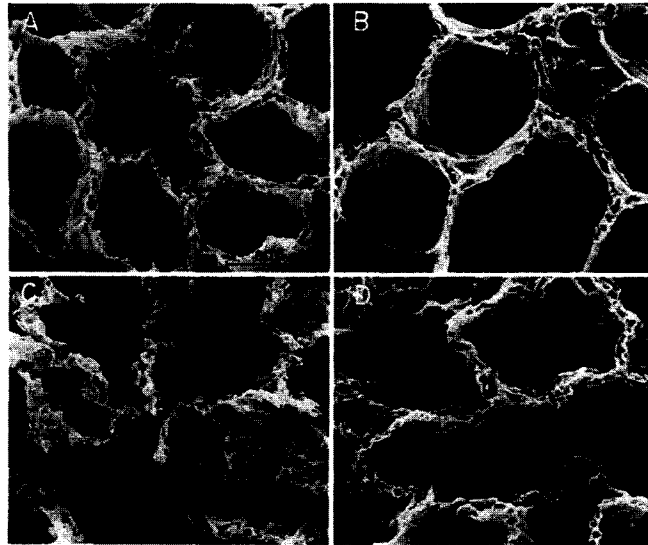
Figure 5.4: "Scanning electron micrograph of air- and saline-filled vascular perfusion fixed lungs". [39] "A and B: air-filled lungs at 40 and 80% of TLC, respectively. C and D: saline-filled lungs at 40 and 80% of TLC, respectively."

dependence would be of the form $S_A \propto V_A^1$; balloon-like reduction of the alveolar size, implying $S_A \propto V_A^{2/3}$; simultaneous change of not only alveolar size, but shape as well (for lower lung volumes, the alveoli have more spherical shape, whereas at higher lung volumes they assume polyhedral shape with slightly smoothed corners) - this kind of shape adjustment will result in functional change from power a of 2/3 to something closer to 1; crumpling of the alveolar surface or anisotropic accordion-like deformations - in such a case the S_A would remain constant with V_A change, i.e. $S_A \propto V_A^0$.

As mentioned earlier, all these studies were performed on fixed lungs, and it has never been shown whether the assumption that these fixations do not alter structure of the lungs actually holds. In this light the possibility of *in vivo* studies would be welcome. With introduction of hyperpolarized ^{129}Xe imaging to medicine this became possible. A method

for the gas exchange dynamics *in vivo* investigations in the lungs, as well as S_A dependence on lung inflation, is described here. The technique is applied to *in vivo* studies in humans for the first time.

5.2   The CSSR technique

The Chemical Shift Saturation Recovery (*CSSR*) method was developed by Butler *et al.* [45] and underwent very careful validation tests performed on porous phantoms, which resemble animal or human lungs in structure. This technique allows determination of the surface-to-volume ratio, S/V, from the exchange dynamics of polarized ^{129}Xe gas from the pores into the solid and back.

In these tests they monitored the exchange of polarized ^{129}Xe from gas state into the dissolved state in a porous polymer granulate (POREX, Atlanta, GA) chosen as a lung model (with respect to the mean pore size). Glass cells were filled with the polymer samples, evacuated the air from the pores of the material and filled the gas space with hyperpolarized xenon. Then the dissolved state was destroyed by an RF pulse applied at the dissolved state frequency f_{diss}, leaving the gas state signal intact. This creates a step function in the dissolved state xenon concentration at time $t = 0$. Then they observed the recovery of the dissolved state xenon signal due to the interphase exchange for times from 10 to 1000ms.

A one dimensional diffusion model was employed for S/V determination for short exchange times. The underlying assumptions were that the density of the dissolved state xenon polarization, $\varrho(x,t)$, satisfies the diffusion equation for $x > 0$, with $\varrho(x, t = 0) = 0$ initial condition, and $\varrho(x = 0, t) = b\varrho_{gas}$, where b is the partition coefficient of xenon and

111

ϱ_{gas} is the density of the gas-state xenon which is assumed to be constant during an interphase exchange measurement (small RF depletion effect and T_1 relaxation effect are neglected). They showed that the number of the dissolved state xenon atoms per unit volume can be expressed as

$$\frac{N_{diss}(t)}{V} = \varrho_{gas} b \frac{S}{V} \sqrt{\frac{4D_{diss}t}{\pi}} \tag{5.5}$$

where S is the total pore-space surface area, D_{diss} is the diffusibility of the dissolved state xenon in the POREX polymers. Using the fact that $\varrho_{gas} = \frac{N_{gas}}{\phi V}$ with ϕ being the porosity of the material and N_{gas} - number of polarized xenon atoms in gas state, Eqn. (5.5) can be rewritten as

$$F(t) = \frac{N_{diss}(t)}{N_{gas}} = \frac{b}{\phi} \frac{S}{V} \sqrt{\frac{4D_{diss}}{\pi}} t = \frac{\int S_{diss}(t,\omega)\, d\omega}{\int S_{gas}(\omega)\, d\omega} \tag{5.6}$$

where the fact that $N_{diss}(t)$ and N_{gas} are proportional to $S_{diss}(t,\omega)$ and $S_{gas}(\omega)$, respectively, was used. Here a quantity $F(t)$, called a fractional diffusive gas transport, was introduced which is the ratio of the measured dissolved and gas state signals.

Samples with 4 different pore sizes were investigated (20, 70, 120 and 250 μm) via 2 different methods: the measurement of S/V with the proposed NMR technique as well as with confocal microscopy. The results from both methods agreed within the measurement error (Figure 5.5). This validated the technique and we applied it in experiments with human subjects to measure alveolar surface area per unit gas volume, S_A/V_A, in vivo.

5.3 Diffusion models

Let us consider the gas exchange in the lungs for very short times, bringing this problem to a one dimensional diffusion problem treated by Butler et al. [45].Figure (5.6, the red
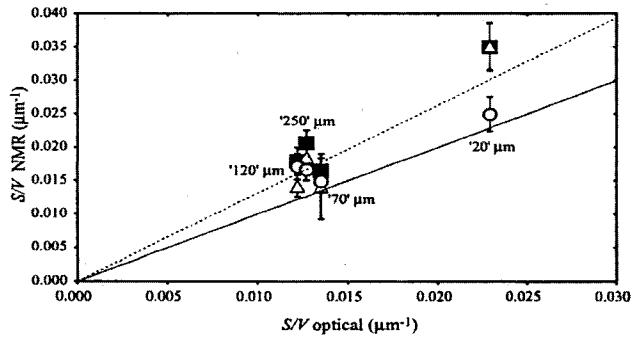
Figure 5.5: Comparison of polimer pore-space S/V obtained with optical microscopy and NMR [45].
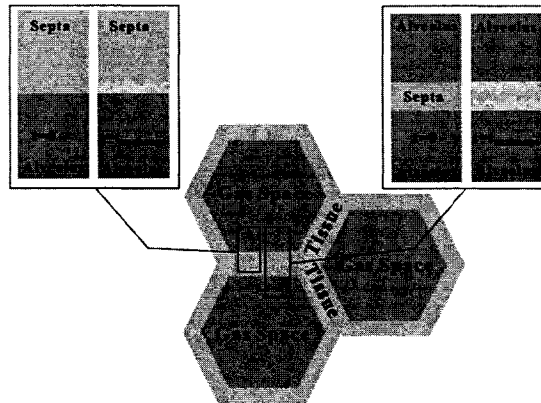
Figure 5.6: Depiction of the one dimensional diffusion models in the lungs. In one case only very short diffusion times (early times model) are considered allowing tissue to be infinetely thick. [45] As time goes on, this assumption is not valid anymore and one has to adjust the diffusion model to include the longer times behavior (late times model), thereby changing the the tissue thickness from semi-finite to finite.

113

quadrangle) shows the idea behind the model, where the lung parenchyma is considered to be infinitely thick. This model is valid for very short exchange times. As mentioned earlier (Eqn.5.6), if we treat gas exchange with this model, the signal from the dissolved state will be proportional to $\sqrt{t_{exchange}}$ with the proportionality constant including $\frac{S}{V}$. In reality, however, the picture is different (Figure 5.6, the green quadrangle) - the septum has a finite width, and signal in the lung tissue saturates and is carried away by the blood. The POREX samples also had a finite width "septum", but it is much thicker than the lung septa and therefore the $\sqrt{t}$ behavior was always valid for the exchange times used. Therefore we will need to treat the problem as a diffusion into a thin slab.

Let us start with a septa of thickness L sandwiched between alveolar gas spaces filled with polarized xenon. Assume that at time $t = 0$ concentration of polarized xenon atoms is zero inside the tissue, and 1 in the gas spaces. We want to solve an equation which would describe the diffusion of the xenon atoms from gas space into the parenchyma (Figure 5.7).
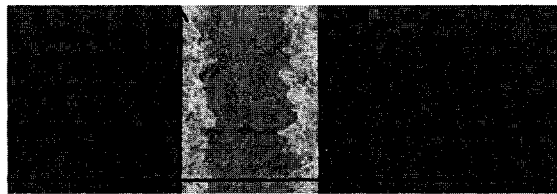
Figure 5.7: Model for 1 dimensional diffusion into a slab. The tissue slab is sandwiched between gas compartments and gas dissolves from both sides.

The equation governing this process is derived from the principle of conservation of the matter, or continuity equation: a change in density in any part of the system is due to

114

inflow or outflow of material, no material is created or destroyed

$$\frac{\partial \varrho}{\partial t} + \nabla \cdot \vec{j} = 0 \tag{5.7}$$

where ϱ is the density of the material and $\vec{j}$ is its flux. If we combine this with the Fick's

1st law stating that the flux is proportional to the negative concentration gradient:

$$j = -D \frac{\partial \varrho}{\partial x}, \tag{5.8}$$

where the proportionality constant D is called the diffusibility, we get the diffusion equation

$$\frac{\partial \varrho}{\partial t} = \nabla \cdot [D(\vec{r}) \nabla \varrho(\vec{r}, t)] \tag{5.9}$$

In the case when D is position-independent we have

$$\frac{\partial \varrho(\vec{r}, t)}{\partial t} = D \nabla^2 \varrho(\vec{r}, t) \tag{5.10}$$

In our case of 1 dimensional diffusion the equation we need to solve can be written as

$$\frac{\partial \varrho(x, t)}{\partial t} = D \nabla^2 \varrho(x, t) \tag{5.11}$$

with the initial condition $\varrho(x, t = 0) = 0$ in $0 < x < L$ and boundary conditions $\varrho(x = 0, t) = \varrho(x = L, t) = 1$. If we assume a solution of the form

$$\varrho(x, t) = 1 - g(x, t) \tag{5.12}$$

and use the separation of variables, i.e. write it as

$$\varrho(x, t) = 1 - u(x) \cdot v(t) \tag{5.13}$$

we can rewrite (5.11) as

$$\frac{1}{v(t)} \frac{dv(t)}{dt} = \frac{D}{u(x)} \frac{d^2 u(x)}{dx^2} \tag{5.14}$$

115

It is noteworthy, that boundary conditions on $g(x,t)$ and consequently $u(x)$ and $v(t)$, are different from those on $\varrho(x,t)$. In particular, the initial condition will be

$$g(x, t = 0) = 1 \ \ for \ 0 < x < L \tag{5.15}$$

and the boundary conditions will read

$$g(x = 0, t) = g(x = L, t) = 0 \ \ for \ t > 0 \tag{5.16}$$

Since the left hand side of Eqn. (5.14) is a function of time only, while the right hand side - of coordinate only, both sides of (5.14) must be equal to the same constant, let say $-\lambda$. Then we obtain that

$$\varrho(x, t) = e^{-\lambda t} u(x) \tag{5.17}$$

and (5.11) becomes

$$-Du" = \lambda u \tag{5.18}$$

The general solution to this equation is

$$u(x) = a \cos(\omega x) + b \sin(\omega x)$$

where $\lambda = D\omega^2$ with $\omega > 0$. It follows from the boundary conditions (5.16) that $a = 0$ and $\omega = \frac{n\pi}{L}$, with n being an integer number. Then we obtain

$$u(x) = b \sin\left(\frac{n\pi}{L}x\right) \tag{5.19}$$

and

$$\lambda = D\left(\frac{n\pi}{L}\right)^2 \tag{5.20}$$

Then we can write the basic solution as

$$g(x, t) = \sum_{n=1}^{\infty} b_n \sin\left(\frac{n\pi}{L}x\right) e^{-D\left(\frac{n\pi}{L}\right)^2 t} \tag{5.21}$$

116

The coefficients of the series will be determined from the initial condition (5.15) which states that at time $t = 0$ there are no polarized xenon atoms in the lung parenchyma, or for $g(x,t)$

$$g(x, t = 0) = \sum_{n=1}^{\infty} b_n \sin\left(\frac{n\pi}{L}x\right) = 1 \tag{5.22}$$

where coefficients b_n are determined from the orthogonality of the Fourier series, i.e.

$$\int_0^L \sum_{n=1}^{\infty} b_n \sin\left(\frac{n\pi}{L}x\right) \sin\left(\frac{k\pi}{L}x\right) dx = \sum_{n=1}^{\infty} b_n \frac{L}{2}\delta_{n,k} = b_k \frac{L}{2} \tag{5.23}$$

On the other hand, from (5.22)

$$\int_0^L \sum_{n=1}^{\infty} b_n \sin\left(\frac{n\pi}{L}x\right) \sin\left(\frac{k\pi}{L}x\right) dx = \int_0^L g(x,0) \sin\left(\frac{k\pi}{L}x\right) dx \tag{5.24}$$

hence giving

$$b_k \frac{L}{2} = -\frac{L}{k\pi} \cdot \left\{ \begin{array}{l} 0, \; if \;\; k = 2n \\[2ex] 2, \; if \;\; k = 2n + 1 \end{array} \right\} \tag{5.25}$$

or

$$b_k = \left\{ \begin{array}{l} 0, \;\; k = 2n \\[1ex] \frac{4}{k\pi}, \;\; k = 2n + 1 \end{array} \right. \tag{5.26}$$

Thus the solution to our diffusion problem will be

$$\varrho(x,t) = 1 - \sum_k \frac{4}{k\pi} \sin\left(\frac{k\pi}{L}x\right) e^{-D\left(\frac{k\pi}{L}\right)^2 t}, \quad k = 2n + 1 \tag{5.27}$$

It follows from Eqn. (5.27), that the total mass of the dissolved xenon at time t is

$$m_{diss}(t) = \int_0^L \varrho(x,t)\, dx = L\left\{ 1 - 2\sum_k \left(\frac{2}{k\pi}\right)^2 \exp\left[-D\left(\frac{k\pi}{L}\right)^2 t\right] \right\} \tag{5.28}$$

Throughout this derivation we assumed that the initial xenon polarization in gas state, C_0, is a unity, as well as the partition coefficient of xenon in tissue, b, was set to 1. If we

117

include them in the formula, then we will have

$$m_{diss}(t) = bLC_0 \left\{ 1 - 2\sum_k \left(\frac{2}{k\pi}\right)^2 \exp\left[-D\left(\frac{k\pi}{L}\right)^2 t\right] \right\} \qquad (5.29)$$

The quantity being measured during the experiments is actually the ratio of dissolved and gaseous phase signals, i.e.

$$F(t) = \frac{m_{diss}(t)}{m_{gas}(t=0)} = b \left\{ 1 - 2\sum_k \left(\frac{2}{k\pi}\right)^2 \exp\left[-D\left(\frac{k\pi}{L}\right)^2 t\right] \right\} \qquad (5.30)$$

One important feature of this method lies in a fact that the same data set yields information about not only the alveolar surface area per unit gas volume but the gas-blood barrier thickness (from long exchange times) as well. Thus this method has a potential of determining early changes in patients with not only tissue-distructive diseases, like emphysema, but tissue scarring diseases as well, such as interstitial pulmonary fibrosis.

5.4 The Experiments

A pulse sequence, very similar to the one implemented by Butler et al, was used in human studies discussed in this chapter. The core pulse sequence was the same in all experiments, with only minor variations, such as adjustment of the exchange times, number of repetitions and such. The flip angles were set as follows: hard pulse interrogating the gas state signal had a 1.4^o flip, while the soft pulse centered on dissolved state frequency was of 90°. For the frequency-selective RF pulse we used a wave form, that has a trapezoidal shape in the frequency domain. The construction and flip angle calibration procedures were discussed in detail in the Experimental Setup.

5.4.1 Pulse sequence

The time diagram of the sequence is presented in figure (5.8). After the subject inhales

the xenon-oxygen gas mixture, a small flip angle hard pulse is applied to measure the gas state signal, which is followed by a frequency-selective 90° RF pulse to quench the dissolved state. Then the accumulation of the dissolved state signal was monitored as a function of the diffusion times, ranging from 17 to 717 ms.
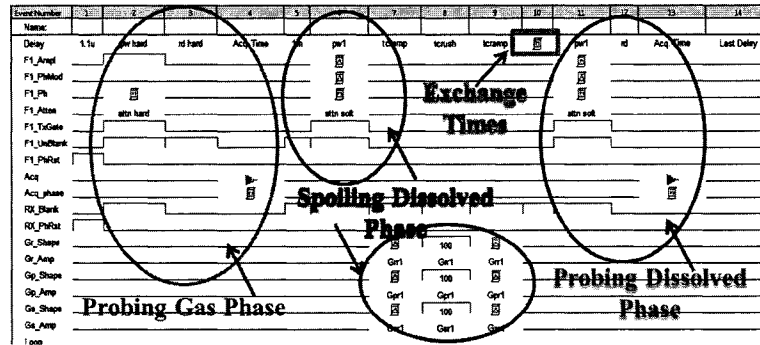
Figure 5.8: The time diagram of the CSSR pulse sequence. First, the gas state is measured by a hard pulse, then the dissolved state is quenched and the signal growth during the exchange time is measured. This figure is the actual pulse sequence from the Tecmag Apollo Console.

A series of experiments were performed on four normal healthy non-smokers, two asymptomatic smokers and two subjects with mild cases of Interstitial Lung Disease (ILD). Since in the case of ILD the alveolar walls of the lungs are inflamed and the lungs stiffen, their tissue thickness is expected to be elevated compare to the normals and TLC declined.

In all experiments the gas inhaling protocols were quite similar - subjects were asked to first establish a breathing history with normal air by inhaling to TLC, exhaling to RV and repeating this. Then they inhale a prepared polarized xenon and oxygen gas mixture from a set of bags and either hold their breath or inhale/exhale in a certain way depending on a

119

type of a measurement being performed. We will discuss each of the protocols separately.

1. Constant lung volume constant exchange time measurements

Constant lung volume constant exchange time (CLVCET) experiments are among the first ones we performed on human subjects. For these runs we prepared 2 sets of Tedlar bags with identical amounts of xenon and oxygen. As soon as the subject exhales to RV the 2nd time, we asked him/her to breathe the gas mixture from the 1st set of the bags and hold his/her breath for 6 seconds while we collect data, then the subject, without exhaling, inhaled the gas mixture from the 2nd set of the bags and, if necessary, followed with room air until TLC was reached. At this lung volume subject was asked to hold breath for another 6 seconds, then exhale all the way down to RV and again hold for 6 seconds. The data acquisition was not interrupted during the breathing maneuvers. The exchange time was kept constant at 62ms throughout the experiment. These runs allowed us to test the stability of the measurement. The data at different lung volumes were initially used to estimate the difference in fractional gas diffusibility with changes in the lung volume.

2. Constant lung volume variable exchange time experiments

The breathing protocol for *Constant lung volume variable exchange time* (CLVVET) experiments is very similar to the one described above with small adjustments: the subject was again asked to repeat the inhale-exhale cycle twice, inhale the gas mixture from the Tedlar bags and hold breath. Only this time the breath hold was not interrupted for about 20 seconds, while data acquisition was in progress. In this series we collected diffusion data for up to 13 different diffusion times, ranging from 17 to 717 ms. The data collected during CLVVET were later fit to both, short time and full time models (diffusion into a slab).

120

3. Variable lung volume constant exchange time experiments

Lastly, we performed experiments with *variable lung volume constant exchange time* (VLVCET), where we asked the subjects to inhale the gas mixture from the bags and, if necessary complement it with some extra air from the room to reach TLC and then exhale through an MRI compatible spirometer all the way down to RV within 6-8 seconds, while we collect both types of data - the NMR signal and the spirometer measurement of the lung volume. This provided us with data to predict the functional dependence of the alveolar functional surface area on the gas volume.

5.4.2 Data Analysis

CLVVET Experiments As mentioned before, in this sequence we probe the gas state signal with a hard pulse of a small flip angle $\alpha_{gas} = 1.4^o$ and spoil the dissolved state signal using a 90° spectrally selective RF pulse, which is followed by dissolved state signal measurement with another soft pulse of $\alpha_{diss} = 90^o$. Since the quantity we are interested in is the ratio of the dissolved phase signal I_{diss} to that of the gaseous phase, I_{gas}, which we call fractional gas transport $F(t)$, we have to account for the aforementioned flip angle differences, i.e.

$$F(t) = \frac{I_{diss}(t)}{I_{gas}(t=0)} \cdot \frac{\sin(\alpha_{gas})}{\sin(\alpha_{diss})} \tag{5.31}$$

which is proportional to $\sqrt{t_{exchange}}$ for short times:

$$F(t_{exchange}) = \frac{b}{\phi} \frac{S_A}{V} \sqrt{\frac{4D_{diss}}{\pi} t_{exchange}} \tag{5.32}$$

Hence if we determine what times can be considered short and for those times measure fractional gas transport, we will be able to deduce the surface area dependence on lung

121

volume. It needs to be noted that V in the Eqn. (5.6) is the total Euclidian volume, while b is the partition coefficient of xenon for tissue and ϕ is the porosity of the lungs, which is defined as the volume of the air space in the lungs, i.e. $\phi = \frac{V_A}{V}$ which results in

$$F\left(t_{exchange}\right) = b \frac{S_A}{V_A} \sqrt{\frac{4 D_{diss}}{\pi} t_{exchange}} \tag{5.33}$$

with S_A being the alveolar surface area and V_A - the alveolar gas volume.

The data from CLVVET experiments were fit to both diffusion models, the one dimensional diffusion into a infinitely thick tissue, which is valid for early times only, and diffusion into a tissue slab for the full range of times. Using only the first 4 terms of the sum in the slab model proved sufficient for the fit - adding any more terms didn't improve fit statistics significantly:

$$F\left(t\right) = c \left\{ 1 - 2 \sum_{n=1}^{4} \left(\frac{2}{n\pi}\right)^2 \exp\left[-D_{diss}\left(\frac{n\pi}{L}\right)^2 t\right] \right\}, \tag{5.34}$$

where c and L are the fitting parameters, and xenon diffusion in tissue was assumed to be $D_{diss} = 3.3 \times 10^{-6} \; cm^2/s$, the value predicted by Ruppert et al. [49]. Here $c = const \cdot b$, with b being xenon partition coefficient for tissue and L is the septal thickness. The fitting was done in Excel using a non-linear least squares algorithm. The function in its original form, however, did not fit the data well until an introduction of a DC offset, F_o, to the equation:

$$F\left(t\right) = F_o + c \left\{ 1 - 2 \sum_{n=1}^{4} \left(\frac{2}{n\pi}\right)^2 \exp\left[-D_{diss}\left(\frac{n\pi}{L}\right)^2 t\right] \right\}. \tag{5.35}$$

This new function fit the data very closely. The possible interpretations of this parameter F_o will be discussed later in this chapter.

VLVCET experiments As mentioned earlier, VLVCET experiments were performed using short diffusion times ($t_{exchange} = 62.1\ ms$) to ensure a linear dependence of $F(t)$ on the $\sqrt{t}$ (a reminder: we are measuring $F(t)$ which is the signal from the dissolved state per signal in the gaseous state.) Then the measured $F(t)$ is linearly proportional to $\frac{S_A}{V_A}$ (Eqn.(5.33)):

$$\frac{S}{V} = \frac{F(t_{exchange})}{b\sqrt{\frac{4D_{diss}}{\pi}t_{exchange}}}.$$
(5.36)

Since in these experiments we measured the lung volume (with the spirometer) along with the collection of the NMR data, we can plot $F(t)$ vs. V. Based on the previously reported functional forms ([85] and [39]) we fit the data to a power function $y(x) = ax^{\beta}$ or:

$$\frac{S}{V} = aV^{\beta}$$
(5.37)

In order to compare the data from different subjects, the measured values should be normalized to a quantity specific to each subject. We chose that quantity to be their TLC, since it is the most stable and repeatable lung volume for a given subject and is strongly correlated with subject's size. Hence, we plotted $F(t)$ vs. $\frac{V}{TLC}$ for each subject.

We also used this data to estimate the actual surface area itself:

$$S_A = V_A \frac{F(t_{exchange})}{b\sqrt{\frac{4D_{diss}}{\pi}t_{exchange}}}.$$
(5.38)

and plotted the surface area and the lung volume data from each subject normalized to his/her TLC: $\frac{S}{TLC}$ vs. $\frac{V}{TLC}$.

5.4.3 Results

123

CLVVET Experiments - Fit to the diffusion models Figure (5.9) shows a sample data set

from the CLVVET experiments. The data are fit with semi-finite tissue thickness model

which is valid for short times and will help to differentiate between short and long time

scales. As apparent from the graphs, the diffusion is well described by the early diffusion

model for exchange times upto ~ 120 ms, after which the fitting curve deviates from the

data points.
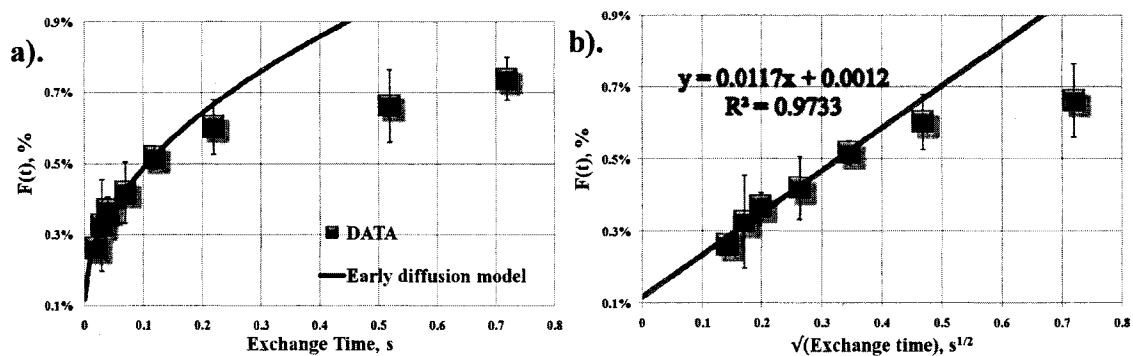
Figure 5.9: The fit of the data set from a healthy normal subject at TLC to the early time

diffusion model. Evidently, the fit is good for short times (up to 120 ms), after which it

deviated from the data. These experiments helped to differentiate between early and late

diffusion. (a) shows the fractional gas transport and the fit plotted against the exchange

time, while (b) has the $F(t_{exchange})$ versus $\sqrt{t_{exchange}}$.

This point of separation between early and late diffusion is the same for all subjects,

and shows no correlation with lung volume.

These type of experiments were performed with 4 healthy non-smokers, 2 asymptomatic

smokers as well as 2 patients with mild ILD. The data from each subject were fit to both,

the early and full diffusion models. At short times, (< 100 ms) both models agree very

124

well with the data and with each other. From the short-time diffusion data we extract
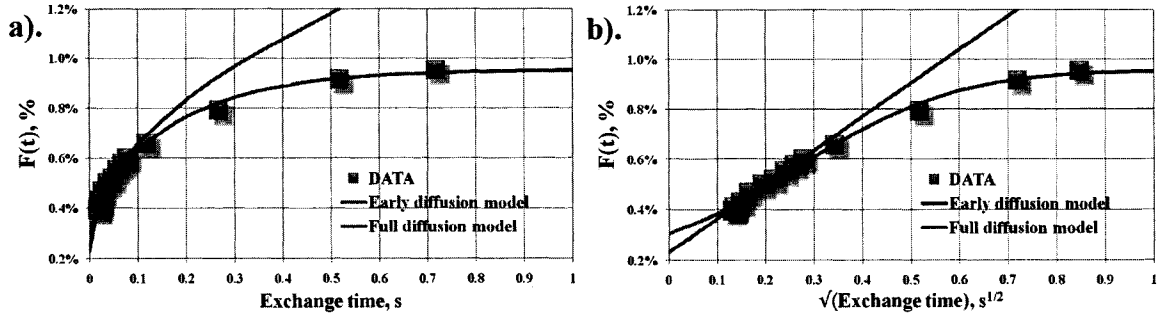
Figure 5.10: The comparison of the early and full diffusion models. (a) displays fractional gas transport $F(t)$ vs. exchange time, while (b) shows the same $F(t)$ vs. $\sqrt{t_{exchange}}$. The data here is from a subject who has a mild case of ILD. The experiment is performed at the current TLC of the subject. For early times both models closely agree.

information about the alveolar surface area of the subject's lungs, whereas the diffusion-into-a-slab model provides not only the surface area, but the septal thickness as well. Table (5.1) contains average of the estimated values for the tissue thickness and surface area from healthy non-smokers, asymptomatic smokers and patients with mild ILD.

As evident from the table, no significant difference in the measured thickness between smokers and non-smokers was observed, while ILD patients data is consistent with slightly thicker septa.

However, the estimated surface area is always lower than the values predicted by Eqn. (5.4). The possible explanation for this effect might be the fact that the first measurement we take is at the exchange time of $t_{exchange} = 17\ ms$, which is long enough time for xenon to travel $\sim 2.5 - 3\ \mu m$. In that case, some of the surface area, which is much thinner than the distance the xenon molecule will travel by the time of our first measurement, is already

125

Subject	Thickness,μm	$S_{predicted}$, m^2	$S_{measured}$, m^2
$HS4$	20.17 ± 1.50	82.8	36
$HS6$	20.13 ± 3.72	82.8	55
$HS13$	20.57 ± 1.83	94.84	55
$HS14$	19.08 ± 3.99	79.84	50
$HS15$	17.80 ± 1.31	52.83	29
$HS27$	24.25 ± 1.30	70.77	8
$HS28$	26.85 ± 4.12	64.82	12

Table 5.1: Average septal thickness, predicted and measured alveolar surface areas for healthy non-smokers (HS4, 6, 13), asymtomatic smokers (HS14 and 15) and patients with ILD(HS27 and 28). These values are obtained from the fits of the data to both diffusion models - for early and late times.

saturated. This then "divides" the septum into "thin" and "thick" parts. The former is not associated with the capillaries and saturates before our measurements start; the latter includes the capillaries, and the diffusion dynamics of xenon into this portion we studied. This separation into portions also implies that we are measuring not the "geometric" or morphological surface area, but rather a "functional" surface area, which is involved in gas exchange.

The thin tissue saturation argument explains the necessity to introduce a constant offset term in the Eqn. (5.35), which is an estimate of the amount of tissue mass that is already filled with xenon.

CLVCET experiments Based on the experiments with variable exchange time we chose $t_{exchange} = 62\ ms$ for the exchange time in CLVCET experiments, as well as VLVCET experiments. As described above, in CLVCET experiments we measured the fractional gas transport $F(t_{exchange})$ for about $6s$ for 3 different lung volumes - RV, FRC and TLC. A sample set of results is presented in Figure (5.11). We performed these experiments with several subjects and found the ratio to be $\frac{F_{RV}}{F_{TLC}} = 3.98$ for changes in the lung volume from RV to TLC, which is of order of $4 - 4.5\ L$. This implies that the surface area does not change significantly with the lung volume, rather it behaves like crumpled paper, which unfolds as the volume increases. However, this is in disagreement with earlier measurements done by Gil et al. [39], that we discussed earlier in the chapter.

VLVCET experiments In order to study this discrepancy more extensively we acquired the NMR data on the subjects while they exhaled into the spirometer. The results are

127
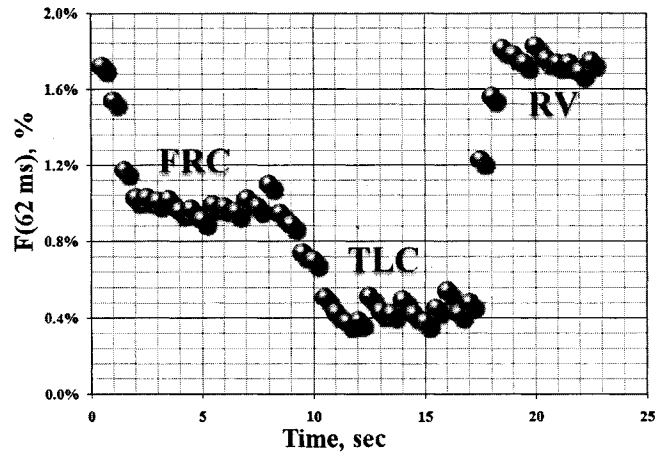
Figure 5.11: The fractional gas transport measured at three different lung volumes in one experiment. The data is from a healthy normal subject, eachange time is set to 62 ms. The three lung volumes are FRC, TLC and RV.

presented in Figure (5.13) while Figure (5.12) shows the data from the spirometer.

The data sets from these experiments are shown in Figure (5.13). It is evident that there is a good agreement between different subjects. As mentioned earlier, the data were fit to a power function of the form $y(x) = ax^\beta$.

The average values of the parameters extracted from the fit of each set are $a = 0.0032 \pm 0.0008$, $\beta = -1.6621 \pm 0.1863$.

On the other hand, for short times the measured signal, $F(t_{exchange})$, is proportional to $\frac{S}{V}$ with the proportionality constant $b\sqrt{\frac{4Dt_{exchange}}{\pi}}$,where b is the partition coefficient and D is the diffusibility of xenon in tissue. Using numbers for the constants from the literature ($b = 0.1$ and $D = 3.3 \times 10^{-6}$ cm^2/s [49]) and exchange time used in the experiments ($t_{exchange} = 62$ ms), as well as lung volumes measured with the spirometer, we obtained estimates of alveolar surface area for the subjects as a function of the gas volume. Figure

128
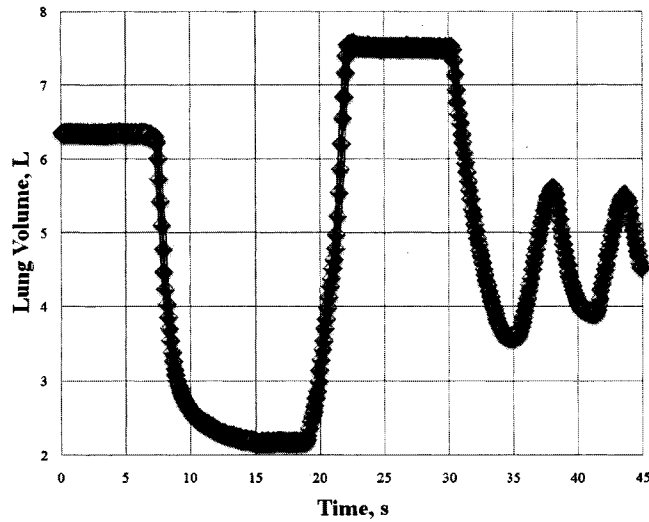
Figure 5.12: A sample data set collected from the spirometer. As the subject exhales through the spirometer, the change in the volume is recorded.
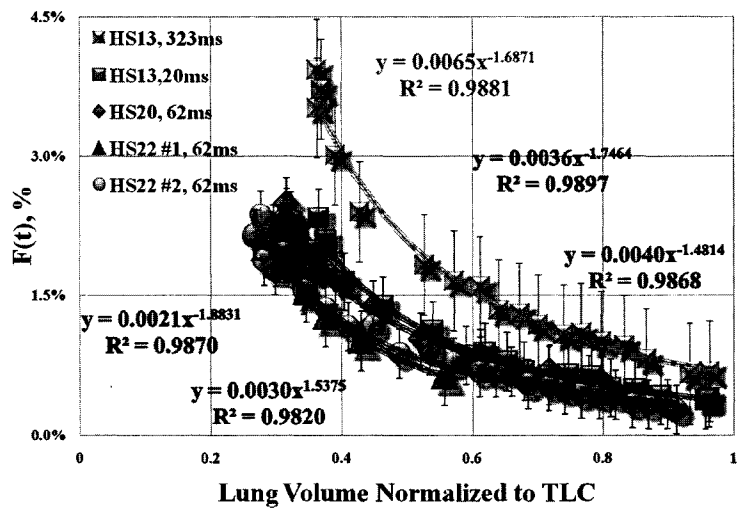
Figure 5.13: The fractional gas excange as a function of normalized lung volume. The fractional gas exchange is proportional to the alveolar surface area per unit gas volume, S_A/V_A. From these data it follows that surface are decreases as the volume increases.

129

(5.14) depicts this relation. In this fit we make an assumption that fractional gas transport is zero at time $t = 0$, i.e. $F(0) = 0$. Here the surface area is plotted versus the lung volume; both axes are normalized to the subject's TLC. This will allow comparison of the data obtained from different subjects.
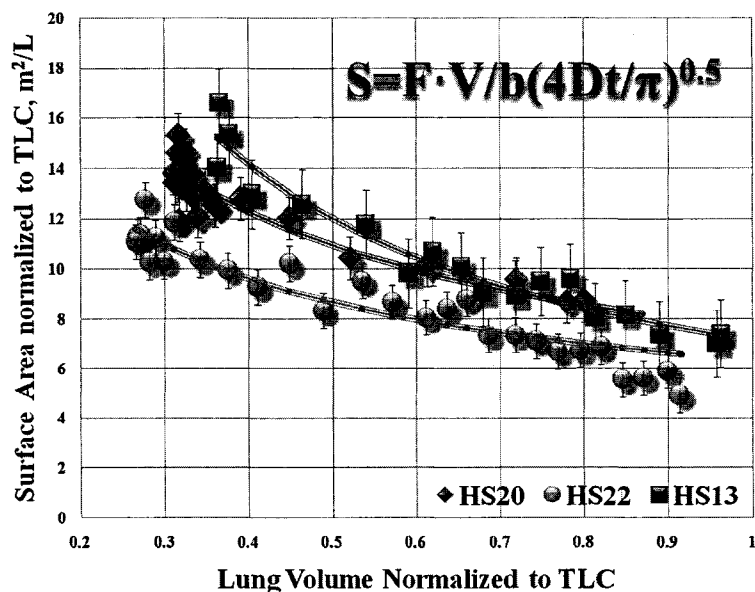
Figure 5.14: Alveolar surface area normalized to each subject's TLC, in m^2/L, as a function of the normalized to TLC lung volume. The lung volume from different subjects is normalized to their TLC allowing comparison of their data. To obtain the values for the surface area we used partition coefficient of 0.1 and diffusibility of 3.3×10^{-6} cm^2/s.

5.5 Discussion of the results

We employed hyperpolarized xenon gas to observe the diffusion dynamics driving the gas exchange *in vivo*. This is accomplished by exploiting xenon's sensitivity to its neighboring environment. We used two diffusion regimes, one for very short times, where pulmonary

130

septum can be considered infinitely thick, and the other for a full range of times, when diffusion into a tissue slab is considered. Both models fit the data very well. However, extrapolation of the measured fractional gas transport F to $t = 0$ ms results in a small offset, whereas one would expect the curve to intercept the ordinate at zero. A number of factors could produce such an effect, including the human error in choosing a range of integration of the signal peaks, etc. But one of the major contributions comes from the fact that the model generalizes the diffusion picture by assuming a uniform medium where the gas propagates. However, strictly speaking, one has to consider individual shapes of the gas-blood boundary. On this level, the diffusion over short times t will progress differently depending on the local morphology. Figure (5.15) shows an electron micrograph of an alveolar wall. It is evident from the picture that alveolar wall thickness is not uniform, and capillaries
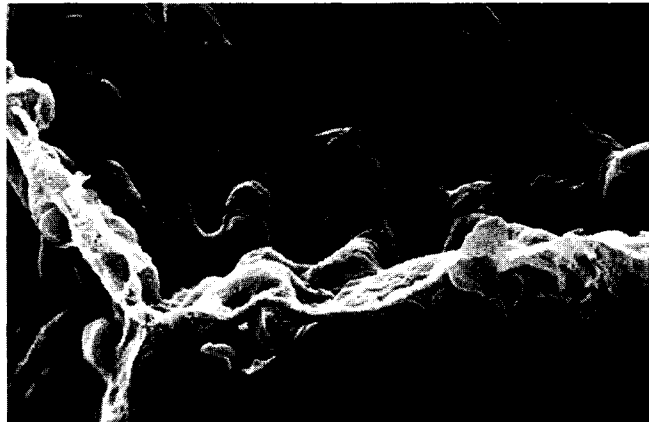
Figure 5.15: An electron micrograph of an alveolar wall [27]. It is evident that the alveolar wall thickness is far from uniform, with the capilaries bulging out from the wall.

are bulging away from the wall. The same type of a geometry can be seen in Figure (5.1, b) where one can see that the wall thickness between alveoli is not uniform at all. If this

is the case, then the thinner parts will saturate much earlier than the thicker ones. Then our diffusion model will not describe the xenon atoms behavior properly anymore, since we will have two separate components of the diffusion process. It should be stressed again that our measurements are not sensitive to these thin parts. The reason for this being that the shortest exchange time we used was 17 ms, during which a dissolved xenon will travel about 2.5 μm, whereas the thickness of the thin part of the septum is estimated to be < 1 μm. This means that some parts of the parenchyma are already saturated by the time we take the first measurement.

This effect could also resolve the discrepancy between our observation of the alveolar surface area dependence on lung volume and earlier reported studies. If we are not sensitive to the first several microns of the tissue, then we will not be able to detect whether it is stretching with the increasing lung volume, as required by the mechanical stability of the system. What could be happening is that as we go to the higher lung volumes, more of the thicker parts stretch and become thinner and invisible to us.

The difference could also come from the difference in the techniques. All previous measurements were performed on fixed lungs ([85], [39]), while our measurements are done *in vivo*.

The absolute values for the alveolar surface area measured are below the predicted by a factor of $2 - 2.5$. This also could be explained by the same argument as above. Another contributor could be the difference in techniques: the formula (5.4) is an empirical description deduced from the histological data. In these cases only the alveolar space is considered, whereas our measurements are done in vivo and we measure exchange happening not only in the alveoli, but the respiratory bronchioles as well. Since the surface area available for

132

the gas exchange in the bronchioles is much smaller than that in the alveoli, this will reduce

the measured mean fractional gas exchange and the mean surface area along with it.

The studies of alveolar surface area dependence on the lung volume were based on

an estimate of the surface area from one time point measurement. This will result in a

underestimated value for $\frac{S_A}{V_{Gas}}$. This effect rises from the DC F_0 offset (Fig.5.16), present
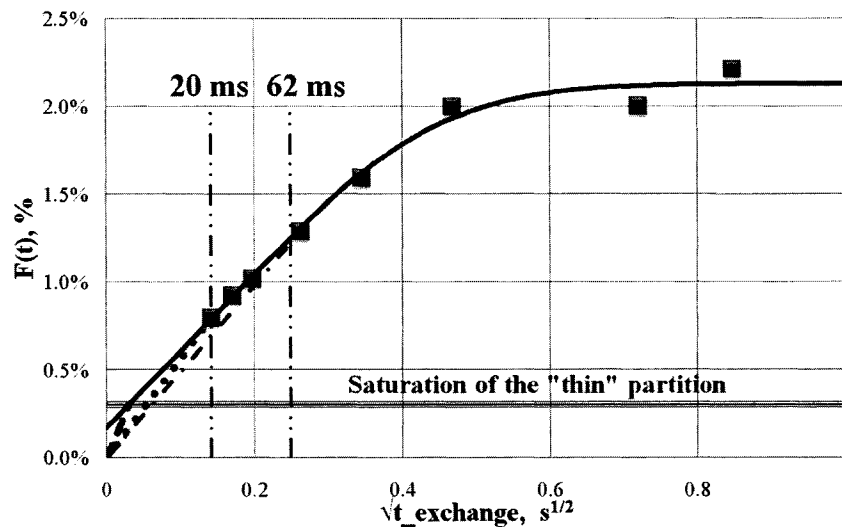
Figure 5.16: The difference between measured and "true" $\frac{S_A}{V_{Gas}}$.The slope of the red line

represents the "true" morphological surface area of the septal surface. However, since the

"thin" portions of the parenchyma will saturate before the first measured time point (tan

horizontal line in the figure), a single time point measurement of the slope from $t = 0$

(green dash-dot line for $t_{exchange} = 62$ ms and pink dotted line for $t_{exchange} = 20$ ms) will

underestimate the slope and hence the surface area.

in the fit for $F(t)$. As mentioned before, the presence of this offset is explained by the

first exchange time used in the measurements. In Figure 5.16 the dashed red line is meant

to schematically demonstrate what one might observe if one could measure at very short

133

exchange times. The slope of the red line represents the "true" morphological surface area of the septal surface. However, since the "thin" portions of the parenchyma will saturate before the first measured time point (tan horizontal line in the figure), a single time point measurement of the slope from $t = 0$ (green dash-dot line for $t_{exchange} = 62\ ms$ and pink dotted line for $t_{exchange} = 20\ ms$) will underestimate the slope and hence the surface area.

For the resolution of these discrepancies measurements should be performed at higher magnetic fields, where one could employ much shorter exchange times and measure not "functional", but rather "morphological" surface area.

134

CHAPTER 6

THE XTC TECHNIQUE

6.1 Earlier Studies

The Xenon polarization Transfer Contrast (XTC) technique capable of measuring "gas exchange "in the lungs was originally developed by Ruppert *et al.* [?]. In their first study [?] Ruppert *et al.* used a rather an elegant way of measuring the gas exchange in the lungs. Since the SNR in the dissolved state signal is quite low, hampering direct measurements
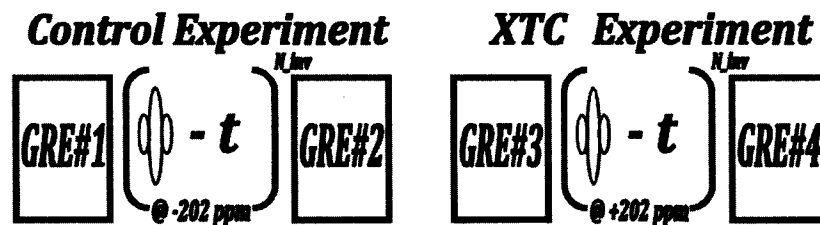
Figure 6.1: A schematic of the original XTC technique developed by Ruppert *et al.* [49] This version of the XTC technique consists of 2 experiments: XTC and Control. Then, based on 2 pairs of images, fractional depolarization per pulse is calculated.

of S_A/V_{Gas} distribution in 2D, Ruppert *et al.* measured the gas signal before and after several consecutive applications of selective $\pi/2$ pulses at the dissolved state frequency f_{diss} 200 *ppm* away from the gas frequency f_{gas}, separated by time $\tau_{exchage}$, allowing for diffusion to take place between the RF pulses (Figure 6.1). Then the loss in the measured signal has several sources: RF depletion, T_1 relaxation of the xenon in the lungs due to oxygen presence, diffusion of gas from alveolar volume into the septal tissue and transport

135

by blood. In order to separate the contribution of the gas exchange from the rest, Ruppert *et al.* performed another "*Control*" experiment, where they again collected two images before and after spoiling soft pulses, but this time the $\pi/2$ pulses were applied at $-200\ ppm$, which does not disturb the dissolved state xenon. The selective RF pulses on the dissolved phase may have a small effect on the gas phase. Therefore by putting them on the opposite side of the gas phase this effect can also be measured in "*Control*" images. Since the rest of the experimental parameters are identical to those in the *XTC* experiment, the data from control experiment can be used to correct for the changes in the signal due to the RF excitation, T_1 relaxation and transport by blood. Using the results from this pair of experiments they calculated the fractional depolarization of the gas per pulse,

$$f_{depol}^{\pi/2} = 1 - \sqrt[N_{\pi/2}]{\frac{S_{XTC,after}/S_{XTC,before}}{S_{Control,after}/S_{Control,before}}} \tag{6.1}$$

where $N_{\pi/2}$ is the number of the spoiling RF pulses. The initial spectroscopic experiments were performed on anesthetized and intubated supine dogs, where interpulse delay was varied between 0.5 ms and 200 ms in order to obtain gas depolarization dependence on the interpulse delay. These experiments showed that $f_{depol}^{\pi/2}$ increases rapidly for exchange times shorter than 50 ms, after which it reaches an asymptotic value of 1.5 % for long delays. For the imaging studies a 100 ms interpulse delay was chosen and Ruppert *et al.* [50] showed that in a supine dog an average depolarization was 1.4 %.

In 2004 Ruppert *et al.* advanced these studies further [49]. This time they considered a one-dimensional model of gas diffusion across the parenchyma to predict the time course of xenon magnetization following the tagging of the atoms in the dissolved state. The

136

macroscopic behavior of the xenon atoms is governed by Fick's second law of diffusion:

$$\frac{\partial}{\partial t}C_m(x,t) = D_m\frac{\partial^2}{\partial x^2}C_m(x,t) \tag{6.2}$$

where C_m is the xenon concentration in the membrane as a function of position x and time t. For a septal wall of thickness L positioned at $x = 0$ the boundary conditions are

$$C_m(0,t) = C_m(L,t) = \lambda C_A \tag{6.3}$$

where λ is the solubility coefficient for xenon in lung tissue and C_A is the concentration of xenon atoms in the alveolar gas space. If at time $t = 0$ an inversion pulse is applied at dissolved state frequency then the initial conditions following a π-pulse are

$$C_m(x,0) = -\lambda C_A \tag{6.4}$$

Ruppert et al showed that the solution to (6.2) with boundary conditions (6.3) and initial conditions (6.4) is

$$C_m(x,t) = \lambda C_A - \sum_{n=1}^{\infty}\frac{8\lambda C_A}{(2n-1)\pi}\cdot\sin\frac{(2n-1)\pi x}{L}\cdot e^{-D_m([2n-1]\pi/L)^2 t} \tag{6.5}$$

where D_m is the xenon diffusion constant in lung parenchyma. Then by integrating Eqn. (6.5) they calculated the signal originating from the xenon atoms dissolved into the septa (S_m):

$$S_m(t) \propto \int_0^{\infty}C_m(x,t)dx = \lambda C_A L - \sum_{n=1}^{\infty}\frac{16\lambda C_A L}{[(2n-1)\pi]^2}\cdot e^{-D_m([2n-1]\pi/L)^2 t} \tag{6.6}$$

137

Since the T_1 is much longer than the exchange time scale, its contribution in this calculation is negligible and ^{129}Xe polarization is constant in the system, i.e. the polarization of the xenon atoms in the gas state plus polarization of the atoms of xenon dissolved into the membrane is conserved. Hence,

$$S_A(t) = S_A(0) + [S_m(0) - S_m(t)]$$ (6.7)

or

$$\frac{S_A(t)}{S_A(0)} = 1 - \frac{S_m(0) - S_m(t)}{S_A(0)} = 1 - f_{depol}^{\pi}(t)$$ (6.8)

where S_A is the gas phase signal and f_{depol} is the fractional depolarization of the gas due to the inversion of the dissolved state signal and subsequent diffusion into the membrane.

In this round the experiments were performed on anesthetized and intubated supine rabbits, a wart dog and a dog. Ruppert *et al.* found $T_1 \approx 30$ *s* in the lungs independent of the exchange time. The data from the spectroscopic runs was fitted to an exponential function of the form $A_0 + A_1 (1 - \exp[-t/B])$. Then the result of this fit was matched to the 1D gas exchange model. By assuming an average septal wall thickness of 5.5 μm they predicted a xenon diffusion constant in lung parenchyma: $D_m = 3.3 \cdot 10^{-6}$ cm^2/s, and measured an asymptotic value of $f_{depol} = 4.5$ %. Note that in this set of experiments fractional gas depolarization is twice that of the previous set of experiments, since in this case Ruppert *et al.* used inversion pulses rather than spoiling RF pulses at ± 202 *ppm* frequency, hence doubling the effect measured on the gas state signal. Ruppert *et al.* also investigated the dependence of the depolarization on the lung inflation - they found that fractional depolarization dropped as the lung volume increased.

138

6.2 Experiments

As shown by Ruppert *et al.*, the registration between images acquired in the two separate experiments works well for anesthetized animals. For breath-hold experiments in humans, however, this might raise some complications. Although a number of techniques have been developed ([52], [47], [51]) and are being improved for image registration, avoiding this issue altogether will decrease the ambiguity of the measurements. We have modified the XTC technique to allow both experiments to be performed in a single breath-hold.

6.2.1 Single-breath XTC

In a single-breath variation of XTC we collect three gradient echo images, called *Gas*, *Control* and XTC images, during a single short breath-hold. The schematic of the sequence is presented in Figure (6.2). Since the subjects participating in the study have limited time and the availability of the polarized gas is limited to about 1 Liter per hour, we could only afford one breath-hold per hour. This limited our imaging resolution - we collected projection images rather than several slices, i.e. each pixel in the images represents a total gas signal from the whole thickness of the lung at that point. We collected 64

Figure 6.2: A schematic of the single breath XTC technique. Here we collect 3 gradient echo images separated by N_inv consecutive inversion pulses exchange time t apart. Then fractional gas transport can be calculated from the data of these 3 images.

139

read-out points with the spectral width of ± 3 kHz and 32 phase encoding lines, with $FOV = 300$ mm in both directions. $k - space$ was collected with shifted echoes, such that echo center was at 0.125 of the acquisition time. This resulted in TE of 8.8 ms and TR of 24 ms. The actual images were separated by 2.73 s and inversion RF pulses were $t_{exch} = 62.1$ ms apart. The entire sequence takes just under 8 s to run, and the hardware requires additional 4 s to compile the sequence before each run. In all XTC experiments we used the RF pulse form with a trapezoidal spectrum (see Figure 4.8), that has been discussed earlier. If a 10 ms long RF pulse is applied at ± 200 ppm, the gas state is tipped with a flip angle smaller than 0.5^o.

The choice of the exchange time was based on $CSSR$ experiments discussed in the previous chapter (see Figure 5.9). According to these experiments, the dynamic equilibrium in the lungs is not reached until ~ 120 ms, and at 62 ms we measure the so called "functional" surface area available for the gas exchange. As discussed in the $CSSR$ chapter, the thin part of the septa is already saturated within the first 17 ms, and in order to measure the geometric surface area, one would need to use exchange times of the order of a millisecond.

Since the polarization of the gaseous xenon decays as we fill the $k - space$, if we use the same flip angle in all 3 images, the Gas image will have the highest SNR, and the XTC - the lowest. In order to obtain images with about the same SNR we will need to use variable flip angles. To predict the optimal flip angle we simulated the magnetization behavior for the experiment. In order to calibrate the sequence properly, we chose to have the same flip angle in the first two images and a higher one in the XTC image. In the simulation we assumed a relaxation time $T_1 = 20$ s, and that 2 % of the gas atoms diffuse into the parenchyma. The resulting flip angles were 3°, 3° and 9° for Gas, $Control$ and

140

XTC images, respectively.

6.2.2 Data Analysis

As Ruppert *et al.* noted [50], [49], in addition to the magnetization loss due to diffusive gas transport, both RF depletion and oxygen presence accelerate the decay. For the image intensities in the single-breath XTC experiment one can write

$$S_{Control} = S_{Gas} \cdot R_{T_1}^{Control} \cdot R_{RF}^{Control}, \qquad (6.9)$$

$$S_{XTC} = S_{Control} \cdot R_{T_1}^{XTC} \cdot R_{RF}^{XTC} \cdot R_{Depol},$$

where S_{Gas}, $S_{Control}$ and S_{XTC} are the intensities of the signals in a pixel of the 1st (Gas), 2nd $(Control)$ and 3rd (XTC) images, respectively; $R_{T_1}^{Control}$ and $R_{T_1}^{XTC}$ are the contributions of the T_1 decay of the gas signal during the time between collection of the centers of the Gas and $Control$ images, and of the $Control$ and XTC ones, respectively. $R_{RF}^{Control}$ and R_{RF}^{XTC} are the contributions of the RF pulses to the gas signal decay, and R_{Depol} is the amount of the decay due to magnetization inversion of xenon dissolved into the alveolar walls. Since timing of the images and times allowed for the exchange between gas and dissolved states were kept constant, T_1 contribution to the decay will be the same between Gas–$Control$ and $Control$–XTC image pairs assuming that oxygen concentration in the lungs has not changed significantly. Thus we can use a common factor

$$R_{T_1}^{Control} = R_{T_1}^{XTC} = R_{T_1}. \qquad (6.10)$$

On the other hand, to keep the SNR in the last image comparable to those in the first two, the flip angles in the images were chosen to be different. Then if α_{Gas}, $\alpha_{Control}$ and α_{XTC} are the flip angles in a pixel for the three corresponding images, and N is the number

141

of phase encoding steps, we will have

$$R_{RF}^{Control} = (\cos[\alpha_{Gas}])^{N/2} \cdot (\cos[\alpha_{Control}])^{N/2} \cdot \sin[\alpha_{Control}], \quad (6.11)$$

$$R_{RF}^{XTC} = (\cos[\alpha_{Control}])^{N/2} \cdot (\cos[\alpha_{XTC}])^{N/2} \cdot \sin[\alpha_{XTC}]$$

where the center of the $k - space$ represents the intensity of an image. Then

$$R_{Depol} = \frac{S_{XTC}}{S_{Control}} \cdot \frac{S_{Gas}}{S_{Control}} \cdot \frac{R_{RF}^{Control}}{R_{RF}^{XTC}}. \quad (6.12)$$

Finally, the fractional gas transport F in a pixel, which carries information about locally averaged surface area to volume ratio of the alveoli per pixel per pulse, will be

$$F(t_{exchange}) = 1 - \sqrt[N_{inv}]{R_{Depol}} \quad (6.13)$$

where $t_{exchange}$ is the chosen exchange time and N_{inv} is the number of inversion pulses applied at dissolved state frequency between a pair of images.

Performing analysis in this fashion we mapped the fractional gas transport distribution on a pixel by pixel basis. Then we obtained the mean value of F and its distribution, together with the superior/inferior position dependence of the distribution.

6.2.3 Error Analysis

The heterogeneity in fractional diffusive gas transport $\sigma_{F,Total}$ has contributions from two sources: physiological heterogeneity $\sigma_{F,Physiol}$ of the lungs and the system noise $\sigma_{F,noise}$. In order to estimate and separate system noise contribution to the fractional gas transport distribution, we need to calculate the error in F due to the noise in Gas, Control and XTC images. It is widely accepted in the MRI community that the noise in images has a Rician distribution ([31], [29], [55], [59]). The Rician noise is signal dependent, rather than

142

a simply additive. In the regions with low SNR the noise distribution tends to the Rayleigh distribution, whereas in high SNR regions the Rician distribution is well-approximated as a Gaussian. Hence in high SNR regions the MRI noise can be treated as Gaussian white noise with a standard deviation σ.

In these experiments we obtained an additional data set before the actual experiment with xenon, where the subject was breathing regular air. Then an image mask corresponding to the area of the image where the lung was located in the actual XTC images was used to determine the region of interest in the noise-only images. Then if we write the mean value of F(t) as

$$\bar{F}\left(\bar{S}_{Gas}, \bar{S}_{Control}, \bar{S}_{XTC}\right) = 1 - \sqrt[N_{inv}]{\frac{\bar{S}_{Gas}}{\bar{S}_{Control}} \cdot \frac{\bar{S}_{XTC}}{\bar{S}_{Control}} \frac{R_{RF}^{Control}}{R_{RF}^{XTC}}} \qquad (6.14)$$

and let σ_{Gas}, $\sigma_{Control}$ and σ_{XTC} be the standard deviations of the noise calculated from those chosen regions of Gas, $Control$ and XTC images, and $\bar{S}_{Gas}$, $\bar{S}_{Control}$ and $\bar{S}_{XTC}$ be the mean values of the signals in Gas, $Control$ and XTC images, respectively, then simple error propagation yields

$$\sigma_{F,\ noise} = \frac{1}{N_{inv}} \sqrt[N_{inv}]{\frac{\bar{S}_{Gas}}{\bar{S}_{Control}} \cdot \frac{\bar{S}_{XTC}}{\bar{S}_{Control}} \frac{R_{RF}^{Control}}{R_{RF}^{XTC}}} \sqrt{\frac{\sigma_{Gas}^2}{\bar{S}_{Gas}} + 4\frac{\sigma_{Control}^2}{\bar{S}_{Control}} + \frac{\sigma_{XTC}^2}{\bar{S}_{XTC}}}. \qquad (6.15)$$

Since the noise is added incoherently, the physiological contribution will be

$$\sigma_{F,\ Physiol.} = \sqrt{\sigma_{F,\ Total}^2 - \sigma_{F,\ noise}^2} \qquad (6.16)$$

6.3 Spectroscopic Studies

The mean gas exchange in the lungs as a function of the diffusion time was measured using a spectroscopic counterpart of the Single-Breath Xenon polarization Transfer Contrast

143

technique and compared to that measured with the Chemical Shift Saturation Recovery

technique, described in the previous chapter. XTC spectroscopy sequence is identical to

the imaging sequence, except instead of collecting 3 images, we collect 3 simple FID signals.

The cycle is then repeated for several different exchange times. When data are fitted to the
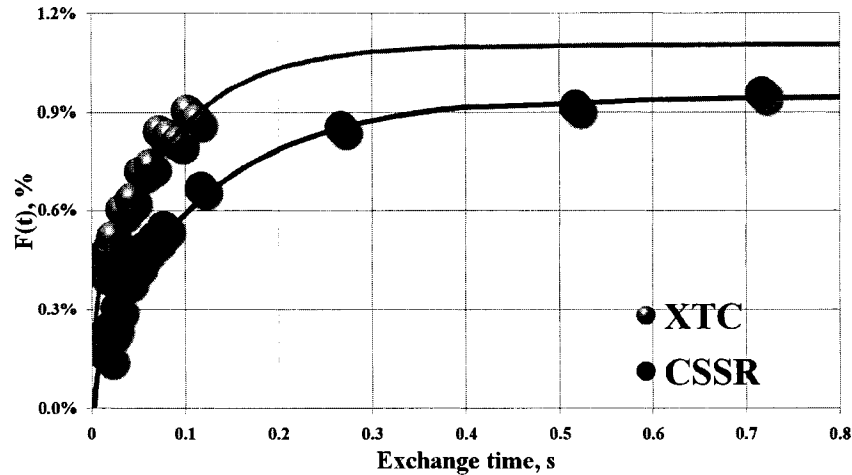
Figure 6.3: Comparison of $\bar{F}(t_{exchange})$ dependence on exchange time measured using CSSR

and XTC methods. Both methods provide the same functional form for the short times

and predict virtually the same tissue thickness

equation describing the long time behavior of the gas exchange (5.35), both sets provide

the same tissue thickness: 16.525 μm, with other parameters being somewhat different.

For XTC spectroscopy data the best fit is achieved with $F_o = 0.0021$, $t_0 = 0.0016$ s and

$c = 0.0093$. For the $CSSR$ data set - $F_o = 0.0020$, $t_0 = -0.0071$ s and $c = -0.0113$.

6.4 Calibration of the technique

In order to validate the XTC sequence, we ran a number of tests with hyperpolarized

xenon in several different phantoms, such as glass cells and Tedlar bags, where one expects
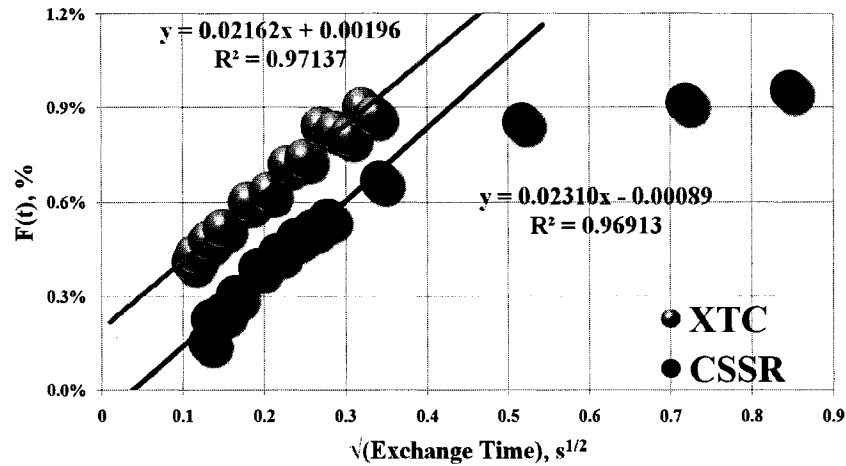
Figure 6.4: Fit of $\bar{F}(t_{exchange})$ vs. $\sqrt{t_{exchage}}$ measured using CSSR and XTC methods to a linear function. Both data sets provide very close in value slopes, predicting close tissue thickness value.

to measure no gas exchange, i.e. $\bar{F}(t_{exchanhe}) = 0$. Results from these calibration runs are presented in Table (6.1). Figure (6.5) shows a sample set of such a run. As can be seen from the results of the calibration runs, mean fractional gas transport is zero in a phantom and *in vivo* measurement of $F(t_{exchange})$ is unambiguous.

A number of experiments were performed with human subject #22 (HS22), where we kept all experimental parameters the same except the number of inversion pulses. These experiments not only helped determine the optimal number of $\pi - pulses$, but also verified the validity of Eqn.(6.13). Figure (6.6) shows the plot of the mean fractional depolarization versus the number of inversion pulses. The error bars in this plot are from the propagated error of $F(t)$: $\sigma_{F,noise}$ (Eqn. (6.15)). One expects the error bars at the limits of the range to be relatively large. For example, for a low number of inversions, the resulting change in the signal due to diffusive gas transport will be small and therefore ill-determined. At the

145

$Date$	$\bar{F}(t_{exchange})$, %	$\sigma_{F,Total}$
10.13.2005	0.18	0.3
10.14.2005	0.081	0.39
04.10.06	−0.023	0.32
08.11.2006	0.037	0.2
08.15.2006	0.021	0.29
08.21.2006	0.019	0.25
08.24.2006	0.059	0.28
08.31.2006	0.063	0.27
07.12.2006	0.034	0.081

Table 6.1: XTC calibration runs with hyperpolarized xenon in a number of phantoms with only gaseous xenon. In a cell, where there is no gas exchange, one expects to measure zero mean fractional gas transport. The exchange time was set to 62 ms. It should be noted that these experiments were imaging experiments and nor spectroscopic studies, and the mean fractional gas transport values are from a region of interest in an image.
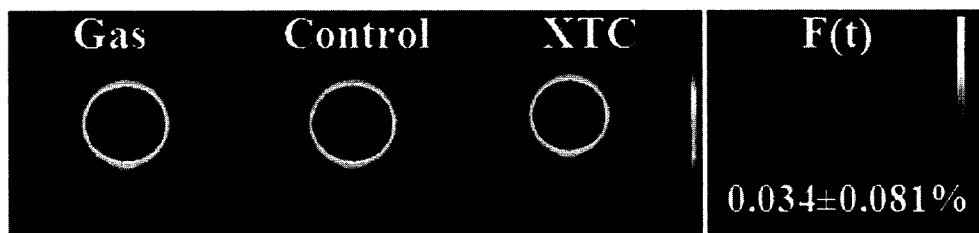
Figure 6.5: The XTC calibration run performed in a 1-Liter spherical glass cell filled with hyperpolarized Xenon to 576Torr. The mean fractional depolarization per pulse was calculated to be $F_{depol} = 0.034 \pm 0.081\%$.
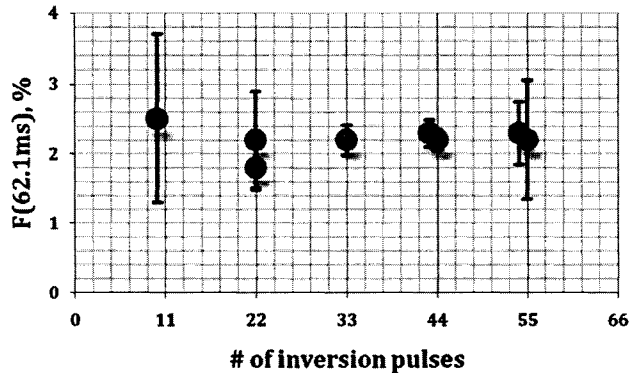
Figure 6.6: Mean fractional gas transport as a function of the number of inversion pulses. The error bars here are from the propagated error.

opposite end of the iteration range, i.e. for a large number of inversions, the change in the signal is large resulting in a poor SNR for the XTC image. As evident from Figure(6.6), the errorbars are small for $30 - 50$ inversion pulses. We chose to use $N_{inv} = 44$ inversion pulses. This provided enough attenuation in the gas state signal, still yielding acceptable SNR in the XTC image.

6.5   Results

6.5.1   XTC Data

The concept of XTC imaging was used to make a spatial map of the fractional diffusive gas transport, $F(t)$, distribution in the lungs. An inter-pulse delay time of 62.1 ms was selected, for which, according to $CSSR$ and XTC spectroscopy measurements, $F(t_{exchange}) \propto \sqrt{t_{exchange}}$. Experiments were done on 14 normal healthy human subjects, 5 of whom were non-smokers, 2 were non-smokers, but have been exposed to 2nd hand smoking everyday for more than 1.5 year, and 7 are smokers with smoking history of more than 1.5 pack years.

147

Gas Image   **Control Image**   **XTC Image**
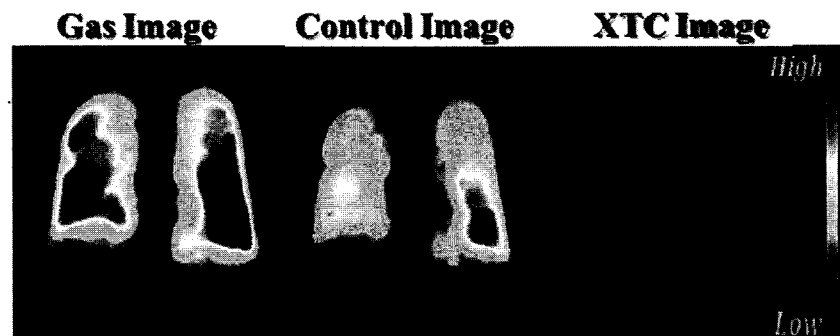
Figure 6.7: Coronal gradient echo projection images of the lungs from XTC experiment. Gas image was acquired before the application of the inversion pulses, Control – after application of the inversion pulses at -205 ppm, and XTC image – after the ones applied at $+205$ ppm. Images are corrected for flip angle differences, i.e. the loss of the signal intensity from Gas to Control is due to T_1 relaxation and RF pulses, and that from Control to XTC is due to the inversion of the gaseous xenon diffused into the alveolar wall as well as the subsequent exchange between phases only.

148

Tables (4.3, 4.4 and 4.2) provide details about the estimated and measured lung volumes for the subjects, their measured DL_{CO} and FEV_1 results, as well as their smoking history. All subjects underwent experiments at 2 different lung volumes: one - close to FRC and another - between FRC and TLC. For 12 of 14 subjects, experiments were repeated at least twice at one of the lung volumes to establish repeatability of the measurements. The list of the subjects with details about the experiments are provided in Tables(6.2,6.3 6.4, 6.5).

Subject	Exp.#	Gas, L	LV/TLC	$\overline{F(62ms)}$	$\sigma_{F,Total}$	$\sigma_{F,noise}$	$\sigma_{F,Physiol.}$
HS4	1	3.90	0.82	0.77	0.39	0.13	0.37
	2	1.35	0.46	1.5	0.41	0.14	0.4
	3	1.30	0.45	1.5	0.42	0.15	0.4
HS6	1	1.56	0.47	1.7	0.38	0.12	0.36
	2	1.58	0.46	1.3	0.48	0.14	0.46
	3	1.60	0.45	1.7	0.38	0.09	0.37
	4	2.60	0.63	1.3	0.29	0.12	0.26
HS13	1	1.25	0.42	1.7	0.42	0.12	0.40
	2	1.30	0.43	1.4	0.58	0.24	0.53
	3	1.35	0.44	1.8	0.48	0.20	0.44
	4	3.00	0.66	0.98	0.35	0.14	0.32

Table 6.2: Lung volume, measured fractional gas trasport and standard deviations for the XTC experiments with normal healthy non-smokers.

A set of sample images from a single breath XTC experiment is presented in Figure

149

Subject	Exp.#	Gas, L	LV/TLC	$\overline{F\,(62ms)}$	$\sigma_{F,Total}$	$\sigma_{F,noise}$	$\sigma_{F,Physiol.}$
HS18	1	0.80	0.39	2.4	0.6	0.35	0.49
	2	0.77	0.38	2.2	0.61	0.19	0.58
	3	1.50	0.53	1.4	0.27	0.08	0.26
	4	0.82	0.39	1.9	0.54	0.14	0.52
	5	0.57	· 0.34	2.1	0.53	0.37	0.38
	6	1.5	0.53	1.5	0.29	0.08	0.28
	7	0.60	0.34	1.5	0.8	0.22	0.77
HS20	1	0.60	0.41	2.1	0.74	0.35	0.65
	2	1.05	0.53	1.8	0.51	0.28	0.43
	3	1.00	0.52	1.9	0.41	0.25	0.32
	4	0.97	0.51	1.7	0.54	0.22	0.49

Table 6.3: Continuation of the table "Lung volume, measured fractional gas trasport and standard deviations for the XTC experiments with normal healthy non-smokers".

150

Subject	Exp.#	Gas, L	LV/TLC	$\bar{F}$ (62ms)	$\sigma_{F,Total}$	$\sigma_{F,noise}$	$\sigma_{F,Physiol.}$
HS22	1	1.50	0.39	2.2	0.69	0.15	0.67
	2	1.55	0.39	2.3	0.72	0.19	0.69
	3	3.04	0.59	1.7	0.41	0.10	0.40
HS23	1	1.41	0.36	2.4	0.61	0.11	0.60
	2	1.45	0.36	2.6	0.83	0.25	0.79
	3	3.16	0.64	2.1	0.33	0.09	0.32

Table 6.4: Lung volume, measured fractional gas trasport and standard deviations for the XTC experiments with normal healthy non-smokers exposed to 2nd hand smoke.

(6.7). The *Gas* image was acquired before the application of the inversion pulses, *Control* image – after their application at −205 *ppm*, and *XTC* image – following the ones at +205 *ppm*. The *XTC* image is corrected for the flip angle differences and scaled so that the loss in the intensity of the signal from *Gas* image to *Control* image is due to T_1 relaxation of the xenon gas and RF depletion of the magnetization, and that between *Control* and *XTC* images is due to the inversion of the xenon magnetization in the dissolved state and the exchange taking place between the two states only. Note that the signal in the trachea did not change significantly, whereas the change in the rest of the lungs is quite large. That is what one expects to see, since the surface area available for exchange is small in trachea.

6.5.2 Intra-subject comparison

From these 3 images we calculated the spatial distribution of F (62 ms), which is presented in Figure (6.8). The experiments were done at 2 different lung volumes. The hypothesis is that at higher lung volume, alveolar surface area increases slower than gas volume and

Subject	Exp.#	Gas, L	LV/TLC	$\bar{F}$ (62ms)	$\sigma_{F,Total}$	$\sigma_{F,noise}$	$\sigma_{F,Physiol.}$
HS14	1	1.25	0.46	2.3	0.45	0.11	0.44
	2	2.30	0.47	2.5	0.49	0.10	0.48
	3	2.70	0.68	1.8	0.31	0.10	0.29
HS15	1	0.64	0.40	2.6	0.9	0.32	0.84
	2	1.8	0.65	1.5	0.61	0.09	0.60
HS16	1	1.92	0.69	1.5	0.37	0.18	0.32
	2	0.90	0.47	2.6	0.59	0.42	0.41
HS17	1	1.03	0.44	1.9	0.65	0.16	0.63
	2	0.98	0.43	2.1	0.68	0.24	0.64
	3	2.4	0.65	1.7	0.35	0.08	0.34
HS19	1	0.90	0.42	2.4	0.54	0.12	0.53
	2	0.85	0.41	2.5	0.62	0.12	0.61
	3	1.85	0.63	1.9	0.45	0.09	0.44
HS21	1	0.90	0.42	2.5	0.79	0.24	0.75
	2	1.00	0.44	2.3	0.83	0.35	0.75
	3	2.10	0.63	1.7	0.33	0.08	0.32
HS26	1	1.85	0.57	1	0.29	0.08	0.28
	2	1.00	0.45	1.2	0.44	0.18	0.40
	3	2.00	0.59	1	0.40	0.18	0.36

Table 6.5: Lung volume, measured fractional gas trasport and standard deviations for the XTC experiments with normal asymptomatic smokers.
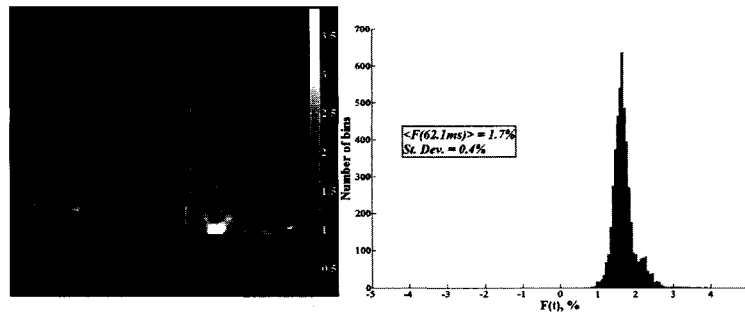
152

Figure 6.8: The fractional depolarization map and its distribution histogram. The data are from a healthy subject, at close to FRC lung volume.

therefore S_A/V_{Gas} and $F(t)$ are expected to decrease [39]. In addition, as lung volume approaches TLC, regional heterogeneity is known to decrease. Depolarization maps at two lung volumes are presented in Figure (6.9) which display the aforementioned behavior.

Although the data are collected in the supine position, at lower lung volumes we see higher values of F(t) at the bases than at the apices. Closer to TLC these differences in superior/inferior direction even out. This is evident from the apex-base plots at two different lung volumes shown in Figure (6.10).

6.5.3 Inter-subject comparison: Non-smokers versus Smokers

To evaluate the sensitivity of the XTC technique, we performed experiments with not only normal healthy non-smokers, but asymptomatic smokers as well. We considered a subject to be a non-smoker, if at the time of participation in the experiments he or she was not active smoker, and had less than one and a half pack years of previous smoking history. Also, we considered a subject to be a asymptomatic smoker if he/she was active smoker at the time of participating in the experiments and his/her FEV_1 and DL_{CO} were more than75% and within $85 - 115\%$ of the predicted values based on sex, age and height, respectively. The

153
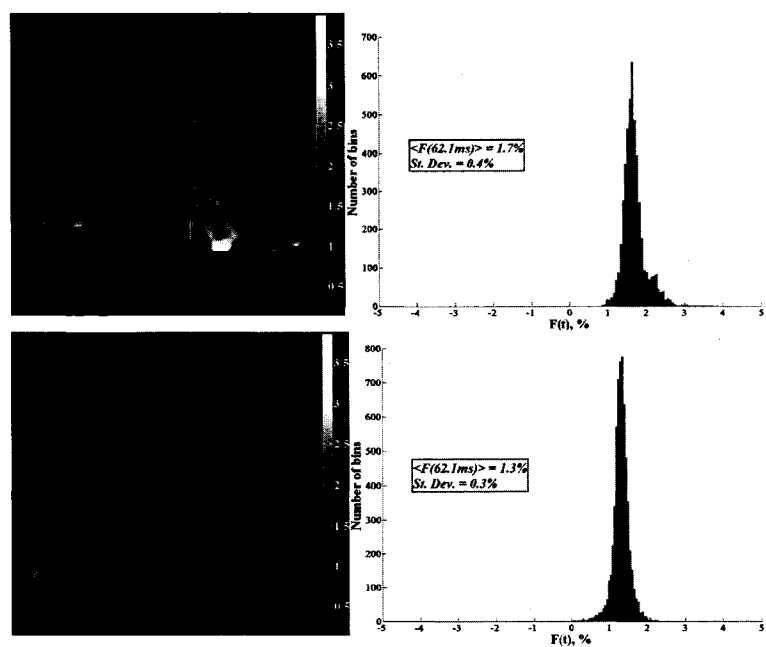
Figure 6.9: Comparison of the fractional Gas transport at two lung volumes: near FRC and near TLC. As expected, the fractional gas transport shows more homogeneous distribution at higher lung volumes.
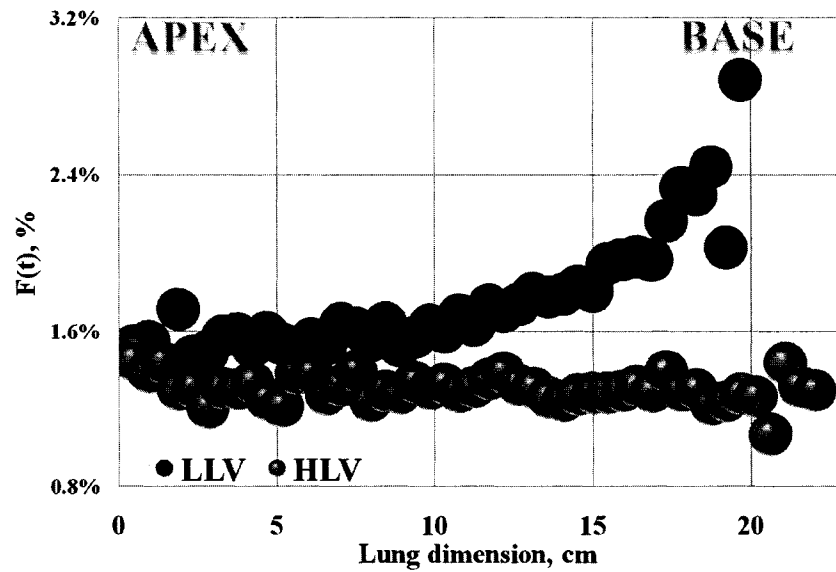
Figure 6.10: Apex to Base distribution of F (62 ms). This is a data set from a healthy normal subject, 32y.o. (HS6). The red dots represent the data at $\sim$ 47% of total lung capacity and the blue ones $-\sim$ 63% of total lung capacity. Data strongly suggests that at lower lung volumes there is a "memory" of gravitational effects in the lungs, even though the data were collected on a supine subject. At higher lung volumes this effect is washed out, and the distribution is more homogeneous.

155
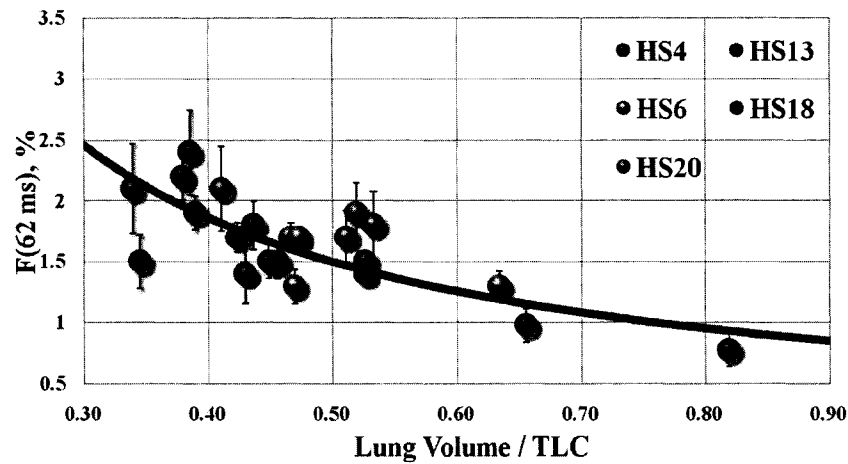
Figure 6.11: Mean fractional Gas transport in non-smokers as a function of normalized lung volume. <F(t)> from all healthy non-smokers is in good agreement within the error, which is represented here by the contribution of the noise to the width of the fractional gas transport distribution. The red line in this graph represents a trend-line, corresponding to the non-smokers and is drawn only for visual comparison with 6.12.

information on PFT and Spirometry results of the subjects is presented in Table(4.3, 4.4). We chose smokers and not people with mild disease for sensitivity evaluation, because at the time of the experiments our FDA and IRB approved protocols allowed experiments on healthy subjects only.

We compare the results from non-smokers to those from the smokers. Figures (6.11) and (6.12) show the mean $F(62.1ms)$ as a function of lung volume normalized to TLC for non-smokers and smokers, respectively. The error bars in both plots represent the measured system noise. The red line in both, (6.11) and (6.12), represents a trend-line for the non-smokers. As evident from the last two figures, most of the smokers have an elevated gas exchange compared to non-smokers.

156
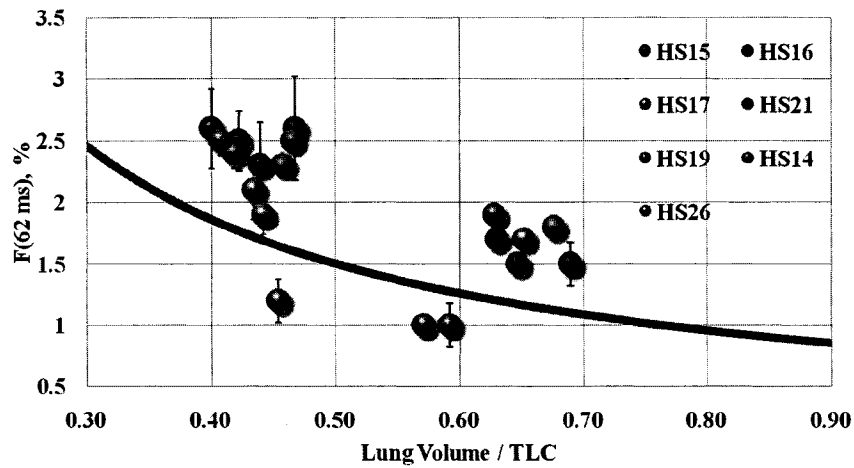
Figure 6.12: Mean fractional Gas transport in asymptomatic smokers as a function of normalized lung volume. Compared to non-smokers, <F(t)> is higher for most of the smokers. The red line here is a trend-line, corresponding to the non-smokers and is drawn for visual comparison only.

The same kind of behavior is seen in physiological heterogeneity $\sigma_{F, physiol.}$ of the fractional gas transport. Figures 6.13 and 6.14 display $\sigma_{F, physiol.}$ for non-smokers and smokers, respectively. As evident from these graphs, the smokers have a somewhat elevated $\sigma_{F, physiol.}$ as well, however the spread in the values is quite wide and more statistics is necessary to draw conclusions.

We also looked at the apex to base distribution of the mean fractional depolarization in the lungs and compared results from non-smokers to those from smokers. Figure (6.15) shows apex-to-base plots for all *low lung volume* (*LLV*) experiments with non-smokers. whereas Figure (6.16) presents that from smokers. As evident from the first figure, there is a common trend in the apex-base distribution for the non-smokers, except HS4, whose plot is characterized by a slightly different shape. This discrepancy may be correlated with age.

157
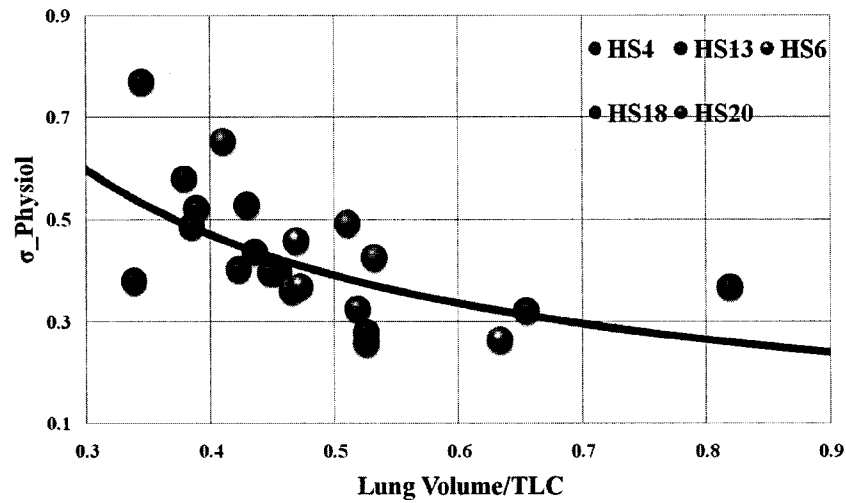
Figure 6.13: $\sigma_{F,\ physiol.}$ for non-smokers. The red line in the graph is a trend line drawn for visual aid only.
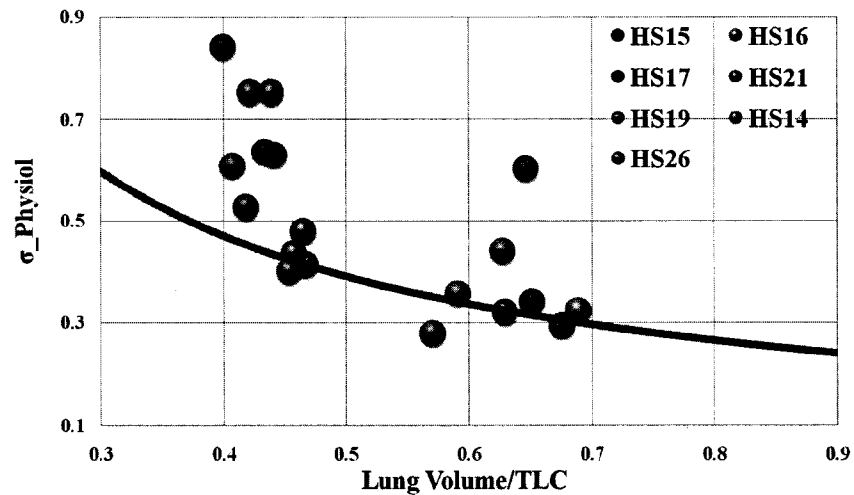
Figure 6.14: $\sigma_{F,\ physiol.}$ for smokers. The red line here represents an average healthy non-smoker. As evident from the graph, smokers have somewhat elevated $\sigma_{F,\ physiol.}$, however the spread is quite wide.

158
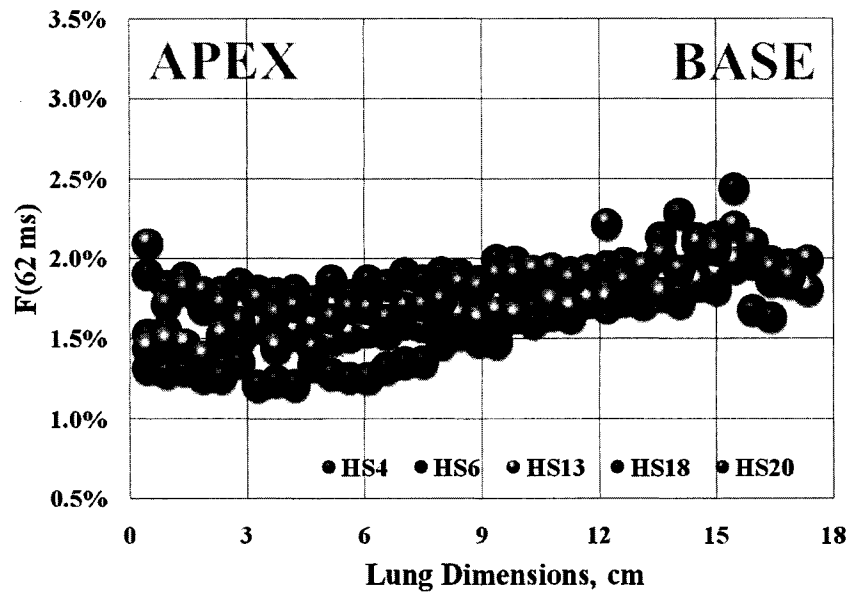
Figure 6.15: Apex to base distribution of fractional gas transport for non-smokers. Data from healthy non-smokers are in great agreement, except the one from HS4, who shows a steeper gradient. This difference might be due to age differences between the subjects (55 vs. 25-35). The red line in the graph represents the averaged apex-base distribution for non-smokers.

159
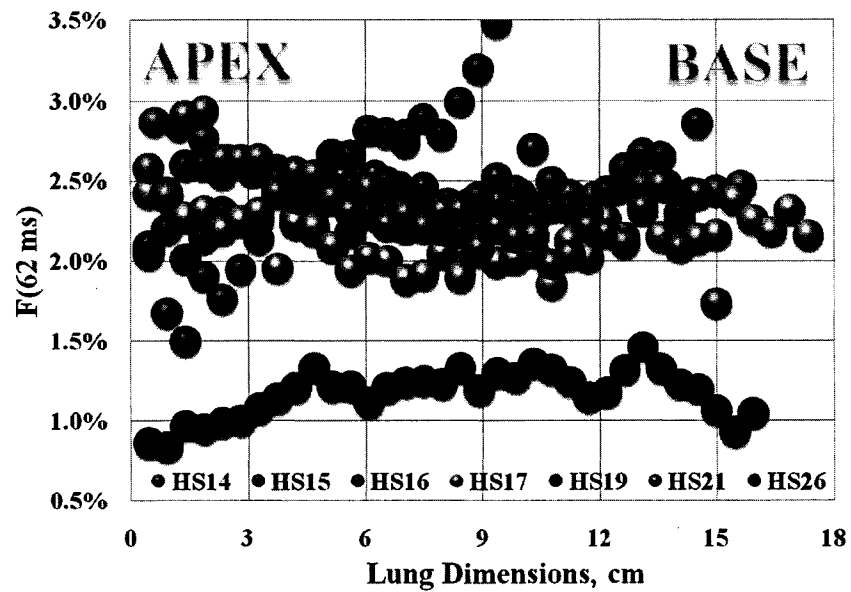
Figure 6.16: Apex to base distribution of fractional gas transport for asymptomatic smokers. In contrast with the non-smokers' data, that from the smokers do not show a common trend. The red line in the graph represents the average apex-base trend from non-smokers.

160

Most of the subjects are 23 - 35 years old, with the exception of HS4 (55 y.o.) and HS26

(50 y.o.). The red line in both figures follows the average apex-to-base distribution for

non-smokers. As can be seen from comparison of the "average" non-smoker (red line) apex

to the base distribution of $F(t)$ to that of the smokers' in Figure (6.16), not only most of

the smokers have a higher mean F (62.1 ms), but all of them also show different apex - base

behavior. For example, HS16 and HS15 exhibit steeper slopes compared to non-smokers,

HS17's distinctly deviates from the non-smokers' trend starting from mid-lungs down to

the base. To highlight this feature, we groupped in one plot the apex-base distributions

of $F(t)$ from all subjects (Fig.6.17). The curves were normalized to the first point of each
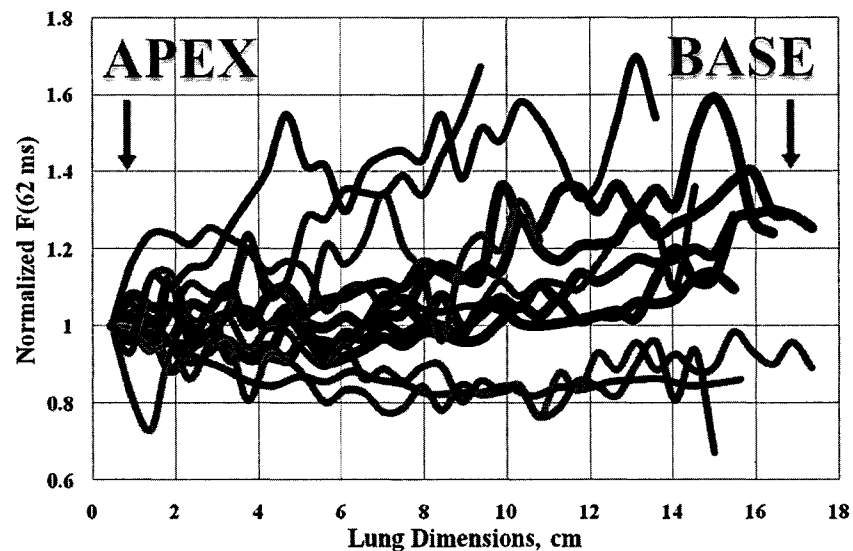
Figure 6.17: Apex-to-Base distribution of $F(t)$ for all subjects. The curves were normalized

to the first point of each set, so that they all originate in one place and so are easier to

compare. The black bold curves as well as the red bold curve correspond to the non-smokers

data. The red curve in particular belongs to HS-4 – the only non-smoker with a slightly

deviating behaviour. All other curves correspond to the smokers' data.

161

set, so that they all originate in one place and so are easier to compare. The black bold

curves as well as the red bold curve correspond to the non-smokers data. The red curve in

particular belongs to HS4 – the only non-smoker with a slightly deviating behavior. In this

picture, the difference between the non-smokers and smokers becomes much more apparent.

The black curves show no significant spread on this scale.

6.5.4 Sensitivity of the XTC Technique

To assess the sensitivity of the XTC method compared to such gold standards as DL_{CO}

and FEV_1, we looked at the dependence of the mean gas exchange $\overline{F(t)}$ and physiological

heterogeneity $\sigma_{F, \, Physiol.}$ on the smoking history at both lung volumes studied and com-

pared them to the dependence of DL_{CO} and FEV_1 on smoking history. Figures (6.18) and
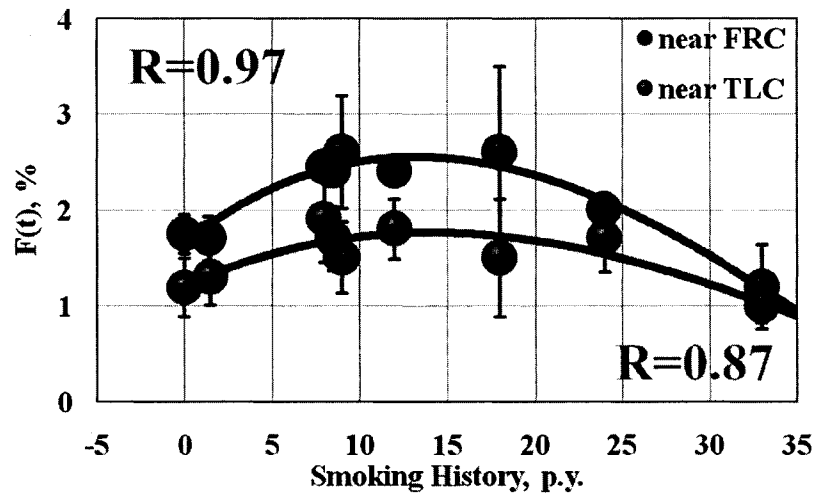
Figure 6.18: The fractional gas transport $\overline{F(t)}$ vs. the smoking history. $\overline{F(t)}$ shows an

interesting behavior with the smoking history. The initial increase in the $\overline{F(t)}$ might be

due to the implamation in the small airways of the smokers' lungs.

() show plots of $\overline{F(62\ ms)}$ and $\sigma_{F, \, Physiol.}$ vs. Smoking history, while Figures (6.20) and

162

() present the same for DL_{CO} and FEV_1.

In Figure (6.18) at zero pack years we are plotting the average fractional gas transport from all experiments done with non-smokers (except one subject, HS6, which is considered non-smoker, but has 1.2 pack years of smoking history. He is plotted separately at 1.2 pack years). As for the rest of the data points in that graph, each of them represents the average
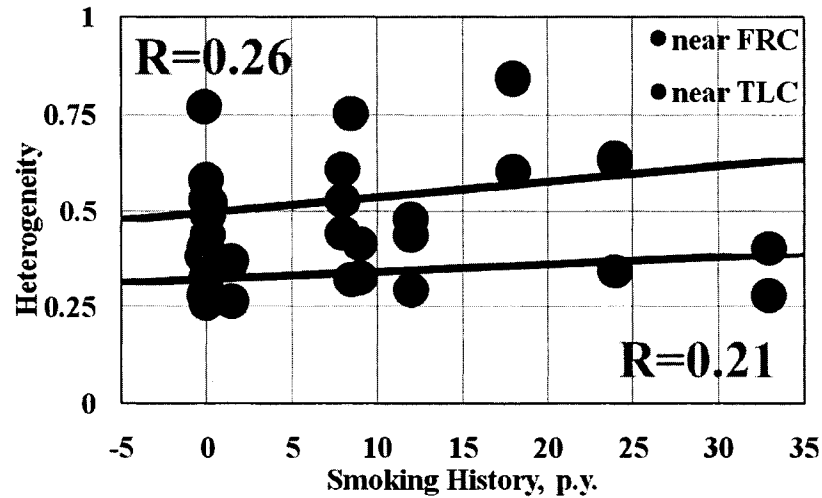
Figure 6.19: The physiological heterogeneity $\sigma_{F,\ Physiol.}$ calculated from the XTC data vs. the smoking history.

$\overline{F\,(62.1\ ms)}$ for each subject.

As for Figures (6.20) and (6.21), we plotted as many data points as we had available - some of the subjects were available only for one day, and failed to take a PFT of Spirometry test.

6.6   Discussion

XTC is a powerful technique capable of delivering information on regional lung characteristics. Modifications introduced into the original XTC allowed its application to human

163
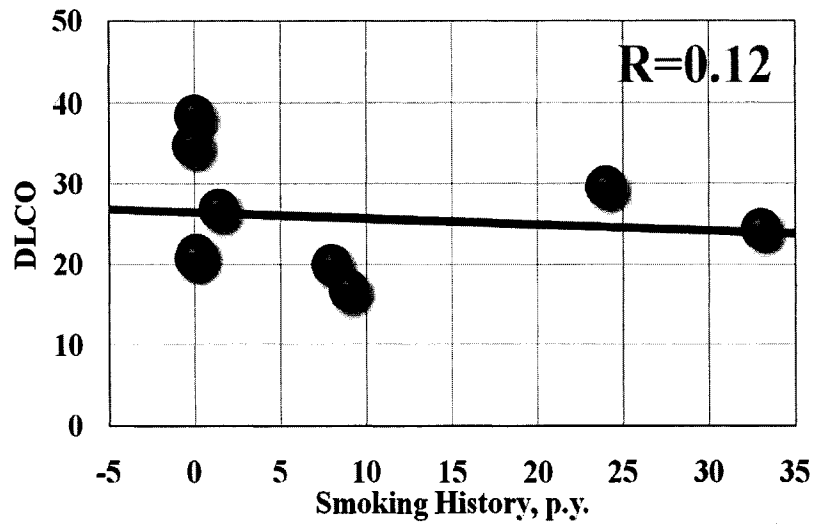
Figure 6.20: DL_{CO} versus smoking history. The diffusion capacity showed no significant correlation with the smoking history.
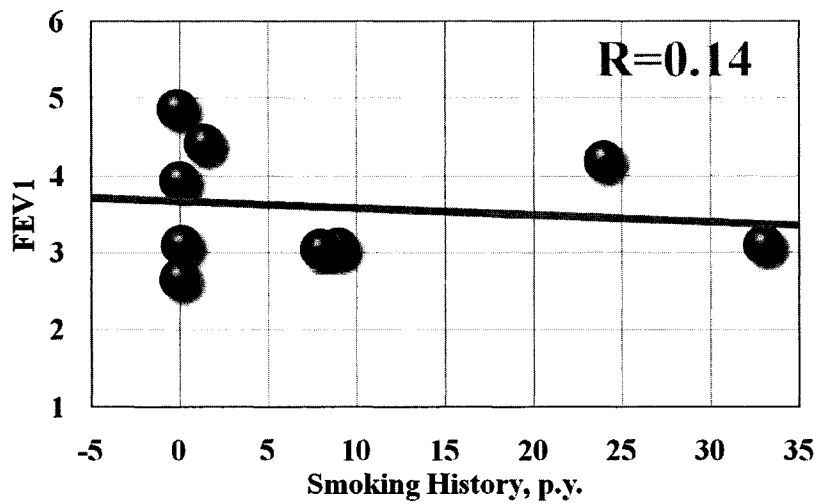
Figure 6.21: FEV_1 versus smoking history. FEV_1 did not show an apparent correlation with the smoking history.

164

subjects and testing its potential to study both, healthy non-smokers and asymptomatic smokers, thus allowing to evaluate the technique's sensitivity to early changes in the lungs. The smokers represented a group of subjects with such possible lung function or structure changes, while still having PFT and spirometry test results within the normal range.

The technique was thoroughly tested on several levels. First, the sequence was calibrated on a phantom containing no solid in which the Xe could diffuse; these experiments yielded numbers consistent with no exchange. Next, the model was validated through a series of experiments with a variable number of inversion pulses that provided a consistent mean fractional gas transport under similar conditions (i.e. the same subject and lung volume). Also, good reproducibility of the mean exchange values confirmed the technique's robustness.

The exchange time was chosen based on the $CSSR$ experiments to measure surface area available for the gas exchange and later confirmed with XTC spectroscopy experiments. In a human lung, tissue volume accounts for ~ 20 % of the total lung volume (gas plus tissue). Assuming a xenon partition coefficient for tissue of 0.1 and sufficiently long exchange time such that the entire tissue is saturated, the net transport will result in a fraction $0.2 \times 0.1 = 0.02$ of the Xe atoms in tissue. XTC measures twice the fractional transport. At the same time the highest value for the mean fractional diffusive gas transport in 62.1 ms was measured at 2.6 % per inversion pulse which when halved to account for XTC technique, gives a maximum of 1.3 %. This number is below 2 % (maximum when saturated), therefore our exchange time is sufficiently short to prevent saturation. There are some areas, where the parenchyma is thinner than 5 μ and in 62.1 ms xenon would cross the tissue-blood barrier and reach the red blood cells. But this defines the "functional" surface area we are

165

measuring.

In a "simple elastic sphere" model of pulmonary parenchyma where alveoli are characterized as roughly spherical, with a uniformly distributed characteristic linear dimension r, the lung's gas volume $V_{Gas} \propto r^3$, while the surface area $S_A \propto r^2$. Together, this implies the surface area density per gas volume, $\frac{S_A}{V_{Gas}} \propto \frac{1}{r}$, and hence decrease with lung volume. With XTC we observed such behavior - $\bar{F}(t_{exchange})$ decreased with the increase of the lung volume for all subjects (Figs. 6.9).

At lower lung volumes, the average alveolar size is greater at the apices of the lungs than at the base. Also, the relative regional ventilation is higher at the bases. These two effects combined create a gradient in the alveolar surface area to gas volume ratio distribution. Although our measurements were performed in supine subjects, such behavior was still detected in all subjects (Figs. 6.15, 6.16). We refer to this phenomenon as the "memory" of the lungs. On the other hand, it is widely accepted that, at least in normals, alveolar size is more homogeneous at higher lung volumes [48], which in turn implies a marked decrease in any $\frac{S_A}{V_{Gas}}$ gradient; this is also supported by our data (Figure 6.10).

Despite the limited statistics a noticeable trend appears in the non-smokers' apex-base distribution, which is not the case with the smokers' data. One possible reason could be early changes in the lungs that do not necessarily follow an identical path in all subjects. For instance, various degrees of degradation of the separate regions in the lungs due to ailments would change the gas-exchange map accordingly, i.e. a smoker starts developing emphysema in the lungs, and let's say, as is the case for most of the smokers, the disease starts off in the apices. Then some of the tissue is destroyed in the apical region, thereby reducing the local exchange surface and $F(t)$ in that area. Then the slope of the apex

166

to base plot will be elevated. Examples of such data are the apex to base distributions for HS15 and HS16 (see Figure 6.16). On the other hand, if the affected area is in the basal part of the lungs, then the apex to base slope will diminish. This peculiarity of the apex-base distribution of F(t) in smokers suggests that XTC is sensitive to early changes in the lungs.

The dependence of $\overline{F}(t)$ on the smoking history shows very curious behavior: for the first several years of smoking $F(t)$ increases, then reaches a maximum at ~ 12 pack years, and begins declining. We have yet to determine the exact cause of such behavior. One possible explanation of the increased signal might be the presence of inflammations and mucus build-up in early stages of smoking which reduces the available gas volume. As long as this increase in the signal compensates the decrease due to possible tissue deterioration, the total signal value may be elevated.

Moreover, the $\overline{F}(t)$ vs. the smoking history correlation constant ($R_{High\ Lung\ Vol.} = 0.97$ and $R_{Low\ Lung\ Vol.} = 0.87$) compared to correlation constants of DL_{CO} ($R = 0.12$) and FEV_1 ($R = 0.14$) implies that XTC may be more sensitive to early changes in the lungs compared to these commonly used tests. However, a larger study population in both groups will be necessary to confirm these preliminary results, particularly given the apparently large variability among the asymptomatic smokers. As for the physiological heterogeneity, although at both lung volumes it displayed slightly higher correlation constants ($R_{High\ Lung\ Vol.} = 0.26$ and $R_{Low\ Lung\ Vol.} = 0.21$) compared to those of DL_{CO} and FEV_1, there is a large spread present in the distribution, and more statistics is required.

Moreover, the dependence of $\bar{F}(t)$ on the smoking history is in contrast to the failure of DL_{CO} and FEV_1 to detect any changes in normal or asymptomatic smokers. This

167

is evidence that XTC is more sensitive to early changes in the lungs compared to these commonly used tests. However, a larger study population in both groups will be necessary to confirm these preliminary results, particularly given the apparently large variability among the asymptomatic smokers.

XTC data can be further supplemented by investigating the local gas exchange as a function of the time allowed for diffusion. In particular, extending this work to include the local septal thickness effect will be one avenue by which a noninvasive assay can be made that specifically differentiates the separate contributions of the septal area and the thickness to the mean local tissue density (as can be measured with CT). This will represent an important step in the diagnosis and management of parenchymal diseases such as idiopathic pulmonary fibrosis, as well as pathologies involving interstitial edema.

CHAPTER 7

THE DIXON TECHNIQUE

7.1 Background of the Technique

If our goal is to measure either the structural or the functional local surface area of the lungs, we need a technique to simultaneously measure signals from dissolved and gaseous xenon in the lungs, which have different resonant frequencies. A similar problem is posed in conventional MRI. The MRI signal in the living tissue is largely composed of ^1H in water, the signal from other hydrogen nuclei being much smaller. An important exception to this is fatty tissue, i.e. hydrogen from CH_2 based tissue elements, which has a chemical shift of 3.35 ppm from H_2O, just like dissolved state xenon is chemically shifted from the gaseous counterpart by 205 ppm. The chemical shift refers to the phenomenon of identical nuclei experiencing different levels of magnetic shielding due to their chemical environment. We noted in previous chapters, that differences in magnetic shielding cause nuclei in various chemical climates to precess with slightly different frequencies. The shift in frequency due to the chemical shift σ is

$$\Delta f(\sigma) = -\sigma \gamma B_0, \tag{7.1}$$

where γ is the gyromagnetic ratio of the nucleus and B_0 is the main magnetic field. Hence

$$\sigma = \frac{\Delta f}{f_0} \tag{7.2}$$

and usually quoted in ppm.

169

Now let assume we have a phantom consisting of two types of tissues, A and B, with a relative chemical shift of σ. For a simple gradient echo sequence, the complex image at a time TE will be:

$$\widetilde{I}\left(T_E\right) = I_A\left(T_E\right) + I_B\left(T_E\right). \tag{7.3}$$

Let us allow the type A tissue to be on resonance, and assume that $\vec{B}_0$ is perfectly homogeneous in the field of view of the image. Then the phase of A and B during the sampling period is

$$\phi_A\left(t'\right) = -\gamma G_x \cdot x \cdot t' = \underbrace{-2\pi \cdot k_x \cdot x}_{Frequency\ Encoding} \tag{7.4}$$

and

$$\phi_B\left(t'\right) = -\gamma\left(G_x\ x + \Delta B_{AB}\right)\ t' - \gamma\Delta B_{AB}\ T_E = \underbrace{-2\pi\ k_x \cdot \left(x + \frac{\Delta B_{AB}}{G_x}\right)}_{Frequency\ Encoding} - \Delta f_{AB}\ T_E$$

$$\tag{7.5}$$

The extra term in the frequency encoding part of Eqn. (7.5) is called frequency encoded shift. This term creates problems if $\Delta f_{voxel} = \frac{\gamma}{2\pi}G_R \cdot \Delta x$ is not much greater than Δf_{AB}. The actual shift in absolute distance units is $\Delta x_{shift} = \frac{\Delta f_{AB}}{\Delta f_{voxel}} \cdot \Delta x$. It is evident from Eqns. (7.4) and (7.5), that I_A is real, while I_B is complex having a T_E-dependent phase. Then (7.3) can be written as

$$\widetilde{I}\left(T_E\right) = |I_A\left(T_E\right)| + |I_B\left(T_E\right)| \cdot e^{-i\Delta f_{AB}T_E} \tag{7.6}$$

7.2   1-point Dixon Technique

If we choose T_E such that

$$\Delta f_{AB}\ T_E\left(n\right) = 2n\pi + \frac{\pi}{2}, \tag{7.7}$$

170

where n is an integer, and for $n = 1$ we have $e^{-i\Delta f_{AB} T_E} = e^{-i\frac{5}{2}\pi} = i$. Then in the absence of the main field inhomogeneities the image can be written as

$$\widetilde{I}\left(T_{E,\,\pi/2}\right) = |I_A| + i \cdot |I_B|, \tag{7.8}$$

making the separation of the images quite simple - the real part of the image data is the signal from tissue type A, and the imaginary part - that from tissue type B. Unfortunately in reality the B_0 field is never perfectly homogeneous, and for this separation to work we need to collect another image at echo time T_E, such that spins from A and B are in phase, i.e.

$$\Delta f_{AB}\, T_E\left(n\right) = 2n\,\pi. \tag{7.9}$$

Then the images will be written as (for the case of $n = 1$)

$$\widetilde{I}_{in} = \left(|I_A| + |I_B|\right) \cdot e^{-i\phi_{\Delta B}} \tag{7.10}$$

and

$$\widetilde{I}_{\pi/2} = \left(|I_A| + i \cdot |I_B|\right) \cdot e^{-i\frac{5}{4}\phi_{\Delta B}}, \tag{7.11}$$

where $\phi_{\Delta B} = \gamma \cdot \Delta B \cdot T_{E,\,in}$ is the phase gained due to the magnetic field inhomogeneities. This phase map is then calculated from the image $\widetilde{I}_{in}$ (Eqn. 7.10) and used to remove the phase from image $\widetilde{I}_{\pi/2}$ (Eqn. 7.11). There are certain difficulties with this technique: phase maps are computed only over a region $[-\pi,\,\pi]$ - any value of the phase above π wraps back to a negative value, making a correct prediction of the phase almost impossible. In addition, problems can arise if a constant T_E-independent phase shift is present that depends on the position.

171

7.3 2-point Dixon Technique

The so called 2-point Dixon Technique is the original version of the technique, developed by Dr. W. Thomas Dixon in 1984. In this case 2 images are collected at such T_E's, that in the first image A and B are in phase (Eqn. 7.9) and are in opposite phase in the second. This state is reached when

$$\Delta f_{AB}\, T_E\,(n) = (2n + 1)\,\pi. \tag{7.12}$$

Then again for n=1 the images will be

$$\widetilde{I}_{in} = I_A + I_B \cdot e^{-i2\pi} = I_A + I_B \tag{7.13}$$

$$\widetilde{I}_{opp} = I_A + I_B \cdot e^{-i3\pi} = I_A - I_B, \tag{7.14}$$

where $\widetilde{I}_{in}$ and $\widetilde{I}_{opp}$ are images collected in "parallel" and "anti-parallel" phases, respectively. Then half of their sum will provide true image of tissue type A, and half of the difference - true image of the tissue type B.

The above separation works only when the chemical shift between the two components is the only source of the off-resonance signal. In the presence of field inhomogeneities, the separation is not accurate anymore, since the algorithm is not able to discern phase shifts caused by ΔB, $\phi_{\Delta B}$, from those deriving from σ_{AB}. Also a constant position–dependent phase shift ϕ_0 is associated with each acquisition. This phase shift rises from inhomogeneous penetration of the imaging volume by RF pulses, as well as delays in the system electronics. Given these extra sources of phase shift, images will be written as

$$\widetilde{I}_{in} = (I_A + I_B)\, e^{-i\phi_0} \tag{7.15}$$

172

and

$$\widetilde{I}_{opp} = (I_A - I_B)\, e^{-i(\phi_0 + \phi_{\Delta B})}. \tag{7.16}$$

B.D. Coombs, J. Szumowski and W. Coshow [5], as well as T.E. Skinner and G.H. Glover [79] extended the original 2-point Dixon method reconstruction to include phase corrections based on these the same information from the two image data. First, they calculate the phase map due to the field inhomogeneities. To do that let's take a look at

$$
\begin{aligned}
\left(\widetilde{I}_{in}^{*}\widetilde{I}_{opp}\right)^{2} &= \left[(I_A + I_B)\, e^{i\phi_0} \cdot (I_A - I_B)\, e^{-i(\phi_0 + \phi_{\Delta B})}\right]^{2} \\
&= \left[(I_A + I_B)\cdot(I_A - I_B)\right]^{2} e^{-2i\phi_{\Delta B}},
\end{aligned}
\tag{7.17}
$$

then the phase map will be

$$\Phi = Arg\left[\left(\widetilde{I}_{in}^{*}\widetilde{I}_{opp}\right)^{2}\right] = Wrap\,(2\phi_{\Delta B}) \tag{7.18}$$

as long as $\widetilde{I}_{in}^{*}\widetilde{I}_{opp} \neq 0$, or $I_A \neq I_B$. For the voxels where $I_A = I_B$, the correct images can be obtained without any phase information: $I_A = I_B = \frac{|\widetilde{I}_{in}|}{2}$. Next, this phase map needs to be unwrapped to give an estimate for $2\phi_{\Delta B}$, halved and this will provide the estimated total inhomogeneity phase $\phi_{\Delta B}$. The two groups used different unwrapping algorithms. Coombs *et al.* [5] used the region growing algorithm with manual seed point selection and choice of phase discontinuity parameter threshold [44]. Skinner and Glover on the other hand, used a different algorithm, developed by Moon-Ho et al, using the Poisson equation [74]. After the phase unwrapping the images I_A and I_B are calculated algebraically:

$$I_A = \frac{1}{2}\left|\left(\widetilde{I}_{in} + \widetilde{I}_{out}e^{i\phi_{\Delta B}}\right)\right| \tag{7.19}$$

and

$$I_B = \frac{1}{2}\left|\left(\widetilde{I}_{in} - \widetilde{I}_{out}e^{i\phi_{\Delta B}}\right)\right|. \tag{7.20}$$

173

This analysis technique works quite well for most of the image regions, but has problems when calculating a proper value for the phase in the regions where A and B yield approximately an equal signal. Thus this method fails along the boundaries between the regions dominated by A on one side and B on the other.

7.4 3-point Dixon Technique

In order to remove the problems with ambiguous phase determination in the 2-point Dixon method reconstruction and bleeding of the information about one tissue type into the other's image, several groups proposed collecting data at not 2, but 3 T_E echo times. Having this extra information allowed the calculation of the B_0 field map, thus exact determination of the phase.

Haacke et al [16] were 1st to propose collection of the 3rd image in 1987. Glover et al [28] used a similar approach with collection data at phase shift points of 0, π and $-\pi$. They also developed a two step phase-unwrapping algorithm to determine the phase correctly. Borrello et al [41] used a slightly different approach - they collected an extra image not at another T_E, but rather an image of a homogeneous phantom to map the B_0 field and then use this map in the reconstruction. This approach will work only when susceptibility effects are negligible. In 1998 Wang et al used the same 3-point scheme to collect images at 3 T_E's and proposed yet another pixel-by pixel phase unwrapping approach.

The basic idea behind all these approaches is the same. If we collect images at 3 different T_E times, such that for the 1st image A and B are in phase ($\Delta f_{AB} T_{E,1} = 0$), for the 2nd image they are in opposite phase ($\Delta f_{AB} T_{E,1} = \pi$), and for the 3rd image – back

174

in phase again $(\Delta f_{AB} T_{E,1} = 2\pi)$, then the images can be written as

$$\widetilde{I_1} = (I_A + I_B) e^{-i\phi_0}, \tag{7.21}$$

$$\widetilde{I_2} = (I_A - I_B) e^{-i\phi_0} e^{-i\phi_{\Delta B}},$$

$$\widetilde{I_3} = (I_A + I_B) e^{-i\phi_0} e^{-2i\phi_{\Delta B}}.$$

The 1st and 3rd images are redundant if $\Delta B = 0$. Otherwise, if we take

$$Arg \left[\frac{\widetilde{I_1}}{\widetilde{I_3}} \right] = 2\phi_{\Delta B}, \tag{7.22}$$

after which a phase unwrapping routine is chosen and applied to estimate true $\phi_{\Delta B}$. This is followed by the calculation of the separated images:

$$I_A = \frac{1}{2} \left(\widetilde{I}_{in} + \widetilde{I}_{out} e^{i\phi_{\Delta B}} \right) \tag{7.23}$$

and

$$I_B = \frac{1}{2} \left(\widetilde{I}_{in} - \widetilde{I}_{out} e^{i\phi_{\Delta B}} \right). \tag{7.24}$$

7.5 Pulse sequence

The two previous described techniques, used to measure total and local alveolar surface area to volume ratio in the human lungs. In this chapter we present the 3rd technique, which is a marriage between Chemical Shift Saturation Recovery ($CSSR$) and 3-point Dixon techniques. As described earlier, in $CSSR$ we quench the dissolved xenon signal by applying a $\pi/2$ pulse at 205 ppm, then allowing for the gas to diffuse into the tissue for some time $t_{exchange}$, which is then followed by an application of another $\pi/2$ pulse and data acquisition. Here we combine this method with the Dixon method to observe both, local gas

175

and dissolved state signal simultaneously. This technique provides a direct measurement

of the 2D distribution of alveolar surface area to volume ratio in human lungs.
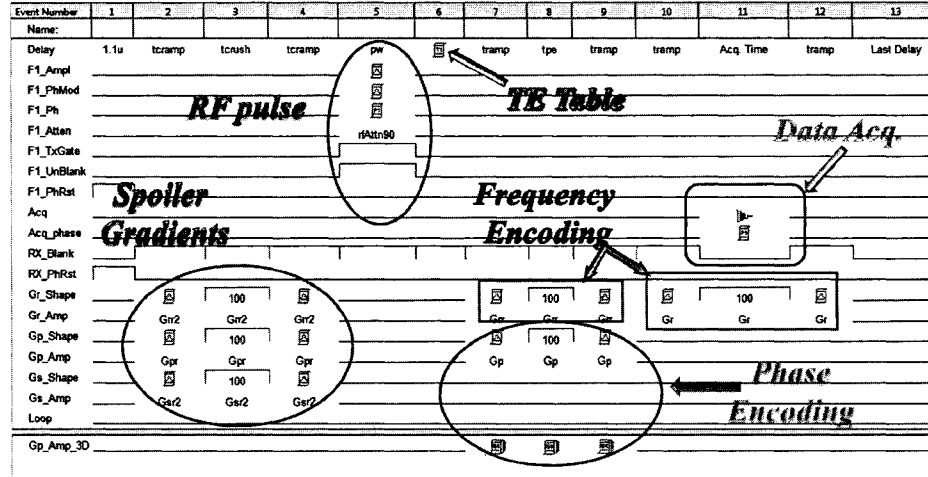

Figure 7.1: The time diagram for the Dixon experiments' pulse sequence.

As mentioned previously, the difference between gaseous and dissolved state xenon

resonance frequencies is about $\Delta\nu = 485\ Hz$. Employing the Dixon technique, we collected

3 images with 3 echo times such that dissolved and gaseous states were in "parallel", "anti-

parallel" and "parallel again" phases, i.e. values for TE were: $T_{E,n} = T_{E,o} + (n-1) \cdot \Delta T_E$,

where n is the number of the image to be collected with $T_{E,n}$ echo time, and $\Delta T_E = \frac{1}{2 \cdot \Delta\nu}$,

and T_0 is the minimum T_E we could afford. We used a 90° flip angle centered at the dissolved

state signal, which tipped the gas state signal 205 ppm away with a 2° flip. In order to

avoid relaxation effects, we collected 3 interleaved images, i.e. the $k - space$ was filled as

shown in Figure (7.2). The pulse sequence parameters were as follows: $TE_o = 8.69\ ms$,

$TR_n = 81.31\ ms + (n-1) \cdot \Delta TE$, $t_{exchange} = 62.5\ ms$; we collected 64 read out points with

$SW = \pm 3\ kHz$, 32 centric encoded $k - space$ lines in the phase encoding direction, i.e.

$k - space$ was filled starting from the center. To minimize the echo time we shifted the

176
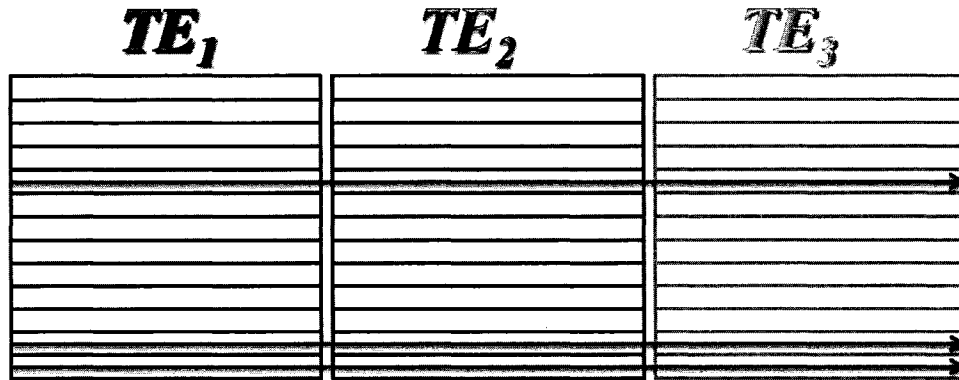
Figure 7.2: 3 interleaved images in 3-point Dixon technique. $k - space$ is being filled one phase encoding line at a time for each image.

echo center from the center of acquisition time - it appeared at $\frac{1}{8}$ *Acq. Time*. The field of view was set to 300 *mm* in both directions. There was no slice selection - the images are coronal gradient echo projections.

7.6 Data Analysis

The dissolved phase xenon signal in the lungs is only about 1% of the total xenon signal, complicating the separation of the signals in Dixon technique. On the other hand, the system noise is of the same order. If in the image reconstruction we use magnitude images, then the "rectified" noise in the image region will have a mean value comparable to that obtained from the dissolved state [29]. To avoid such errors in the reconstruction, we used phased reconstruction. Then the mean value of the signal in the noise-only regions is close to zero.

If we collect 3 images at such T_Es that for the 1st T_E dissolved and gas states are in phase, for the 2nd T_E - they are in opposite phase, and for the 3rd - in phase again. Then

177

the Fourier transforms of 3 collected gradient echoes can be written as:

$$I_1 = \left[D + G \cdot e^{-i\Delta\phi}\right] \cdot e^{-i\phi_o} = [D + G] \cdot e^{-i\phi_o}, \tag{7.25}$$

$$I_2 = \left[D + G \cdot e^{-i\Delta\phi}\right] \cdot e^{-i\phi_o} \cdot e^{-i\phi} = [D - G] \cdot e^{-i\phi_o} \cdot e^{-i\phi},$$

$$I_3 = \left[D + G \cdot e^{-i\Delta\phi}\right] \cdot e^{-i\phi_o} \cdot e^{-2i\phi} = [D + G] \cdot e^{-i\phi_o} \cdot e^{-2i\phi}$$

where I_1, I_2, and I_3 are the the Fourier transforms of the 1st, 2nd and 3rd echoes, D and G are the signals from xenon dissolved into the lung parenchyma and that in alveolar gas spaces only, respectively, which are to be determined; $\Delta\phi = \sigma_{DG}\gamma_{Xe}B_0 T_E$ is the phase due to the chemical shift σ_{DG} between dissolved and gas states, ϕ_o is a constant position–dependent phase shift due to inhomogeneous penetration of the imaging volume by RF pulses, as well as electronics' delays; and $\phi = \gamma \cdot \Delta B \cdot T_E$ is the time–dependent phase. Since the first and third images were collected with the two states in phase, they only differ by an extra phase collected over longer T_E time. Thus their ratio, unwrapped, will provide the time–dependent phase shift:

$$2\phi = \arg\frac{I_1}{I_3}. \tag{7.26}$$

We can use this calculated phase to correct the 2nd image.

$$\widetilde{I_2} = I_2 \cdot e^{-i\phi} \tag{7.27}$$

Now if we take the difference $I_1 - \widetilde{I_2}$ and the sum $I_1 + \widetilde{I_2}$, we get

$$I_1 - \widetilde{I_2} = 2G \cdot e^{-i\phi_o} \tag{7.28}$$

$$I_1 + \widetilde{I_2} = 2D \cdot e^{-i\phi_o} \tag{7.29}$$

Going back to the time domain at this point we can correct for the chemical shift artifact.

So, we can write this signal in the time domain as:

$$s_-(p\Delta t) = \sum_{q=-n}^{n-1} 2G(q\Delta x) e^{-i\gamma gp\Delta xq\Delta t} e^{-i\Delta fp\Delta t} \tag{7.30}$$

$$s_+(p\Delta t) = \sum_{q=-n}^{n-1} 2D(q\Delta x) e^{-i\gamma gp\Delta xq\Delta t} e^{-i\Delta fp\Delta t} \tag{7.31}$$

which if not taken care of here, will result in a shift in the position shift of the off-resonance component in the resulting image, i.e.

$$s_-(p\Delta t) = \sum_{q=-n}^{n-1} 2G(q\Delta x) e^{-i\gamma gp\Delta t\left(q\Delta x - \frac{\Delta B}{g}\right)}, \quad \xrightarrow{\mathcal{F}} \quad 2G\left(q\Delta x - \frac{\Delta B}{g}\right). \tag{7.32}$$

On the other hand, if we correct for this known phase in time domain, we can avoid these chemical shift problems. The phase correction is done simply by multiplying each point of the collected echo with the corresponding phase:

$$\widetilde{s_-}(p\Delta t) = \sum_{q=-n}^{n-1} 2G(q\Delta x) e^{-i\gamma gp\Delta xq\Delta t} e^{-i\Delta fp\Delta t} e^{i\Delta fp\Delta t}$$

$$= \sum_{q=-n}^{n-1} 2G(q\Delta x) e^{-i\gamma gp\Delta xq\Delta t}, \quad \xrightarrow{\mathcal{F}} \quad 2G(q\Delta x) \tag{7.33}$$

Then after this simple phase correction, we will have

$$D = \frac{1}{2}\Re(I_1 + \widetilde{I_2}) \tag{7.34}$$

and

$$G = \frac{1}{2}\mathcal{F}\left(\widetilde{s_-}(p\Delta t)\right) \tag{7.35}$$

respectively.

In order to calculate the values for the fractional gas transport, we have to account for the flip angle differences experienced by each state: if α_D is the flip angle experienced by

179

the dissolved state and α_G is the flip angle experienced by the gas state, then the fractional gas exchange will be:

$$F\left(t_{exchange}\right) = \frac{D \cdot \sin\left(\alpha_G\right)}{G \cdot \sin\left(\alpha_D\right)}.$$ (7.36)

All reconstructions and analyses were performed in Matlab (MathWorks, MA)

7.7 Calibration

The initial tests of the sequence were conducted on a phantom, consisting of 2 cylindrical glass cell, one of which was half filled with corn oil. Immediately before the experiment both cells were evacuated. Since T_1 in the dissolved state is much shorter than in the gas state, the gas only cell was filled with hyperpolarized xenon to atmospheric pressures first, and then placed in the magnet. After that the half-oil cell (see Figure 7.3) was filled to 1 atmosphere. Thereupon the oil cell was vigorously shaken for 8 seconds to ensure xenon dissolution in the oil, and placed on top of the gas only cell. The sequence began without any further delays. Figure 7.3 depicts the experimental setup for such runs. The results of these runs are presented below.

Since the exact solubility coefficient / partition coefficient of xenon for corn oil is undetermined, we needed another way to make sure the sequence is calibrated properly, and that it really measures what we *think* it does. For that we ran the pulse sequence on a phantom, such as glass cell or a Tedlar bag filled with xenon only, where one expects to measure no gas exchange. After successfully passing these tests the technique was used in human studies.

Six experiments in total were performed on 2 normal healthy subjects at 2 different lung volumes. The breathing protocol was as follows: inhale, exhale, inhale, exhale to
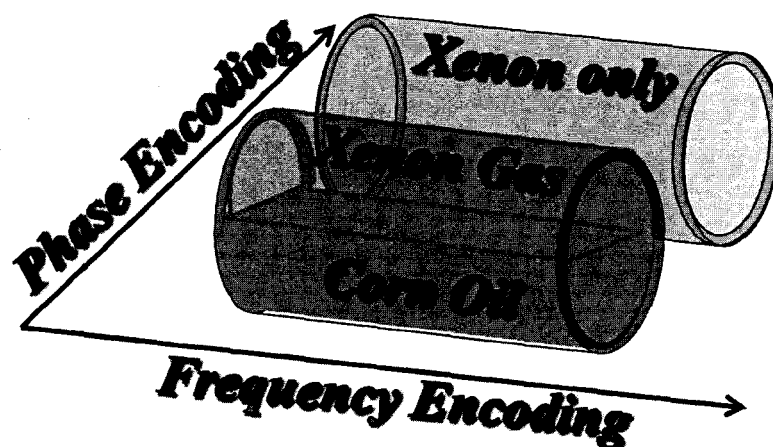
180

Figure 7.3: The experimental setup for corn oil - xenon experiments. 2 cylindrical glass cells were used, one half filled with corn oil. After evacuating the cells to reduce the amount of oxygen, both cells were filled with hyperpolarized xenon to 1 atmosphere.

RV, breathe the gas mixture from the bag, hold the breath. The whole sequence takes just about 6 seconds to run, thus breath-holds for these experiments were well under 10 seconds.

7.7.1 Calibration Results

The chemical shift frequency $\Delta\nu$ was measured to be 472 Hz for the corn oil. T_1 was determined to be 83 s and 8.7 s for the gas and dissolved states, respectively. 1D projections were collected, and integration of the signal from the gaseous and corn oil peaks shows the ratio of the signal in the two states is 0.36, which is a measure of the partition coefficient for corn oil. Figure (7.4) shows the signal from 1D projections after the signal separation.

We have collected images of the cells as well, and separated the gas and the dissolved state signals. The results are presented in Figure (7.5). From these images it can be seen that the separation of the signals is quite good, as well as that there is no position shift in

181
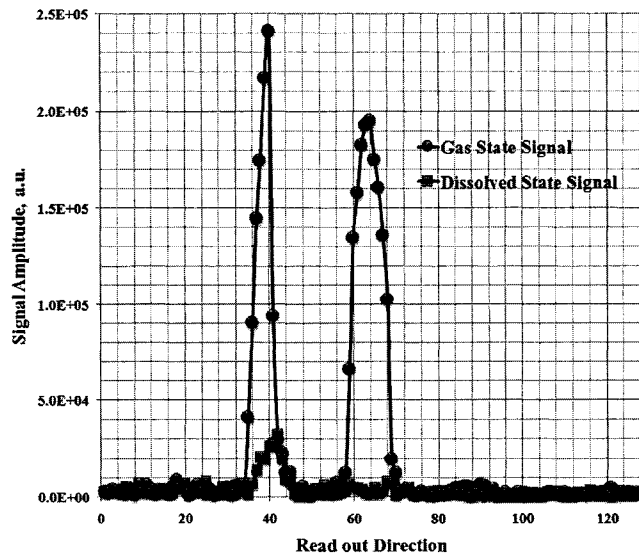
Figure 7.4: 1D Dixon technique with two cells. One of the cells cointains gas only, the other - oil and gas. The gas and dissolved signals are successfully separated.

the oil signal due to the chemical shift.

The last test of the technique was done on a number of either glass or plastic phantoms, where there should be no dissolved state measured. Figure (7.6) presents results of such a run.At this point we were convinced that the sequence measures what it should, and we could trust the results, and consequently carry out experiments involving human subjects.

7.8 Human studies

We have performed experiments on normal healthy subjects at two different lung volumes - near FRC and closer to TLC. In Figure (7.7) we present sample sets of experimental results from 2 different lung volumes. The top 3 images are gas signal only, dissolved signal only and a calculated measure of the gas exchange in the lungs, respectively. The scale for Fractional Gas Transport maps was kept constant in the figure to facilitate visual compar-

182

| Gas Phase Image | Dissolved Phase Image | Phase Map |
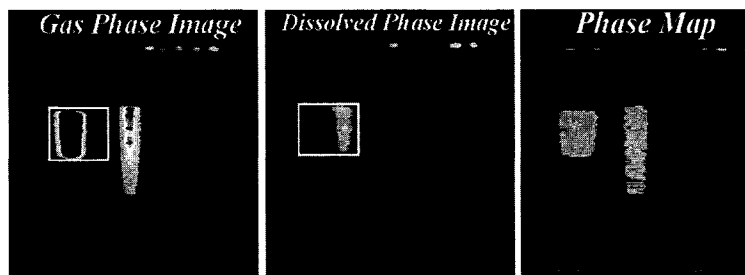
Figure 7.5: 2D projection images of two cells, one with gaseous xenon only, and the other one - with xenon gas and xenon dissolved into the corn oil.
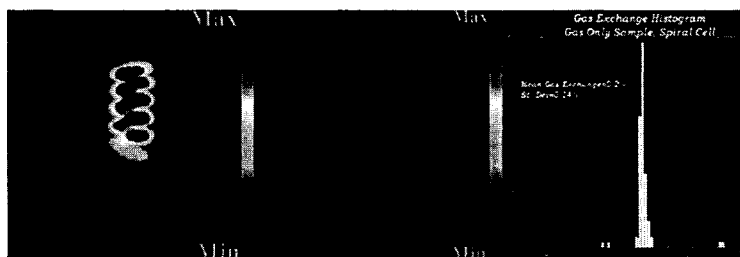
Figure 7.6: The calibration of the Dixon technique performed on a glass cell filled with xenon. Using our reconstruction we were very successful in separating the gas signal from the dissolved (non-existent in this case) state signal.

183
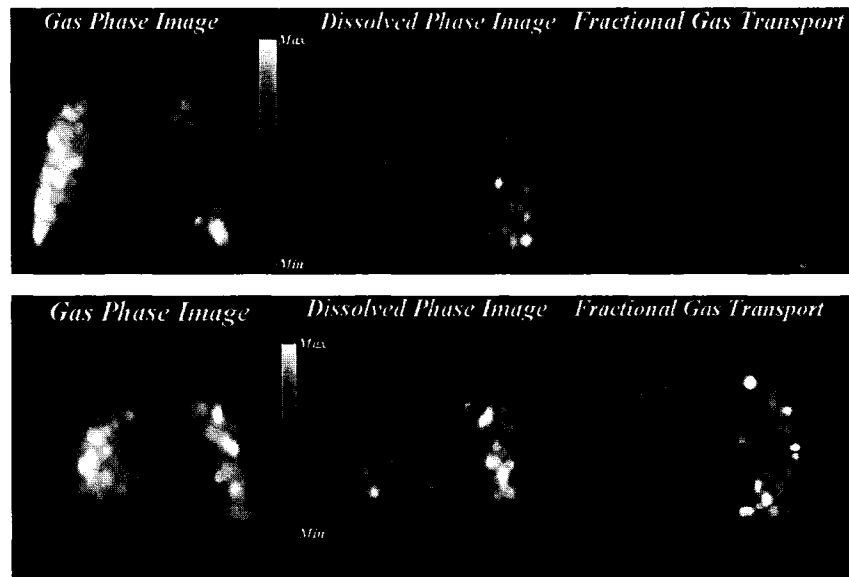
Figure 7.7: Sample data from a subject at two different lung volumes. The top row shows the data at higher lung volume ($\sim$ 70% TLC), while the bottom one is at FRC. As expected, and has been seen in XTC experiments as well, the higher lung volume shows more homogeneous distribution of the gas exchange. Also, the exchange values at highel lung volumes are smaller that those at lower lung volumes. This also agrees with previously recorded results [49], as well as our measurements with the XTC technique.

184
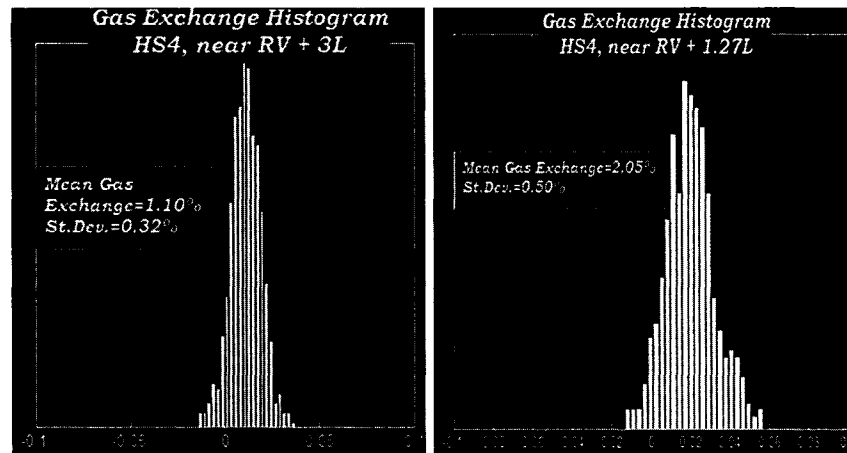
Figure 7.8: Histograms of the collected maps of the fractional gas transport at two lung volumes. These histograms correspond to the data shown in the fig. (7.7).

ison. As evident from the maps, the exchange is elevated at low lung volumes compared to higher lung volumes. Figure (7.8) shows the histograms of the distribution of $F(62.5\ ms)$.

7.9 Discussion of the Results

The 3-point Dixon technique was used to map the fractional gas diffusion directly. A diffusion time of 62.5ms was used, for which according to $CSSR$ and XTC spirometry measurements $F\left(t_{exchange}\right) \propto S_A/V_{Gas}$ (see $CSSR$ experiments). The technique underwent a series of tests and calibrations, carried out on several phantoms. These experiments demonstrated not only a clear separation of the signals, but successful implementation of the chemical shift correction as well. Also, they provided numbers consistent with no exchange in gas only phantoms.

A total of 6 experiments were performed on 2 normal healthy subjects at 2 different lung volumes - one, close to FRC and the other - near TLC. The obtained mean fractional gas

185

diffusibility $F(62.5\ ms)$ values were $1.69 \pm 0.58\%$ and $2.05 \pm 0.5\%$ for lower lung volumes and $1.10 \pm 0.32\%$ and $1.15 \pm 0.38\%$ for higher lung volumes for one subject (HS6) and $1.45 \pm 0.31\%$ and $0.95 \pm 0.23\%$ for the other one (HS4). The $F(62.5ms)$ value increases, as expected, with the decrease of lung volume. However, it shows stronger dependence than predicted by studies done on fixed animal lungs and measured with microscopy [39].

Both subjects showed more homogeneous fractional gas transport maps at higher lung volume, which is in accord with XTC data as well. This feature is evident from Figure (7.7). We also looked at the apex to base distribution of the fractional gas transport. Despite the fact that the data were collected in supine subjects, their exchange maps showed a dependence on the apex-base position. This also agrees with the behavior seen in XTC experiments with a much larger pool of subjects.

The 3-point Dixon technique, unlike to the previously described XTC method, where the dissolved state is probed indirectly through modulation on the gas state signal, is a direct measure of both dissolved and gas state signals, and is complementary to the approach of XTC. Since the dissolved state signal constitutes only about 2% of the total signal, the data collected with the Dixon method suffers from low SNR, making its application less practical. Nevertheless, the technique shows great promise for applications at slightly higher fields, where it is easier for the RF coils to reach their optimal loading.

CHAPTER 8

SUMMARY

The World Health Organization [87] reports that 80 *million* people suffer from moderate to severe $COPD$ worldwide and in 2005 3 *million* died of $COPD$, which corresponds to 5% of all deaths globally. They predict that the number of deaths from $COPD$ will increase by more than 30% in the next 10 years, and it is projected that by 2030 the mortality will increase to 9.3 *million* per year. The currently available tests do not possess the sensitivity needed to diagnose the disease in its early stages. Although the symptoms of $COPD$ may develop early, typically people who are diagnosed are over 45 years old, have at least 20 pack years of smoking history, and are suffering from advanced stages of the disease. In this light it becomes imperative to establish a suite of tests capable of diagnosing $COPD$ early, thereby increasing the chances of a successful treatment that leads to the patients' recovery.

Computed tomography tests are equipped to handle some of these challenges, but are also accompanied by harmful radiation. This is a major disadvantage, absent in hyperpolarized gas MRI, where images are acquired based on the phenomenon of Nuclear Magnetic Resonance. Xenon MRI, in particular, offers not only a way to image the gaseous compartments in the lungs but also to infer information about the pulmonary septum. The latter is accomplished by exploiting xenon's sensitivity to its immediate environment, and its diffusibility into the tissue. The description of this methodology and its implementation to human subjects constituted the main scope of this dissertation. In it I presented several

187

techniques designed to probe the lung as a whole as well as to obtain local information. For the firs time, these methods were applied to human studies.

The $CSSR$ technique was implemented to investigate *in vivo* the diffusion dynamics driving the gas exchange. We modeled the process of gas exchange for a case of a one-dimensional diffusion into a tissue slab. The data acquired with $CSSR$ technique (fractional gas transport measurements at variable exchange times) was closely described by this model. This method allows the estimation of the septal thickness along with the total surface area available for the gas exchange.

Using $CSSR$ we studied 3 normal healthy subjects and 2 subjects with mild to moderate Interstitial Lung Disease. For ILD patients, alveolar wall inflammation results in thicker gas-blood barrier. Echoing this behavior, fit of the data to the diffusion into a slab model provided higher values for the tissue thickness in ILD patients relative to the normals. The values of the total surface area, obtained in these experiments, were below the predicted numbers. One of the possible reasons for this effect may be the choice of the first exchange time used in the measurements: $t_{exchange} = 17\,ms$. A xenon molecule can travel $\sim 2.5-3\,\mu m$ into the tissue during this exchange time, and if the septal surface is not flat (but rather has "thin" ($< 2.5\,\mu m$ for our purposes) and "thick" ($> 2.5\,\mu m$) regions), then the "thin" portions will be saturated by the time we collect the data corresponding to the first exchange time. Another possibility is that these predictions are based on histological studies of the "alveolar only" regions of the lungs, whereas our measurements provide an average fractional gas transport from all regions where the gas exchange takes place. In such a case, since more surface is available for the exchange in the alveolar spaces, the fractional gas transport measured with our method is expected to be below that measured in histological

188

studies, e.g. for a normal healthy subject we calculated a total alveolar surface area of $S_A^{CSSR,HS6} = 55 \ m^2$ while the predicted value is $S_A^{predicted, \ HS6} = 82.8 \ m^2$.

The $CSSR$ technique was also utilized to measure the dependence of the parenchymal surface area on the lung volume *in vivo* for the first time in three normal healthy humans. This was achieved by using the MRI compatible spirometer (Mirtech, Inc.). The data were fit to a power function: $S(V) = aV^\beta$ and the parameters extracted from the fit were $a = 0.0032 \pm 0.0008$, $\beta = -0.6621 \pm 0.1863$. This behavior does not agree with previously recorded functional form: $S(V) = kV^{0.33}$ and $S(V) = k'V^{0.58}$ for air and saline filled fixed lungs. This discrepancy between our observation of the alveolar surface area dependence on lung volume and earlier reported studies could also be explained by the "thin" and "thick" partition model. The technique's insensitivity to "thin" tissue regions obscures the stretching effects due to increased lung volume. Then as we go to higher lung volumes some parts stretch and become "thin" and undetectable.

Another possible explanation for the discrepancy is that it could arise from the difference in the techniques used for the measurements. All previous studies were performed on fixed lungs ([85], [39]), while our measurements are done *in vivo*.

We successfully employed the Dixon technique for direct measurements of the xenon dissolved phase. We thoroughly tested and calibrated the technique: a proper separation of the images of the dissolved and gaseous phases from data acquired on glass cells was achieved. Moreover, in a cell filled only with gaseous xenon, the mean fractional exchange time calculated from a region of interest of the dissolved and gaseous phase images, was non-significant.

The technique was then used to measure the fractional gas transport *in vivo* in two

189

normal healthy humans for the first time. We separated the signals from the gas and dissolved states, collected simultaneously, and deduced the fractional gas transport. For both subjects, the distribution of the fractional gas transport showed the expected behavior: it was more homogeneous at higher lung volumes. Despite the fact that the dissolved state comprises only 2 % of the available xenon and the signal to noise ratio in the dissolved state images is quite low, the technique showed enough sensitivity to depict the differences in the fractional gas transport in the apical and basal regions of the lungs.

The problem with the low signal-to-noise ratio in the dissolved phase images is overcome in the XTC technique, since only ventilation images are involved in this method. Some modifications were introduced to the original technique [49]. Subsequently, the modified version went through several calibration tests and was implemented with human subjects: five healthy non-smokers and 7 asymptomatic smokers participated in the studies. The results revealed that the fractional gas transport shows dependence on the lung inflation level: at higher lung volumes mean $F(t)$ is lower, which is in agreement with earlier studies on animals [49]. Also, $F(t)$ and thus the alveolar size, proved to be more evenly distributed at higher lung volumes. Although the data were collected in the supine position, a difference in $F(t)$ in the apical and basal regions was observed. We attributed this difference to a "memory" in the lungs of the gravitationally induced alterations in the level of expansion of different parts (in upright position the lung stretch like a slinky hang from the top - more on the top and very little on the bottom).

When comparing smokers and non-smokers results, the former group showed higher values of the fractional gas transport together with wider distribution. We studied the sensitivity of the XTC technique to early changes in the lungs by comparing its correlation

190

to smoking history with that of DL_{CO} and FEV_1. Both, the mean fractional gas transport and the physiological heterogeneity displayed changes with smoking history. $\sigma_{F, \ Physiol}$ increased with the smoking history but a large scatter in the $\sigma_{F, \ Physiol}$ versus smoking history plot was observed. Hence more statistics are required to draw conclusion of the correlation of $\sigma_{F, \ Physiol}$ ($r_{low \ lung \ vol.} = 0.26$ and $r_{high \ lung \ vol.} = 0.21$) with early changes in the lungs. $\overline{F(t)}$ on the other hand showed a strong correlation ($r_{low \ lung \ vol.} = 0.97$ and $r_{high \ lung \ vol.} = 0.87$) with the smoking history at both lung volumes studied. However it showed very peculiar behavior: it first increased reaching a maximum at ~ 12 pack years, and then decreased. DL_{CO} and FEV_1 showed no significant correlation ($r_{DL_{CO}} = 0.12$ and $r_{FEV_1} = 0.14$) with the smoking history. The preliminary results reveal that XTC shows greater correlation with the smoking history of the subjects compared to such gold standards as DL_{CO} and FEV_1.

Despite the low SNR in Dixon images, the values we obtained for the gas exchange are in agreement with the ones from XTC. Two of the subjects underwent experiments involving both techniques at about the same lung volume - near FRC. For one of them (HS4) the mean alveolar surface area calculated based on Dixon method is $S_A^{Dixon, \ HS4} = 95.2 \pm 20.3 \ m^2$ and based on XTC it is $S_A^{XTC, \ HS4} = 99.9 \pm 9.3 \ m^2$, while for the other subject ($HS6$) the numbers are $S_A^{Dixon, \ HS6} = 103.7 \pm 21.2 \ m^2$ and $S_A^{XTC, \ HS6} = 91.1 \pm 5.6 \ m^2$, respectively. The predicted value for the alveolar surface area for a human of their height ($HS4$ and $HS6$ happen to have the same height: 177.8 cm) is $S_A^{predicted, \ 177.8cm} = 82.8 \ m^2$.

The methods described in this work show great promise as techniques capable of revealing early changes in the lungs. The development of these methods is still in its early stages. A number of improvements will propel these approaches into becoming robust and

191

indispensable tools used routinely in diagnostic medicine.

192

BIBLIOGRAPHY

[1] Kumar A, Welti D, and Ernst RR. Nmr fourier zeugmatography. *J Magn Res*, 18:69–83, 1975.

[2] Cormick AM. Representation of a function by its line integrals, with some radiological applications. *J Appl Phys*, 34:2722–2727, September 1963.

[3] Cormick AM. Representation of a function by its line integrals, with some radiological applications. ii. *J Appl. Phys.*, 35(10):2908–1913, October 1964.

[4] Driehuys B, Cates GD, Miron E, Sauer K, Walter DK, and Happer W. High volume production of laser-polarized 129xe. *Appl Phys Lett*, 69:1668–1670, 1996.

[5] Coombs BD, Szumowski J, and Coshow W. Two-point dixon technique for water-fat signal decomposition with b0 inhomogeneity correction. *MRM*, 38:884–889, 1997.

[6] Goodson BM. Nuclear magnetic resonance of laser-polarized noble gases in molecules, materials, and organisms. *J.Magn.Rson.*, 155:391–392, 2002.

[7] Bohr C. Ueber die spezifische tätigkeit der lungen bei der respiratorischen gasaufnahme. *Scand. Arch. Physiol.*, 22:221–280, 1909.

[8] Bratton CB, Hopkins AL, and Weinberg JW. Nuclear magnetic resonance studies of living muscle. *Science*, 147:738, 1965.

[9] Slichter CP. *Principles of Magnetic Resonance*. Solid State Science 1. Springer-Verlag, 1990.

[10] Canet D. *Nuclear Magnetic Resonance: Concepts and Methods*. John Wiley and Sons, New York, 1996.

[11] Brenner DJ, Elliston CD, Hall EJ, and Berdon WE. Estimated risks of radiation-induced fatal cancer from pediatric ct. *American Journal of Roentgenology*, 176:289–296, 2001.

[12] Hinshaw DS, Bottomley PA, and Holland GN. Radiographic thin-section image of the human wrist by nuclear magnetic resonance. *Nature*, 270:722–723, 1977.

[13] Odeblad E, Bhar BN, and Lindström G. Proton magnetic resonance of human red blood cells in heavy water exchange experiments. *Arch Biochem Biophys*, 63:221–225, 1956.

[14] Zavoisky EK. *J Phys USSR*, 9:211–245, 1945.

[15] Hahn EL. Spin echoes. *Phys Rev*, 80:580–594, 1950.

[16] Haake EM, Patrick JL, Lenz GW, and Parrish T. The separation of water and lipid components in the presence of field inhomogeneities. *MRM*, 1:123–154, 1986.

[17] Purcell EM, Torrey HC, and Pound RV. Resonance absorption by nuclear magnetic moments in a solid. *Phys Rev*, 69:37–38, 1946.

[18] Hunt ER and Carr HY. Nuclear magnetic resonance of 129xe in natural xenon. *Phys. Rev.*, 130:2302–2305, 1963.

[19] Weibel ER. *Morphometry of the human lung*. Academic Press, 1963.

[20] Weibel ER. Stereological principles for morphometry in electron microscopic cytology. *Int. Rev. Cytol.*, 26:235–302, 1969.

[21] Weibel ER. Morphometric estimation of pulmonary diffusion capacity. *Resp. Physiol.*, 11:54–75, 1970/71.

[22] Weibel ER and Knight BW. A morphometric study on the thickness of the pulmonary air-blood barrier. *J. Cell Biol.*, 21:367–384, 1964.

[23] Weibel ER, Kistler GS, and Scherle WF. Practical stereological methods for morphometric cytology. *J. Cell Biol.*, 30:23–38, 1966.

[24] Weibel ER and Vidone RA. Fixation of the lung by formalin steam in a controlled state of air inflation. *Am. Rev. Resp. Dis.*, 84:856–861, 1961.

[25] Bloch F. Nuclear induction. *Phys. Rev.*, 70:460–474, 1046.

[26] Block F, Hanson WW, and Packard M. Nuclear induction. *Phys Rev*, 69:127, 1946.

[27] Eropean Lung Foundation.

[28] Glover GH. Multipoint dixon technique for water and fat proton and susceptibility imaging. *JMRI*, 1:521–530, 1991.

[29] Hakon Gudbjartsson and Sam Patz. The rician distribution of noisy mri data. *Magnetic Resonance in Medicine*, 34:910–914, 1995.

[30] Hatabu H, Gaa J, Kim D, Li W, Prasad PV, and Edelman RR. Pulmonary perfusion: Qualitative assessment with dynamic contrast-enhanced mri using ultra-short te and inversion recovery turbo flash. *MRM*, 36:503–508, 1996.

[31] R.M. Henkelman. Measurement of signal intensities in the presence of noise in mr images. *Medical Physics*, 12(2):232–233, 1985.

[32] Clever HL. *Krypton, Xenon and Radon - Gas Solubilities*, volume 2. Oxford: Pergamon, 1979.

[33] Carr HY and Purcell EM. Effects of diffusion on free precession in nuclear magnetic resonance experiments. *Phys Rev*, 94:630–638, 1954.

[34] Ruset I, Ketel S, and Hersman FW. *Phys. Rev. Lett.*, 96:053002, 2006.

[35] Ruset IC. *Hyperpolarized xenon production and applications.* PhD thesis, University of New Hampshire, Durham, NH, May 2005.

[36] Rabi II, Zacharias JR, Millman S, and Kusch P. A new method of measuring nuclear magnetic moment. *Phys Rev*, 53:318, 1938.

[37] Mugler JP III, Driehuys B, Brookeman JR, Cates GD, Berr SS, Bryant RG, Daniel TM, deLange EE, Downs JH III, Erickson CJ, Happer W, Hinton DP, Kassel NF, Maier T, Phillips CD, Saam BT, Sauer KL, and Wagshul ME. Mr imaging and spectroscopy using hyperpolarized 129xe gas: preliminary human results. *MRM*, 37:809–815, 1997.

[38] Gil J and Weibel ER. Improvements in demonstration of lining layer of lung alveoli by electron microscopy. *Resp. Physiol.*, 8:13–36, 1969.

[39] Gil J, Bachofen H, Gehr P, and Weibel WR. Alveolar volume-surface area relation in air- and saline-filled lungs fixed by vascular perfusion. *J Appl Physiol: Respirat Environ Exercise Physiol*, 47(5):990–1001, 1979.

[40] West J, editor. *Bioengeneering aspects of the lung*, volume 3 of *Lung biology in health and disease.* Marcel Dekker, Inc., 1077.

[41] Borrello JA, Chenevert TL, Meyer CR, Aisen AM, and Glaser GM. Chemical shift based true water and fat images: regional phase correction of modified spin-echo mr imaging. *Radiology*, 164:531–537, 1987.

[42] Jackson JA and Langham WH. Whole-body nmr spectrometer. *Rev Sci Instrum*, 39:510–513, 1968.

[43] Lawrence JH, Loomis WF, Tobias CA, and Turpin FH. Preliminary observations on the narcotic effect of xenon with a review of values for solubilities of gases in water and oils. *J. Physiol.*, 105:197–204, 1946.

[44] Szumowski JH, Coshow WR, Li F, and Quinn SF. Phase unwrappin in the three-point dixon method for fat suppression mr images. *Radiology*, 192:555–561, 1994.

[45] Butler JP, Mair RW, Hoffmann D, Hrovat MI, Rogers RA, Topulos GP, Walsworth RL, and Patz S. Measuring surface-area-to-volume ratios in soft porous materials using laser-polarized xenon interphase exchange nmr. *J. Phys.: Condens. Matter*, 14:L297–L304, 2002.

[46] Hansen JR. Pulsed nmr study of water in muscle and brain tissue. *Biochim Biophys Acta*, 230:482–486, 1971.

[47] Hajnal JV, Hill D, and Hawkes DJ. *TEX: Medical Image Registration.* Biomedical Engineering. CRC Press, 2001.

[48] Kaneko K, Milic-Emili J, Dolovich MB, Dawson A, and Bates DV. Regional distribution of ventilation and perfusion as a function of body position. *J Appl. Physiol.*, 21(3):767–777, 1966.

[49] Ruppert K, Mata JF, Brookeman JR, Hagspiel KD, and Mugler III JP. Exploring lung function with hyperpolarized 129xe nuclear magnetic resonance. *Magn. Reson. Med*, 51:676–687, 2004.

[50] Ruppert K, Brookeman JR, Hagspiel KD, and Mugler III JP. Probing lung physiology with xenon polarization transfer contrast (xtc). *MRM*, 44:349–357, 2000.

[51] Karin Kneöaurek, Marija Ivanovic, Josef Machac, and David A. Weber. Medical image registration. *Europhysics News*, 31(4), 2000.

[52] Peter J. Kostelec and Senthil Periaswamy. Image registration for mri. *Modern Signal Processing*, 46:161–184, 2003.

[53] Anderson LW, Pipkin FM, and Baird JC. *Phys Rev Lett*, 120:1279, 1960.

[54] Springuel-Huet MA, Bonardet JL, Gedeon A, and Fraissard J. Xe-129 nmr: overview of xenon physisorbed in porous solids. *Magn. Reson. Chem.*, 37:1–13, 1999.

[55] Albert Makovski. Noise in mri. *Magnetic Resonance in Medicine*, 36(3):494–497, 1996.

[56] Spence MM, Rubin SM, Dimitrov IE, Ruiz EJ, Wemmer DE, Pines A, Yao SQ, Tian F, and Schultz PG. Functionalized xenon as a biosensor. *Proc. Natl. Acad. Sci. USA*, 98:10654–10657, 2001.

[57] Bouchiat MR, Carver TR, and Varnum CM. Nuclear polarization in he3 gas induced by optical pumping in dipolar exchange. *Phys. Rev. Lett*, 5(8):373–375, 1960.

[58] Albert MS, Cates GD, Driehuys B, Happer W, Saam B, Springer Jr. CS, and Wishnia. A biological magnetic resonance imaging using laser-polarized 129xe. *Nature*, 370:199–201, 1994.

[59] Robert D. Novak. Wavelet-based rician removal for magnetic resonance imaging. *IEEE Transactions on Image Processing*, 8(10):1408–1419, 1999.

[60] Hall P, Adami H-O, Trichopoulos D, Pedersen NL, Lagiou P, Ekbom A, Ingvar M, Lundell M, and Granath F. Effect of low doses of ionising radiation in infancy on cognitive function in adulthood: Swedish population based cohort study. *BMJ*, 328:19, 2004.

[61] Lauterbur PC. Image formation by induced local interactions: examples of employing nuclear magnetic resonance. *Nature*, 242:190–191, 1973.

[62] Lauterbur PC. Magnetic resonance zeugmatography. *Pure and Applied Chemistry*, 40:149–157, 1974.

[63] Damadian R, Goldsmith M, and Minkoff L. Nmr in cancer: Xvi. fonar image of the live human body. *Physiol Chem Phys*, 9:97–100, 1977.

[64] Gabillard R. Résonance nucléaire mesuré du temps de relaxation t2 en présence d'une inhomogenéité de champ magnétique supérieur à la largeur de raie. *C R Acad Sci Paris*, 232:1551–1553, 1951.

[65] Seydoux R, Diehl P, Mazitov RK, and Jokisaari J. Chemical shifts in magnetic resonance of the 129xe nucleus in liquid solvents and comparison with other noble gases. *Journal of Magnetic Resonance A*, 101:78–83, 1993.

[66] Forster RE. *Diffusion of Gases*, volume 1, chapter Handbook of Physiology 3. Respiration, pages 839–872. American Physiological Society, 1964.

[67] Streever RL and Carr HY. Nuclear magnetic resonance of xe-129 in narural xenon. *Phys. Rev.*, 121:20–25, 1961.

[68] Edelman RR, Harabu H, Tadamura E, Li W, and Prasad PV. Noninvasive assessment of the regional ventilation in the human lung using oxygen-enhanced magnetic resonance imaging. *Nature Medicine*, 2:1236–1239, 1996.

[69] Damadian RV. Tumor detection by nuclear magnetic resonance. *Science*, 171:1151–1153, 1971.

[70] Mair RW, Wong GP, Hoffmann D, Hurlimann MD, Patz S, Schwartz LM, and Walsworth RL. Probing porous media with gas diffusion nmr. *Phys. Rev. Lett.*, 83:3324–3327, 1999.

[71] Mair RW and Walsworth RL. Novel mri applications of laser-polarized noble gases. *Appl. Magn. Reson.*, 22:159–173, 2002.

[72] Gardner S, Green J, and Bednarczyl E et al. Principles and clinical applications of positron emission tomography. *Am J Health Syst Pharm.*, 49:1499–1506, 1992.

[73] Mansson S, Wolber J, Driehuys B, Wollmer P, and Golman K. Characterization of diffusing capacity and perfusion of the rat lung in a lipopolysaccaride disease model using hyperpolarized 129xe. *MRM*, 50:1170–1179, 2003.

[74] Moon-Ho S, Napel S, Pelc NJ, and Glover GH. Phase unwrapping of mr phase images using poisson equation. *IEEE Trans. Image Proc.*, 4:667–676, 1995.

[75] Peled S, Jolesz FA, Tseng CH, Nascimben L, Albert MS, and Walsworth RL. Determinants of tissue delivery for 129xe magnetic resonance in humans. *MRM*, 36:340–344, 1996.

[76] Cullen SC, Eger EI, Cullen BF, and Gregory P. Observations on the anesthetic effect of the combination of xenon and halothane. *Anesthesiology*, 31:305–309, 1969.

[77] Ito T and Fraissard J. In LVC Rees, editor, *5th Int. Conf. on Zeolites*, page 510, Heyden, Naples, 1980.

197

[78] Marx T. Xenon anesthesia. *J.R.Soc.Med*, 93:513, 2000.

[79] Skinner TE and Glover GH. An extended teo-point dixon algorithm for calculating separate water, fat and bo images. *MRM*, 37:628–630, 1997.

[80] Ligon TR. Master's thesis, 1967.

[81] Whittington Hospital NHS Trust. The beatles greatest gift... is to science, May 2007.

[82] Kilian W, Seifert F, and Rinneberg H. Dynamic nmr spectroscopy of hyperpolarized 129xe in human brain analyzed by an uptake model. *MRM*, 51:843–847, 2004.

[83] Kilian W, Seifert F, and Rinneberg H. Time- and spatially-resolved in vivo human brain mr-spectroscopy using hyperpolarized 129xe. *Proc. ISMRM, 11th meeting*, page 767, 2004.

[84] Schull WJ. *Effects of Atomic Radiation: A Half-Century of Studies from Hiroshima and Nagasaki*. Wiley-Liss, 1995.

[85] Thurlbeck WM. The internal surface area of non-emphysematous lungs. *Am. Rev. Respir. Dis.*, 95:765–773, 1967.

[86] www.emrf.org. European magnetic resonance forum.

[87] WHO (www.who.int/mediacentre/factsheets/fs315/en). Chronic obstructive pulmonary disease (copd), 2005.

[88] Zeng X, Wu Z, Call T, Miron E, Schreiber D, and Happer W. Experimental determination of the rate constants for spin exchange between optically pumped k, rb and cs atoms and 129xe nuclei in alkili-metal noble-gas van der waals molecules. *Phys. Rev. A*, 31(1):260–278, 1985.

[89] Brethezene Y, Vexler V, Clement O, Muhler A, Moseley ME, and Brasch RC. Contrast-enhanced mri imaging of the lung: Assessments of ventilation and perfusion. *Radiology*, 183:667–672, 1992.

APPENDICES

A. FDA IND Human Protocol Approval

FDA IND approval is required to perform studies using hyperpolarized xenon involving human subjects. The experiments described in this dissertation were performed with human subjects using hyperpolarized ^{129}Xe. Attached is the FDA Investigational New Drug approval for the mentioned studies.

200

Public Health Service

Food and Drug Administration
Rockville, MD 20857

IND 68,949

F. William Hersman, Ph.D.
Physics Dept – University of New Hampshire
9 Library Way
Durham, NH 03824

Dear Dr. Hersman:

Please refer to your Investigational New Drug Application (IND) submitted under section 505(i) of the Federal Food, Drug, and Cosmetic Act for Xe-129.

We also refer to your clinical response of February 1; chemistry response of February 4; clinical pharmacology response of February 10; and our clinical pharmacology comments of February 17, 2004.

We have completed our 30-day safety review of your application and have concluded that it is reasonably safe to proceed with your proposed clinical investigation once you have incorporated the clinical comments into an amended protocol as discussed at the teleconference on February 19, 2004.

Also, we remind you of your Letter-of-Commitment of February 19, 2004, in which you have agreed to submit an amended protocol to reflect the Division's clinical comments (facsimile, 02\19\04) as well as addressing the two outstanding chemistry comments (your facsimile, 02\04\04) and the clinical pharmacology comments (your facsimile, 02\10\04).

If we have any additional comments to relay to you, we will send them to you in a separate letter.

As Sponsor of this IND, you are responsible for compliance with the Federal Food, Drug, and Cosmetic Act and the implementing regulations (Title 21 of the Code of Federal Regulations). Those responsibilities include (1) reporting any unexpected fatal or life-threatening adverse experience associated with use of the drug by telephone or fax no later than 7 calendar days after initial receipt of the information [21 CFR 312.32(c)(2)]; (2) reporting any adverse experience associated with use of the drug that is both serious and unexpected in writing no later than 15 calendar days after initial receipt of the information [21 CFR 312.32(c)(1)]; and (3) submitting annual progress reports (21 CFR 312.33).

201

IND 68,949: Xe-129
Page 2

Please forward all future communications concerning this IND in ***triplicate*** along with Form
FDA 1571, identified by the above IND number, to the following address:

<div style="margin-left: 2em;">

<u>U.S. Postal Service/Courier/Overnight Mail:</u>
Food and Drug Administration
Center for Drug Evaluation and Research
Division of Medical Imaging and Radiopharmaceutical Drug Products
Attention: FDA Document Room #8B-45
5600 Fishers Lane, HFD-160
Rockville, Maryland 20857

</div>

If you have any questions, call Thuy M. Nguyen, M.P.H., Regulatory Health Project Manager,
at (301) 827-7510.

<div style="margin-left: 4em;">

Sincerely,

{See appended electronic signature page}

Patricia Stewart
Acting Chief, Project Management Staff
Division of Medical Imaging and
 Radiopharmaceutical Drug Products, HFD-160
Office of Drug Evaluation III
Center for Drug Evaluation and Research

</div>

202

B. IRB Human Protocol Approval

IRB approval is required for Ph.D. Theses involving human subject experiments. The experiments described here were performed with human subjects at Brigham and Women's Hospital in Boston, Massachusetts. Attached is the latest human protocol BWH IRB approval for the magnetic resonance imaging experiments using hyperpolarized ^{129}Xe.

Continuing Review: Notification of IRB Approval/Activation

Protocol #: 2005-P-000302/24; BWH

Date: 03/08/2007

To: Samuel Patz, Ph.D
          Radiology
          LMRC-GR 221 Longwood

From: Anne DiSorbo
          PHS Research Management
          116 Huntington Ave 10

Title of Protocol: Infrastructure and Application of Hyperpolarized 129Xenon MRI
Version/Number: 5R01 HL07363-02
Version Date: 01/19/2007
Sponsor: NIH-NHLBI National Heart, Lung, and Blood Institute
IRB Continuing Review #:   2
IRB Review Type: Full
IRB Approval Date: 02/14/2007
Approval Effective Date: 03/08/2007
IRB Expiration Date: 02/14/2008

This Project has been reviewed and approved by the BWH IRB, Assurance # FWA00000484. During the review of this Project, the IRB specifically considered (i) the risks and anticipated benefits, if any, to subjects; (ii) the selection of subjects; (iii) the procedures for securing and documenting informed consent; (iv) the safety of subjects; and (v) the privacy of subjects and confidentiality of the data.

Please note that if an IRB member had a conflict of interest with regard to the review of this project, that member left the room during the discussion and the vote on this project.

NOTES: The following documents were reviewed and approved by the IRB: Protocol Summary (dated 1/19/2007), Detailed Protocol (dated 1/19/2007), Consent Form (1), Advertisement (1), and Questionnaires (3).

As Principal Investigator you are responsible for the following:

1. Submission in writing of any and all changes to this project (e.g., protocol, recruitment materials, consent form, study completion, etc.) to the IRB for review and approval prior to initiation of the change(s), except where necessary to eliminate apparent immediate hazards to the subject(s). Changes made to eliminate apparent immediate hazards to subjects must be reported to the IRB within 24 hours.
2. Submission in writing of any and all adverse event(s) that occur during the course of this project in accordance with the IRB's policy on adverse event reporting.
3. Submission in writing of any and all unanticipated problems involving risks to subjects or others.
4. Use of only IRB approved copies of the consent form(s), questionnaire(s), letter(s), advertisement(s), etc. in your research. Do not use expired consent forms.

205

The IRB can and will terminate projects that are not in compliance with these requirements. Direct questions, correspondence and forms (e.g., continuing reviews, amendments, adverse events, safety reports) to Anne DiSorbo, (617) 424-4118.

cc:
Christina Johnson, Radiology